IMPEDANCE MODELLING AND STABILITY ANALYSIS OF POWER GRID-CONNECTED INVERTER-BASED RESOURCES

by

SHUAILONG DAI

A thesis submitted to the University of Birmingham for the degree of

DOCTOR OF PHILOSOPHY

Department of Electronic, Electrical and Systems Engineering
School of Engineering
University of Birmingham
April 2024

Abstract

Modern power systems are transitioning from synchronous generators dominated power systems to inverter-based resources (IBRs) dominated power systems. This change leads to low inertia and low fault current power systems, which tends to cause power system oscillations. Traditional modelling methods have the difficulty to capture the dynamic response of complex control systems. In addition, detailed white box models of inverters are generally unavailable due to commercial intellectual property and other commercial reasons. Therefore, impedance-based stability analysis has various applications for such black-box models.

This thesis aims at the development of methods and tools for the enhancement of the stability of power systems with a high proportion of renewable energy. This is to be achieved by development of a number of methods and tools, which include impedance modelling methods using measurements, impedance-based stability analysis method and tool with fast preliminary screening and detailed impedance-based stability theory, novel auxiliary phase-locked loop (PLL) control method to enhance to enlarge the stable boundary, stability enhancement by impedance tuning method using perturbation and observation, a data-driven automation method for clustering and aggregation of multiple operating point impedance models, and a data-driven automation method using a Bayesian optimisation method to determine stability boundary.

The two impedance-based modelling methods are implemented to demonstrate the characteristics of the interconnected power system. The impedance modelling method derived from state space equations is presented and the impedance modelling method based on measurements is also presented. Then they are compared, which indicates that the impedance model based on measurements can match the impedance model derived from state-space equations very well. Furthermore, several important concerns for practical applications are addressed and appropriate guidance is provided to obtain a highly accurate model via case study.

Based on the impedance model of the interconnected system, the impedance-based stability analysis is widely adopted to understand the system oscillation phenomenon normally caused by control interaction. A two-step screening method including multi-infeed impact factor (MIIF) and short circuit ratio (SCR) index are proposed in this thesis to identify the potential threats. If a risk is identified, then secondly a full-scale analysis is automated using an automation tool as a scripting tool. Hence, the systematic method, including preliminary screening and impedance-based stability theory, is proposed to trade off effort and accuracy.

Since the stability analysis is presented, the further actions on stability enhancement could be implemented. The information obtained from the state-space model is validated with simulations, revealing how the control parameters affect the impedance transfer function and eigenvalues. A novel auxiliary phase-locked loop (PLL) control method is proposed to enlarge the stable boundary of the operating points by impedance reshaping methods.

For the black box model, it would be a bit challenge to enhance the stability for inverter cause the inner control topology and parameters are unknown to the engineer. Therefore, the impedance tuning method using perturbation and observation is proposed for black-box model to enhance the stability. The changes in eigenvalue explain the effect of variable disturbance on stability. When the real part of eigenvalues decreases, the changes on parameters should be retained to enhance the stability.

The measurement-based impedance model is applicable for specific operating point and it could be different under multiple operating points. Giving tens of thousands of models for a power grid with multiple operating points and making these models available to equipment manufacturers and wind farmer developers/operators would be impractical. Such large amounts of data sets should be clustered and aggregated into a limited number of impedance models. Hence a data-driven automation method for clustering and aggregation of multiple operating point impedance models is proposed. A clustering method based on discrete Fréchet distance (DFD) is proposed to allocate impedance data to different groups. An aggregation method with data shift is proposed to reduce the data size and generate the aggregated transfer function. A data-driven toolbox for stability analysis is developed to make above process be automated and improve system efficiency.

The method of traversing all operating points to determine the system stability boundary is time-consuming, so a fast method for optimizing the stability operating range is needed. Data-driven automation method using a Bayesian optimisation method to determine stability boundary is proposed. Compared with grid search method, this data-driven method selects the next operating point to test based on the experience of previous operating points. The proposed Bayesian optimization method reduce the required number of frequency scan to find stable operating boundaries, especially with a large number of operating points. The user-friendly interface of the toolbox has been developed for engineers to use in a broader range of applications.

Acknowledgements

I want to use this valuable chance to express my acknowledgement and sincerely appreciate all the people who continuously support my PhD study.

I am deeply grateful to my dear friend and supervisor, Professor Xiao-Ping Zhang, for his unwavering guidance, support, and patience throughout my thesis research. His insightful feedback and encouragement were invaluable. Our journey through this research has been more than academic—it has been an adventure of shared ideas, late-night discussions, and unwavering support. His guidance, patience, and belief in my abilities have been instrumental in shaping this thesis.

I want to thank Dr. Dechao Kong for his inspiring academic and industrial discussions and suggestions. I want to thank Dr. Ying Xue for his advice and inspiring talks. Their collaboration places a solid fundamental knowledge of power systems for my future research.

I want to thank Dr Jianing Li, Dr Jiajie Luo, Dr Chenyixuan Ni, Dr Kai Lin, Dr Longmao Fan, Dr. Nan Chen, Dr Xin Ma, Mr Chengyi Wu, Mr Zixuan Jia, Mr Guolong Ma, Mr David Li, Miss Yixin Li, Mr Yiliang Fan. It was my pleasure to work with them.

I want to thank my parents, Mr Jun Dai and Ms Ping Luo. Their unwavering love, sacrifices, and encouragement have been the bedrock of my journey. From the earliest days of curiosity to this moment of accomplishment, their guidance has shaped me. Their belief in my dreams and resilience during challenging times have been my guiding stars. I am forever grateful for the values they instilled, the sacrifices they made, and the love that envelops me. This thesis stands as a tribute to their unwavering support and the countless sacrifices they have made for my education and growth.

Lastly, thank you to all those who believed in me, challenged me, and celebrated with me. This thesis stands as a testament to our collective efforts.

Contents

1. Introduction

1.1 Background and motivation

Renewable energy technologies, including solar and wind power, have received continuous attention and application. To mitigate the environmental pollution problems brought about by traditional fossil energy sources, the future power system with a high penetration level has become an inevitable trend [1]. Figure 1.1 shows the proportion and changing trend of new energy. By 2023, the United Kingdom had over 11 thousand wind turbines with a total installed capacity of 30 GW (half onshore and half offshore). The United Kingdom has world-leading wind energy, with a total installed wind power capacity of 30 GW [2]. Table 1.1 describes the growth of the wind power in UK.

Table 1.1 The growth of wind power in UK

Year	Total Installed Capacity (GW)	Onshore Wind Power Capacity (GW)	Offshore Wind Power Capacity (GW)	Wind Power Generation (TWh)	Employment in the Wind Industry
2018	20.2	13.2	7	57.9	44,000
2019	24.1	14.1	10	64.4	46,000
2020	27.2	14.5	12.7	75.6	48,000
2021	28.7	14.5	14.2	80.3	50,000
2022	30	15	15	85.5	52,000

However, the high penetration rate also led to a series of problems such as wind abandonment, light abandonment, and frequent grid failures, which bring difficulty to stable operating of the modern power systems, for instance oscillations. [3] provides an overview of industry sub-synchronous oscillation (SSO) caused by inverter-based resources (IBR). The deep-seated causation mechanisms leading to SSO were examined, and promising research directions for stress grid requirements globally were proposed. By replicating real-world SSR events, sub-synchronous resonance was investigated in [4] to enhance understanding and develop mitigation strategies.

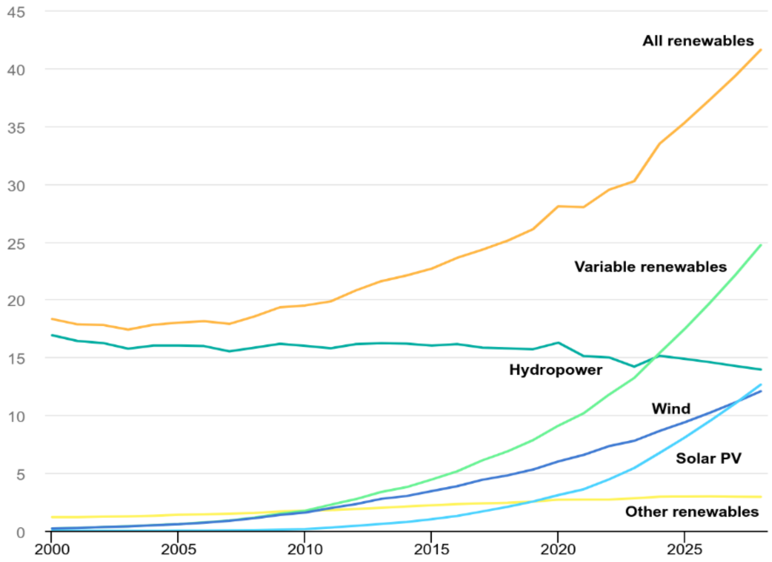

Figure 1.1 Share of renewable electricity generation by technology [5]

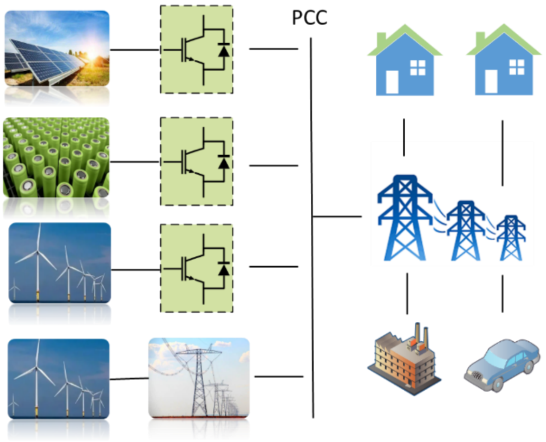

Figure 1.2 Modern power system with a high penetration level

Figure 1.2 shows the topological structure of renewable energy connected to the power grid through inverters. [5] covers various aspects of renewables, including solar, wind, hydropower, and bioenergy and provides a comprehensive report on global renewable energy trends. The insightful work in [6] explores the complexities of power system oscillations. The interconnected areas feature generators, load regions, and transmission lines, providing a rich context for studying oscillations. Different oscillation types include local modes, generator speed fluctuations, and more. In Grid Code GSR018 [7], SSO is a critical concern in power systems, and this document likely provides guidelines, standards, or insights related to their identification, analysis, and mitigation, which is considered to be a valuable resource for practitioners and researchers in the system stability and grid code compliance.

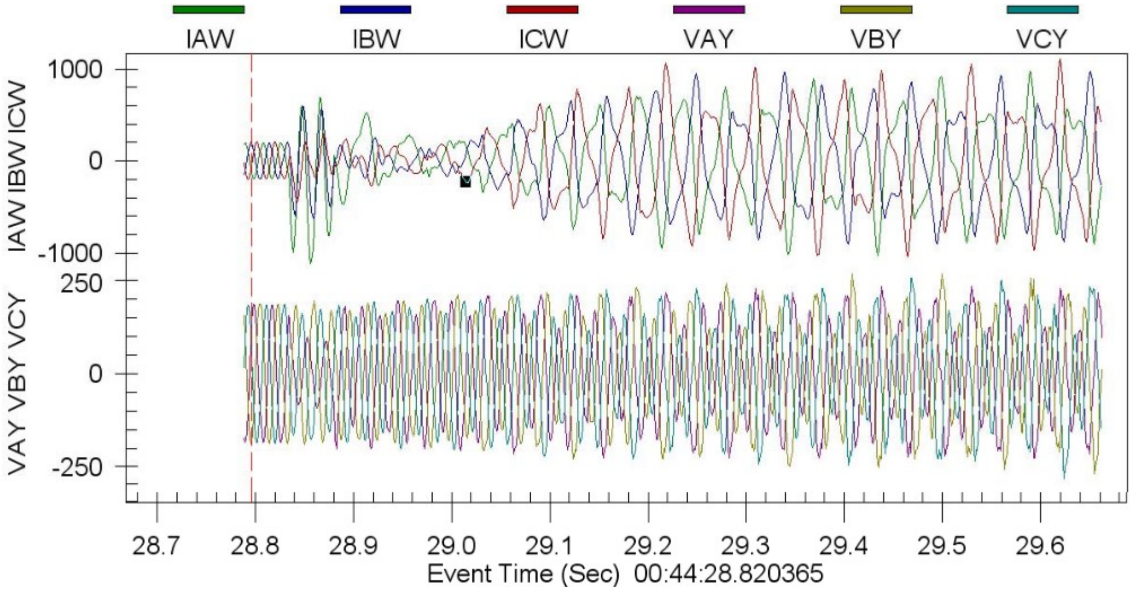

Figure 1.3 Oscilloscope record of sub-synchronous event [8]

Sub-synchronous control interaction (SSCI) occurs when control systems interact with sub-synchronous modes, potentially leading to instability [8], which is shown in Figure 1.3. Real-world scenarios encountered in the ERCOT grid have been discussed, and remediation strategies have been proposed.

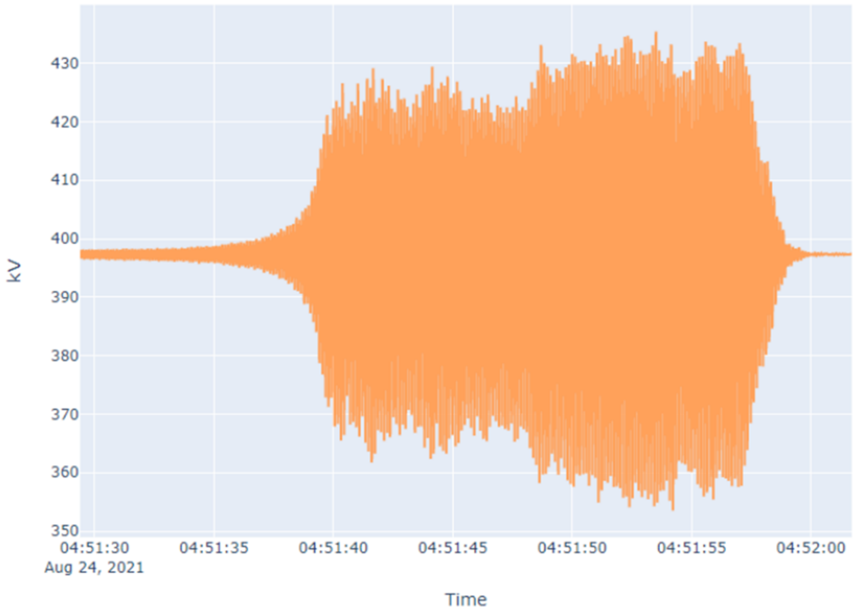

Figure 1.4 Voltage oscillation in Scotland in 2021 [9]

As renewable energy sources become more prevalent, IBRs play a significant role in grid dynamics. The primary disturbance lasted around 25 seconds, and the oscillation frequency was about 8 Hz, the waveform is shown in Figure 1.4.

In the summer of 2023, limited periods of sub-synchronous oscillations, on 5 days across 4 weeks, were recorded on the GB transmission network [10]. The recorded oscillations had a higher magnitude and impact on the transmission network in Scotland compared to that recorded in England and Wales. The investigation found no evidence to suggest that the cause of these events is directly linked to system inertia, short circuit levels or any specific type of generation. The investigation concluded that a particular asset was the major contributor to the sub-synchronous oscillations event.

The occurrence of the above accidents is closely related to the high penetration level of renewable energy onto the network. The high penetration of renewable resources is often intermittent, random and fluctuating, and the equivalent grid impedance often fluctuates dramatically, which makes the grid show a weak or even very weak grid characteristic and this brings severe difficulty to the stable operation of the inverted-based power system. As the core equipment of renewable resources, the grid-connected inverters reduce the damping and inertia which were originally provided by synchronous machines, often leading to stability problems. The control interaction between inverters and grids leads to power system oscillations. The topology and control parameters of the inverters are usually challenging to obtain, while the system complexity and dynamics of large grids are difficult to access through detailed modelling. Nowadays, the motivation is to understand the causes of SSO and propose methods to mitigate the power system instability issues caused by grid-connected inverters.

1.2 Literature review

1.2.1 Inverter-based resources

The REN21 serves as a global platform that unites industry and academia groups [11]. Its mission is to foster knowledge exchange and facilitate the rapid adoption of renewable energy technologies across developing and industrialized nations. Compliance with protection standards is essential in distributed units connected to the power system via static generators [12]. These units must incorporate an interface protection device tailored to satisfy specific requirements dictated by relevant standards [13]. On the grid side, control mechanisms play a pivotal role. These controllers manage critical functions, including regulating active and reactive power flow, maintaining frequency and voltage stability, achieving synchronization, overseeing the DC link, and ensuring sustainable and stable power injection [14].

The stability and reliability of the interaction network heavily depend on the design of the inverter controller. When the controller lacks robustness, issues of instability and disturbances arise. To ensure accurate functionality and high stability, the choice of control strategy plays a crucial role. The inverter control involves internal and external loops. The internal loop is the fast current loop, and the external loop is the slow voltage loop. The current loop manages grid current, affecting current protection and power quality levels. Meanwhile, the voltage loop regulates the DC link voltage, ensuring stability in the slow dynamic system. Grid-side controllers fall into various categories and will be presented later.

Additionally, evaluating grid-connected inverter performance is essential for efficient solar or wind power plants. Critical criteria include power quality, which assesses distortion to meet system requirements such as total harmonic distortion (THD). Voltage regulation is to ensure the inverter maintains grid voltage to satisfy the requirement under multiple load conditions. The power factor means achieving a unity power factor to minimize grid loss. Frequency control is to verify synchronization with grid frequency and adjust accordingly. Phase angle control also aligns the phase angle with the angle of the grid. Efficiency measurements also contribute to system optimization.

（1） Linear control

Linear controllers, rooted in classical feedback control theory, leverage the dynamics and properties of linear systems. Conventional control falls into this category within the realm of photovoltaic (PV) systems. The main classical control technique, proportional (P) control, adjusts the control signal proportionally to the difference between the expected and real output. Proportional integral derivative (PID) Control combines proportional, integral, and derivative actions to enhance performance. Proportional integral (PI) Control: Integrates error over time to eliminate steady-state errors. Proportional derivative (PD) Control: Incorporates derivative action to improve transient response. These classical controllers are widely use in applications due to their simplicity in plan. When applied to current-controlled voltage source inverters (VSIs), they exhibit limitations in high-frequency performance.

（2） Robust control

Many nonlinear aspects in the power system are difficult to simulate by linearization. Robust control addresses controller design in the presence of uncertainties. Robust control methods ensure proper functioning when dealing with system parameters, disturbances, and outer factors. Within this system, well-known variations fall into several categories. Linear fraction transformation (LFT) [15] means that robust control relies on describing these uncertainties. It effectively separates the nominal system part from the uncertain portion. Attractive features include: (1) Disturbance Rejection: Robust control can handle disturbances while maintaining set point tracking. (2) No Prior Knowledge Needed: It doesn't require prior knowledge of uncertain inputs. (3) Performance and Stability: Robust control ensures good performance and stability in closed-loop systems. However, robust control is not suitable for sudden operating condition changes. Some standard techniques exist in Mu-Synthesis that enable robust multivariable controller design for complex linear systems with various uncertainties. H-Infinity methods are applied in the voltage source converter (VSC). For instance, the H-infinity controller effectively reduces THD in output current [16]. The controller may lead to slow dynamic responses, which is the drawback [17].

（3）Non-linear control

In power systems, nonlinear control strategies including Sliding mode control (SMC) and hysteresis current control (HCC) offer distinct advantages over linear counterparts. SMC exhibits robustness against disturbances and parameter variations [18]-[19] and it ensures an invariant steady-state response even for varying PV systems. However, the performance hinges on two critical parameters. Identifying suitable parameter values remains a challenging task, constituting a critical drawback. Additionally, SMC-controlled PV systems may suffer from chattering phenomena and increased power loss [20]. Researchers proposed solutions to address chattering. In [21] and [22], novel SMC techniques based on artificial intelligence were described. These approaches reduce system chattering by estimating uncertainties in real time.

Complete linearization control transformed nonlinear systems into partially or fully linear ones [23].

In the context of grid-connected systems, HCC emerges as a valuable nonlinear control method. Hysteresis current control is a measure employed within the current control loop of interconnected systems [24]. Its primary goal is to achieve a fast dynamic response while ensuring robustness against load variations. The implementation of HCC is straightforward, and it offers advantages:

- Current Limitation: It effectively limits the output current.
- Simplicity: The control strategy is easy to implement.
- Robustness: It handles varying operating conditions. The core concept revolves around defining a “hysteresis band”. The inverter’s switches are then controlled to maintain the output current within this band. While HCC provides a rapid transient response, it faces challenges related to switching frequency variation due to the chosen hysteresis band and operating conditions.
- Overcoming Hysteresis Controller Drawbacks: Researchers have proposed solutions to enhance HCC [24].
- Sinusoidal Variation: In [25], the switching frequency remains constant which results in reduced output current fluctuations and power ripple.
- Constant Switching Frequency: [26] achieved a steady switching frequency without directly controlling the hysteresis band.

HCC balances simplicity and dynamic performance in grid-connected PV systems, and ongoing research aims to optimize its effectiveness.

In summary, nonlinear control methods, while powerful, require careful parameter tuning, and ongoing research seeks to enhance their effectiveness.

(4) Artificial intelligent (AI) control

These AI Control methods, inspired by human intelligence, do not rely on explicit system models for controller design. They can approximate nonlinearities, making them versatile for various applications. Over the past years, AI techniques have been widely adopted within power systems.

- Forecasting: Predicting load demand, renewable energy generation, and market prices.
- Designing: Optimizing system components and layouts.
- Maintenance: Detecting faults and ensuring reliability.
- Control: Enhancing system performance and stability.

Results indicate that AI-assisted tasks exhibit enhanced efficiency and accuracy compared to traditional approaches. These strategies fall into two leading families: Artificial Neural Network (ANN) control utilizes interconnected neurons to approximate complex mappings. Fuzzy Logic Control (FLC) handles uncertainty and imprecision using linguistic rules. In summary, AI control methods empower modern power systems by leveraging intelligence without relying on explicit models.

Researchers have proposed various ANN techniques to address control and identification challenges. The main advantages of ANN-based controllers include treating the objective as a black box and eliminating the requirement on the model mathematically. Data-Driven training can utilize real-world data from actual plants, even when system knowledge is limited. Improved performance compared to classical controllers through accurate tuning of ANN-based strategies. In [27], the authors presented a novel control strategy by leveraging ANNs. This approach enhances the system's ability to withstand low voltage conditions during grid disturbances. In summary, ANNs offer flexibility, robustness, and improved power converter control and identification performance, making them valuable tools for modern energy systems.

The low voltage ride through (LVRT) ensures that the connection between the PV system and the grid remains intact even during voltage drops. The proposed approach employs a neural network (NN) to classify grid faults. A model predictive controller (MPC) adjusts the injected reactive power accordingly with a fault. Results demonstrated that this technique adheres to grid code specifications and maintains efficiency during voltage drops. In [28], an MPC strategy was proposed for a three-phase inverter with an output LC filter, which aims to minimize THD and enhance steady-state and dynamic response. The MPC controller serves as an expert system for offline training of the NN, which ensures accurate output voltage tracking. Overall, this ANN-based control exhibits satisfying static and dynamic performance across diverse operating conditions. While effective, this control method faces challenges: It's sensitive to the dimensionality of input data. Initial choices for weights and functions impact performance. Sufficient training data is essential to satisfy the large training data requirement. A visual representation of the basic Neural Network control scheme is proposed in [29]. In summary, ANN-based control strategies offer promise but require careful parameter tuning and robust training.

In recent decades, the FLC technique has garnered attention in power converters for PV applications. FLC controllers stand out due to their adaptive nature. They can add or modify rules, allowing for continuous improvement of system performance. Among various intelligent controllers, FLC is the simplest for inverter control [30]. In [32], the authors present a fuzzy-based inverter controller. The goal is to mitigate output fluctuations and address nonlinearity properties. The results demonstrate very low voltage and current THD. In summary, FLC offers simplicity, adaptability, and robust performance in PV system control.

Furthermore, researchers have explored evolutionary algorithms (EAs) to tackle challenges related to PV systems. In [33], the authors compared different approaches for maximum power point tracking (MPPT) in PV systems. [34] proposed a modified version of the particle swarm optimization (PSO). The goal is to implement an adaptive MPPT for centralized-type PV generators operating under partial shading conditions (PSC). The focus is on improving tracking speed and accuracy. In [35], a genetic algorithm (GA) method was introduced to enhance the lifetime. The evolutionary algorithm optimized the weights of a back-propagation (BP) neural network PID controller. [36] proposed a Volt-VAR control algorithm for optimizing voltage regulation. Historical operational data and reinforcement learning methods are leveraged to balance voltage stability and operational costs. Evolutionary algorithms are crucial in enhancing system performance and addressing various control challenges.

(5) Performance and future trends

The control strategy selection relies on demands encompassing desired performance. When choosing the suitable control method, there is a need to consider a balance among performance, complexity, and implementation requirements. Linear control techniques, rooted in linear mathematical models, prove relatively straightforward to implement and enjoy widespread use in grid-connected inverters. While offering commendable steady-state performance and stability, they fall short in handling nonlinearities. Generally, linear control methods lack the efficiency seen in more advanced counterparts, unable to optimize for dynamic operating conditions. Furthermore, they may encounter power quality issues, including exhibit limited scalability. Despite being simple and having low requirements on computational resources, linear control methods incur lower initial implementation costs.

Artificial intelligence algorithms and intelligent control methods learn to a certain extent about dynamic characteristics that are difficult to simulate with conventional control methods. However, this technology is usually tricky to model accurately through mathematical expression. The selection and randomness of some initial states in the model can also affect the repeatability of the results to some extent.

Based on the above review, the current situation for grid-connected inverters is clear, and the research gap is summarized.

- Accurate modelling of grid-connected inverters is essential for control. The state-space model represents dynamic behaviour and interactions within the system but requires details. Besides, it would be hard to build a state-space model due to the high complexity.
- Modern control methods, such as neural networks, are difficult to model mathematically directly which bring challenges to further analysis.

1.2.2 Impedance modelling techniques

The challenges of integrating inverter-based resources into modern power systems are addressed in [37]. These resources include wind farms, photovoltaic and energy storage devices. The authors proposed technology pathways to incorporate these resources into the grid effectively. The paper is a valuable resource for understanding the evolving landscape of power systems with IBR.

Reference [38] provided valuable insights into the modelling and analysis of three-phase dynamic systems. It covers various components, including AC machines, passive elements, and power electronic converters. The focus is on utilising detailed transfer functions (TF) and matrices to describe system behaviour, which contributes to understanding frequency-domain analysis and stability theory. [39] provides a unified general phasor transformation method with AC systems. This technique simplifies the analysis and modelling of converters, enhancing their performance and control. A modified sequence-domain definition was proposed in [40], which was compared with the dq-domain impedance definition. This work contributes to stability analysis in power systems. The authors introduced an asymmetric complex-vector framework specifically applied to control interactions [41]. These models enhance the understanding of converter behaviour in grid-connected systems. A comprehensive approach to modelling the entire system was developed by embedding frame dynamics, considering synchronous and asynchronous components [42].

[43] was focused on impedance modelling and analysis of VSC. It provided insights into the behaviour of these converters within the power system. The impedance of inverters with dq frame is analysed in [44], which concludes that the impedance characteristics are crucial for control design. [45] was focused on grid admittance identification for active distribution networks and provides techniques to enhance grid stability according to impedance stability theory. An improved strategy using measuring the impedance of grid-connected systems was presented, accounting for background harmonics and frequency deviations and improving accuracy [46].

By explicitly revealing the nature relations in different domains using complex TF and space vectors, the authors presented a stationary (αβ-) frame [47]. This model predicted the stability effect of the phase-locked loop (PLL) and explicitly characterized the frequency coupling effect. Harmonic linearization [48] and the harmonic state-space (HSS) [49], [50] directly linearized the converter systems in the αβ frame. [51] focuses on these complex-valued AC impedance modelling for converters, explicitly considering the impact of zero-sequence circulating current. The study provides valuable insights into the behaviour of modular multilevel converters (MMC), which play a crucial role in high-voltage direct-current (HVDC), renewable resources integration, and other systems. [52] revealed the impedance relationships under different coordinate systems and how they could facilitate stability analysis. The harmonic transfer function-based stability analysis method was applied to unbalanced networks in reference [53]. The model works typically for specific conditions but is not applicable for analysis when the operating point changes.

Based on the previous introduction, the significant research gaps are summarized as follows:

- The existing impedance model may only work for specific operating conditions and is unsuitable for dynamic power systems.
- Developing a robust impedance model to trade off efforts and accuracy which is applicable to white-box model and black-box model.

1.2.3 Impedance-based stability analysis

Inverters can be used to connect wind power, PV and other renewable resources to the AC power system. With the rapid increase of their proportion, the stability problems involved or dominated by converters are highlighted in this section. For example, many converter-type new energy units connected to the grid under a weak system result in the problem of sub/supersynchronous oscillations, which was investigated in [54]. Some developing trends on challenges, control strategies, and renewable energy integration have also been discussed.

The stability criterion for interconnected systems was initially proposed in [55], focusing on ensuring the stable operation of inverters within the grid. [56] investigated stability in multi-infeed power systems considering system strength evaluation. Modelling techniques and stability challenges specific to voltage-source converter-dominated power systems were explored in [57], which covers control strategies and stability analysis.

The fundamental plan is to check if the impedance ratio identified from the interaction network satisfies the Nyquist stability theory, which is equal to the theory of identifying a close loop with all poles in the left half plane (LHP) [58]. Stability criteria will vary slightly depending on impedance sum or ratio [59]. Stability was evaluated by the location of the zeros of the characteristic equation in systems with cascaded voltage sources [60]-[61]. The passive input admittance indicated power system oscillation [62]-[64]. Tuning the control parameters to reduce the frequency range of the negative resistor is another solution [65]-[67].

Based on the literature review in Section 1.2.3 Impedance-based stability analysis, the current challenge includes the following aspects:

- Lack of systematic analysis of enhanced system stability from an impedance perspective.
- The linearized impedance model is only suitable for stability analysis at specific operating points which brings limitation to the stability analysis.
- Determining system stability through bode plots is more complicated.

1.2.4 Impedance-based stability reinforcement

When the power system oscillation happens, corresponding measures need to be taken to suppress the oscillation and enhance system stability. The output power, control strategy & parameters adopted, and the system strength influence the system oscillation characteristics [68]. The dominant oscillation mode of the renewable resources after the grid connection was analysed with the grid parameters, and then the variation rules of the oscillation frequency and damping with the operating conditions, grid strength and control parameters were investigated [69]. More specifically, some mitigation measures for instability have been taken into consideration. The dominant methods include optimizing control parameters and reshaping the control topology and additional equipment [70].

However, the impedance of the grid side is normally challenging to adjust according to the operating conditions of the inverter. Therefore, to enhance the stability of the interconnected system, new energy resources connected to the system are usually adjusted. After obtaining the impedance model of the grid-connected inverter and the power grid, the impedance stability analysis of the interactive system is performed, and a theoretical basis for the impedance stability control will be provided. When controlling the character of an interactive system, the impedance shaping methods include:

(1) Control parameter optimization method.

proposed a novel method to enhance stability in quadrature-axis control. A novel control is introduced with MVDC systems [71]. Under weak grid conditions, [72] investigates control strategies for grid-connected inverters using impedance reshaping in the q-axis. The system was optimized so the grid-following inverter operates stably under low system strength [73]. The tuning strategy for current control and PV/PQ control was adopted to connect with a weak grid. The optimization guidance can be concluded from impedance measurements, which leads to eigenvalues that are far away from zero axes.

(2) Impedance structure reshaping method

Grid-forming control become popular nowadays because of its superior stability performance in weak grids [74]-[78], whereas it could also trigger stability issues when it is applied to a robust grid [79]. The stability analysis has been implemented with the state-space model [80]-[81] and the impedance-based model [82]-[84], which lacks sufficient shaping guidance when operating under different penetration levels.

In interactive systems, impedance structure reshaping methods mainly include active damping, changing controller type, and virtual impedance. [85] adopted changing the controller type. It proposed a structure to use multiple PR controllers to reshape the dq-axis output of the grid-connected inverter, which can reduce the harmonic interference gap between interconnected systems to ensure the system's stability. [86] proposed an active damping method based on different feedback points. Different types of compensators are used according to different feedback points so that the return rate matrix at each connection satisfies the Nyquist criterion. [87] added the virtual impedance and realizes the series and parallel correction of the output impedance through the feedforward PCC point voltage, ensuring the sustainable operation. Stability issues related to DC resonance are investigated and a reshaping method is developed to mitigate resonance effects [88]. In [89], a simplified impedance-based stability criterion was used in DC cascade systems. A novel double-PLLs-based control is designed to extend the stability range of grid-following inverters operating without losing fast dynamic response [90].

(3) Addition of ancillary equipment to the system.

When impedance shaping of the interactive system based on impedance parameter optimization and structural reshaping methods are usually carried out within the inverter and grid-interactive system, the interaction stability is optimized by improving the impedance characteristics of the inverter. In addition, existing power devices outside the interactive system can be used, or additional power equipment can be connected to improve system stability further and achieve system-level impedance control. The impedance model introduces the mechanism of oscillations, and modifications are made using a synchronous condenser. The synchronous condenser is more effective than STATCOM in stabilizing the system [91].

In summary, when reshaping the interactive system impedance model, the impedance parameter optimization can be adopted to improve the grid-connected inverter's output impedance characteristics so that the interactive system's impedance stability has a certain degree of robustness. The impedance structure reshaping method reconstructs the impedance model of the interactive system to achieve adaptive adjustment of impedance characteristic control; the system-level impedance control is helpful to enhance the stability of the interactive system further, providing a new damping control idea for impedance control. Since the impedance reshaping method extends the interactive system's stability margin and achieves optimization of the interactive system, the solution is promising with impedance stability analysis.

Based on the literature review in Section 1.2.4 impedance-based stability reinforcement, the current challenge includes the following aspects:

- How to determine the boundary of stable operation when the control parameters of the inverter are unknown.
- It can be challenging to pinpoint the exact root cause when instability occurs using impedance-based approaches.

1.2.5 Data-driven optimization approach

When the structure and control of the inverter are unknown, the frequency domain data of the inverter is obtained by frequency scanning. Further, the impedance data is used to estimate the transfer function. However, the small-signal model is only applicable at specific operating points. To get the inverter's full state impedance, many operating points need to be scanned to create a database. The analysis methods only employ the database and no longer need the mathematical model is called the data-driven approach. The non-invasive method monitors the stability condition of a system and detects any changes in its behaviour. The technique has already been implemented in broader industrial applications.

Since the control block and parameters are unknown, it could be a black box model. Further, the parameters of the operating point are assumed to be the inputs of the black box model, and the eigenvalues of the system obtained from the frequency scanning can be considered the outputs of the black box. In industry, it is required to determine the range of the stable operation of the inverter, and this objective can be transformed into a black-box optimization. It is a significant growing field that deals with problems where the objective and constraint function values are available as outputs [92]. [93] utilizes evolutionary programming and radial basis functions for high-dimensional constrained optimization problems.

General impedance-based stability analysis relies on robust models with proper identification methods. Data-driven methods to assess grid impedance are utilized under varying frequency conditions to obtain multiple event data [94]-[98]. No prior power system knowledge or complex modelling was required, a black-box method is proposed in [99] that acquired power grid characteristics through frequency-domain identification by the inverter itself. The power-frequency dynamics of grid-forming inverters were explicitly reshaped to ensure synchronization. Python scripts enabled automation simulation, significantly reducing the effort of large amounts of operating points [100].

A large amount of impedance data constitutes a data set, with the operating point as the input quantity and the impedance curve as the output quantity [101]. The neural network can be used to predict the impedance curve at a specific operating point. The neural network obtained through training can be transplanted for feature extraction of other inverters [102]. A Data-driven approach using support vector machines (SVM) to create a generalized impedance model for IBRs was proposed in [103]. However, currently it requires a long time to set up models for different scenarios and obtain a large amount of impedance dataset at multiple operating points.

Based on the review in Section 1.2.5, the research gaps can be identified as follows:

(1) Current methods for evaluating data similarity are not applicable to evaluating inverter impedance models.
(2) Mainstream clustering methods have difficulties in clustering data under multiple operating points.

(3) The comprehensive understanding of the stability of grid-connected inverters under varying operating points lacks deep research.

(4) Existing automation toolkits are only applicable to specific scenarios and lack of portability. There is a lack of research on reducing the number of operating points to improve the efficiency of impedance stability analysis.

1.3 Objectives

According to the literature review and research gaps identified in Section 1.2, intrinsic causes of oscillations and control optimization need to be appropriately implemented to achieve stability in high-penetration power systems. The challenges of impedance modelling and stability analysis methods will need to be researched. Hence, the objectives of this thesis are:

(1) to develop a measurement-based impedance modelling method with appropriate guidance.

(2) to propose a two-stage stability assessment method including preliminary screening and impedance-based stability analysis that achieves a balance between time cost and accuracy in assessing stability issues of power systems with renewable energy.

(3) to reveal the relationship between the impedance model and the state-space model and to propose an auxiliary control to reinforce the stability of the interconnected system and expand the stable boundaries of system operation in terms of impedance reshaping.

(4) to propose an impedance-based stability analysis approach that is applicable to black-box systems and provides tuning guidance on impedance under multiple operating points.

(5) to develop a data-driven automation method for clustering and aggregation of multiple operating points impedance models which can reduce the data size and provide aggregated transfer function for practical applications.

(6) to develop a data-driven automation method using Bayesian optimisation to determine the stability boundary of the interconnected power system and improve system performance by reducing the number of frequency scan.

1.4 The thesis outline and contributions

The research is conducted via theoretical derivation and simulation verification. The main contents of the thesis are divided into eight Chapters as follows:

Chapter 1 starts with an introduction to background and motivation, and then carries out the literature review. Based on the review, the objectives are presented, and the contents are highlighted.

Chapter 2 introduces the modelling technique for grid-connected inverters. Then, the mathematical impedance model is developed and validated using simulation. Besides, the impedance model could be obtained with measurement data. Therefore, the procedure of the impedance measurement is given. Some proper guidance is provided to trade off the efforts and accuracy.

Chapter 3 proposes a preliminary screening method to reveal potential threat points prone to instability. The definition of short circuit ratio and system strength are presented to indicate if the system is strong or weak. Then, the fundamental stability theory is introduced, and its advantages are emphasized. Case studies are implemented to validate the impedance-based stability analysis.

Chapter 4 investigates characteristics of inverters with mathematical modelling. The state-space model and impedance model cross-check each other. The reshaping of the impedance curve leads to stable operation. It is known that tuning control parameters may mitigate the instability issue and the auxiliary control also enhances the stability. Proper strategies are proposed to expand the boundaries of stable operation and further verified by simulation.

Chapter 5 deals with the limited information on the inverter, which is treated as a black box. Hence, the measurement data is built up to investigate the characteristics of the inverter. The real part of eigenvalues moving towards the right indicates the change of system parameters weakens the stability of the interconnected system. The tuning method is proposed to enhance the stability of interconnected systems when the black box inverter is connected.

Chapter 6 utilizes a data-driven method to represent a very large amount of impedance models corresponding to multiple operating points. In the data-driven framework, a novel clustering method based on discrete Frechet distance (DFD) is proposed. An aggregation method based on data shift is proposed to merge data without losing the characteristics of the original data. Finally, an automation toolbox for stability analysis is developed and its characterizations are presented.

Chapter 7 introduces the three optimization methods and makes a comparison among them. The black box optimization with Bayesian theory is proposed to determine the stability boundary and reduce the number of simulations runs. A toolbox was developed that eliminates the need for the user to manually run a large number of simulations.

Chapter 8 summarises the key findings of the research and concludes with the main content. One individual section highlights the contributions and presents the extent of promising research.

The relationship among each Chapter of this thesis is summarised in Figure 1-5:

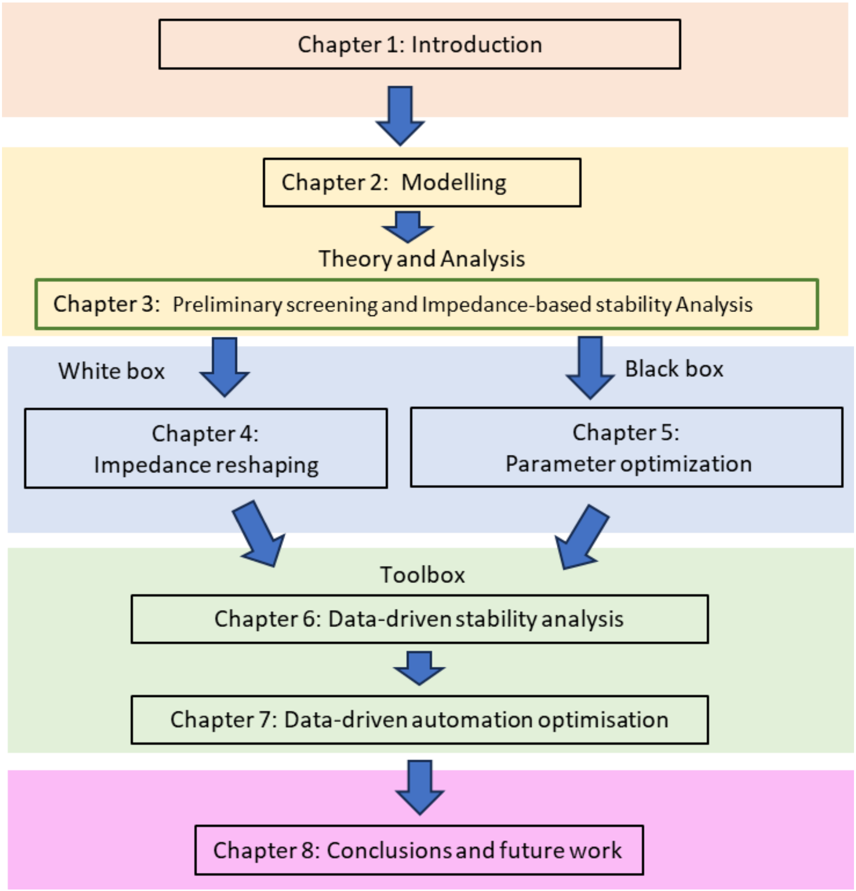

Figure 1.5 Relationship among Chapters of this thesis

Figure 1.5 shows the overview of the whole thesis. Chapter 1 introduces the challenge and key research gaps as well as research objectives. Then, the system modelling and impedance-based stability analysis are presented in Chapters 2 and 3. Chapter 4 deals with the white box and the proposes impedance reshaping method. Besides, Chapter 5 aims at increasing the stability of the black box model by reshaping the impedance of an inverter. A data-driven impedance modelling method with multiple operating points by clustering, and aggregation is proposed in Chapter 6 and a related toolbox is implemented. Black box optimization is proposed to find the stability boundary and a data-driven method is proposed and a related toolbox is developed in Chapter 7. Conclusions and future work are summarized in Chapter 8.

1.5 Publications

[1] S. Dai and X.-P. Zhang, "Advanced Identification Methods for Power System Oscillations based on Measurements," 2022 IEEE 16th International Conference on Compatibility, Power Electronics, and Power Engineering (CPE-POWERENG), Birmingham, United Kingdom, 2022, pp. 1-6, doi: 10.1109/CPE-POWERENG54966.2022.9880879.

[2] S. Dai, C. Wu, D. Li, D. Kong, X. Zhou, and X.-P. Zhang, "A Methodology to Derisk HVDC and Offshore Wind Connections to a Network", CIGRE Paris Session 2024.

2. Impedance modelling on grid-connected inverter-based resources

2.1 Introduction

A system designer usually has no access to detailed data on the power converters, due to the confidentiality of manufacturers. To understand the characteristics of the model, impedance measurement techniques are required.

This Chapter presents impedance modelling methods with state space equations and measurement data, respectively. A brief comparison of the two different modelling methods is given in Section 2.2. Then, the procedures for building the impedance by derivations are provided in Section 2.3. Additionally, the guidance on impedance measurements is presented in the case study in Section 2.4. Finally, the results from the two different methods are compared and validation of the modelling methods is presented in Section 2.5. Finally, the summary is presented in Section 2.6.

2.2 Modelling of grid-connected inverters

When evaluating the stability of grid-connected inverters, prevailing methods can typically be categorized into state-space (SS) methods and impedance analysis methods. The state space method, employed for stability analysis, mandates the acquisition of all parameters related to both the grid-connected inverter and grid components. This is crucial for formulating a comprehensive state-space model. Subsequently, characteristic equations and eigenvectors of the state space model are scrutinized to ascertain the stability of the grid-connected inverter system. The efficacy of the state space method hinges on the completeness and certainty of the grid-connected inverter system during stability analysis. Any alterations in system components or parameters necessitate the re-establishment of the state space model for the updated network. In a grid-connected system featuring distributed power generation, the dynamic nature of component units, with potential changes in structure and parameters at any given time, complicates system analysis using the state space method.

In a bid to streamline and enhance the establishment of models and stability analysis for grid-connected inverters, the impedance analysis method has been introduced. With the impedance stability method, both the grid-connected inverter and the grid-interactive system are treated as independent subsystems. Impedance models are built for each subsystem based on their unique control structures and parameter characteristics. The beauty of this approach lies in the autonomy of each subsystem; alterations in the structure or parameters of one do not impact the other. Consequently, re-establishing the impedance model is not required, simplifying the intricacies of system analysis. After obtaining the impedance model, a linear network structure is employed to depict the equivalent circuit of the interactive system. The subsequent application of impedance stability criteria facilitates a thorough analysis of the system's stability.

Table 2.1 Comparison of modelling methods

Items	**State-space model**	**Impedance model**
Description	The eigenequations and eigenvectors of the state space model are analysed to determine the stability.	Only the terminal impedances of subsystems are required and thus facilitate the stability assessment for the “black box” systems.
Features	Known structure and parameters.	Mathematical model or measurement model

2.3 Impedance modelling

The impedance model is a small-signal model in the frequency domain. In this work, the impedance model is developed with the harmonic linearization method in the frequency domain. Meanwhile, since the system oscillation frequency is mainly less than 100Hz and the switching frequency of the system is high, the delay is ignored in the impedance modelling.

The overall idea of the harmonic linearization method to model the impedance of the two grid-connected subsystems is to assume that the positive and negative sequence voltage harmonics and current harmonics are present at the grid connection point of the grid-side inverter at a specific frequency and the relationship between the positive and negative sequence voltage and current harmonics is established by the system's grid-connection parameters, control structure, and rated operating conditions to obtain the positive and negative sequence voltage and current harmonics of the grid-side inverter. Inverter impedance modelling is the most basic part of impedance modelling for different new energy grid-connected power units. All the inverter-based power units connected to the grid can be represented by a universal impedance model, which can be derived from the state space model of the inverter.

2.3.1 Main circuit of grid-connected inverter

The typical interconnected system with a scan module is shown in Fig. 2.1. The inductor L serve as AC filter inductance. The PLL is used in the grid following control to track the voltage synchronous reference θ_{PLL}, And the current controller produces output voltage reference according to current reference and actual current. In the impedance modelling process, the sampling delay is ignored for simplicity, and the performance of the converter is idealized by assuming that the output voltage can perfectly track the voltage reference.

The AC side currents and voltages of the converter are denoted as i_a, i_b, i_c, v_a, v_b, and v_c. The mathematical model is given in (2.1).

$$L\frac{d}{dt}\begin{bmatrix} i_a \\ i_b \\ i_c \end{bmatrix} = \begin{bmatrix} v_a \\ v_b \\ v_c \end{bmatrix} - \begin{bmatrix} e_a \\ e_b \\ e_c \end{bmatrix} \tag{2.1}$$

where v_a, v_b, and v_c represent the converter output voltage.

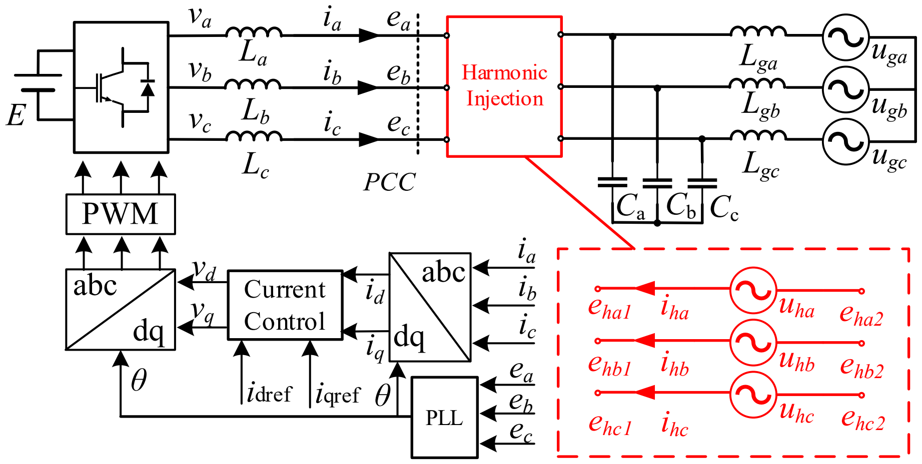

Figure 2.1 The control and harmonic injection for grid-connected inverter

2.3.2 PLL

Fig. 2.2 describes the typical control diagram for PLL. The transfer function of the PLL with PI regulator is given in Eq (2.2).

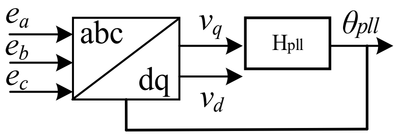

Figure 2.2 The basic block diagram of the PLL

$$H_{PLL} = (k_{pp} + k_{pi}/s)/s \tag{2.2}$$

where k_{pp} and k_{pi} are proportional and integral coefficients, respectively.

2.3.3 Current control

The basic current control block is given in Figure 2.3. The current reference is output from the voltage control loop. Equation (2.3) gives the transfer function of PI controller.

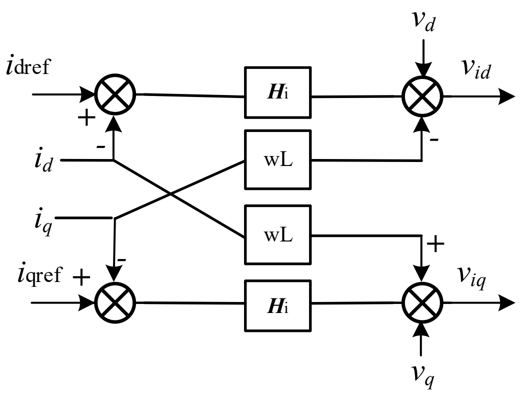

Figure 2.3 Basic block diagram of current control

$$H_i(s) = k_{ip} + k_{ii}/s \tag{2.3}$$

where k_{ip} and k_{ii} are proportional and integral coefficients, respectively.

The analytical mathematical equations, namely, positive-sequence impedances for the inverter in Figure 2.1 are shown below:

$$Z_p = \frac{H_i(s-j2\pi f_1)-j2\pi f_1 L+Ls}{1-\frac{T_{PLL}(s-j2\pi f_1)}{2}[\frac{I_1}{V_1}e^{j\theta_{i1}}H_i(s-j2\pi f_1)+1]} \tag{2.4}$$

$$T_{PLL}(s) = \frac{V_1 H_{PLL}(s)}{1+V_1 H_{PLL}(s)} \tag{2.5}$$

where V_1 is the phase voltage amplitude, I_1 is the current reference amplitude, θ_{i1} is the current reference phase, and f_1 is the fundamental frequency. Many determinants affect the impedance curve. This explains why the same inverter could become unstable due to the gird changes.

All the inverter-based power units connected to the grid can be represented by universal impedance models shown in Equations (2.4) and (2.5), and these can be derived from the state space model of the inverter as depicted in Figure. 2.1.

2.4 Impedance model based on measurements

The main common methods for stability analysis are the state space method and the impedance method. The state-space models the system in the time domain by calculating the eigenvalues and performing stability analysis based on their positions in the complex plane, which is only applicable to white-box systems and requires complete system parameters, which is impractical. The impedance method models the system in the frequency domain by scanning the voltage-current characteristics of the ports to obtain the impedance and establish the transfer function and performs stability analysis using the Nyquist criterion, which is suitable for black-box systems and detailed information of the internal parameters is no longer needs. In this section, the measurement-based impedance modelling approach is described, and recommendations are given for key issues in the implementation.

2.4.1 Overall framework of impedance model based on measurements

The overall scheme is to inject the voltage component at one frequency at a time, output the impedance value at that frequency, and utilize the multi-run component to change the injected frequency at each run so that the impedance characteristics of the frequency band can be obtained at the end of one's setup, which includes perturbation injection, voltage and current acquisition, Fourier transform, impedance calculation, and multi-run operation.

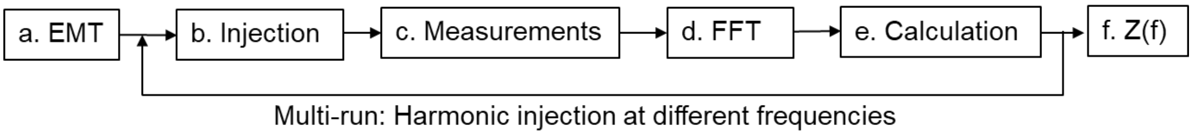

Figure 2.4 Main steps of impedance measurement

Step 1: Stable condition in EMT simulation;

Step 2: Voltage injection at the PoC point;

Step 3: Voltage and current measurements;

Step 4: Data conversion with FFT module;

Step 5: Calculation the magnitude and phase angle;

Step 6: Frequency response data output.

The flowchart shows the voltage disturbance injection process while the data collection is shown in Figure 2.5 below.

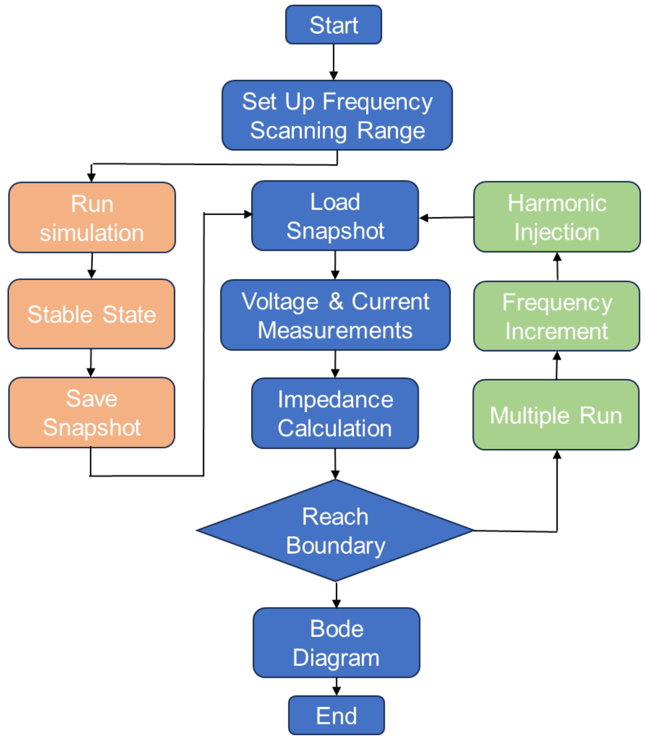

Figure 2.5 Impedance Measurement Flowchart

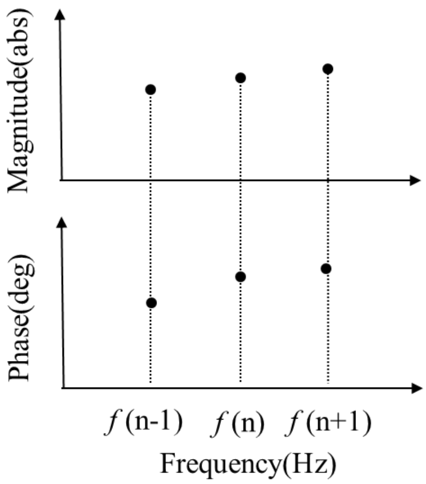

Figure 2.6 Bode Plot from Impedance Measurements

The frequency domain impedance data is then imported into Matlab to estimate the transfer function. Then, the eigenvalues are calculated with the transfer function, and they are compared with the results from the state space model.

2.4.2 Proper injection magnitude

One concern is what the appropriate amplitude for the injection harmonics is to implement the impedance measurements. A large disturbance signal may affect the operation point, leading to trouble, whereas the small harmonics also lead to non-smooth impedance curves. Some attempts are implemented to receive guidance on the amplitude. Slightly increasing the amplitude of the harmonic injection at each time and observing the results until a significant change happens. It should be noted that this initial conclusion may be various when it comes to other scenarios. The motivation to do this investigation is to plant the multiple harmonic injections when it comes to a large number of conditions which will take effort to obtain the impedance data.

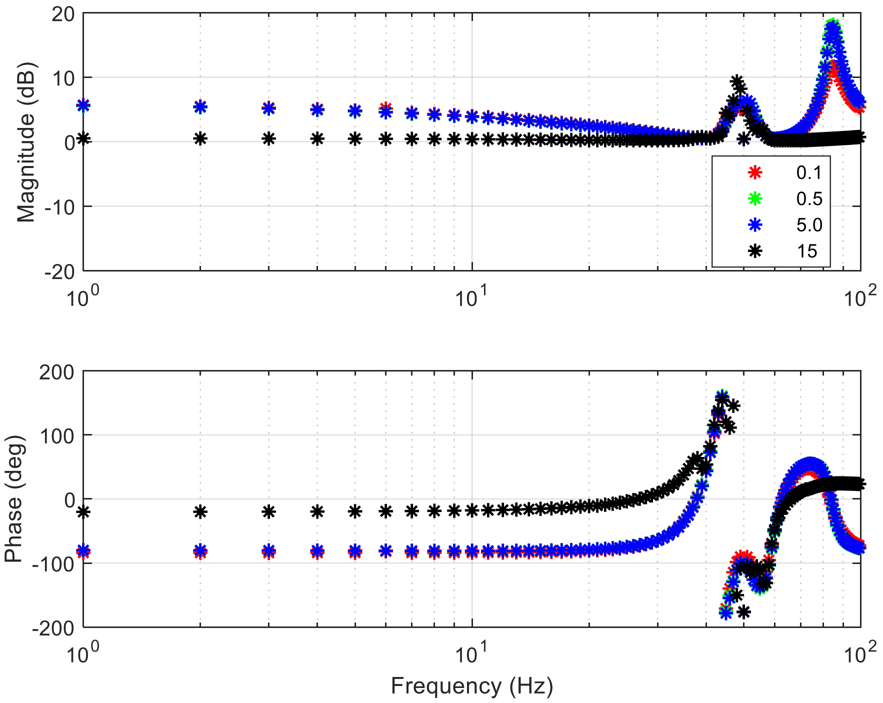

Figure 2.7 Impedance under different injection amplitude

According to the results in Figure 2.7, the impedance data is stable when the amplitude of the harmonic injection is within 5%. When the amplitude increases to 15%, the curve shape is significantly different from previous cases. Hence, a preliminary conclusion can be reached that the proper amplitude of the harmonic is required for obtaining the measurement impedance.

2.4.3 Reasonable resolution

When the frequency range is set up, the harmonic resolution becomes a key to determining the efforts that should be paid to the whole multi-run simulation. In this section, 0.5 Hz, 1 Hz and 2 Hz resolutions are implemented in Figure 2.8 to obtain a deeper understanding of the reasonable resolution for practical cases.

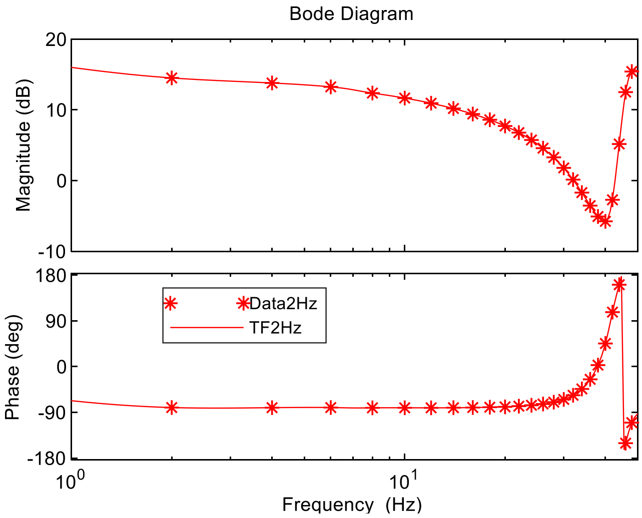

(a)

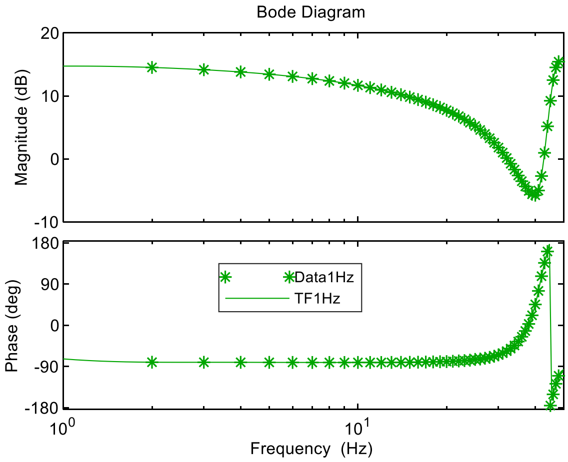

(b)

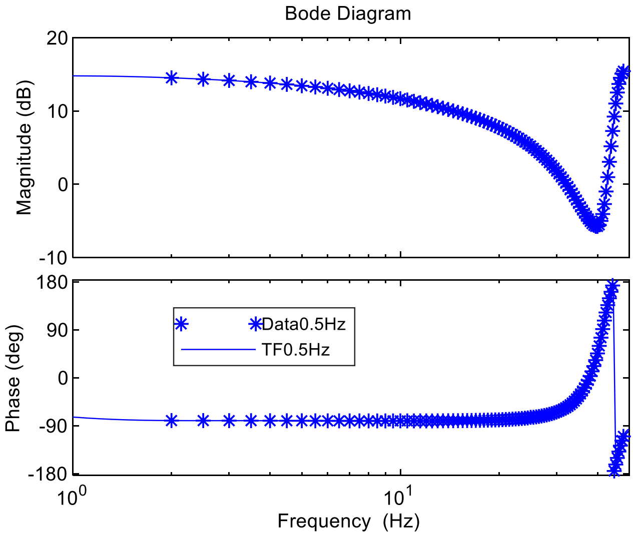

(c)

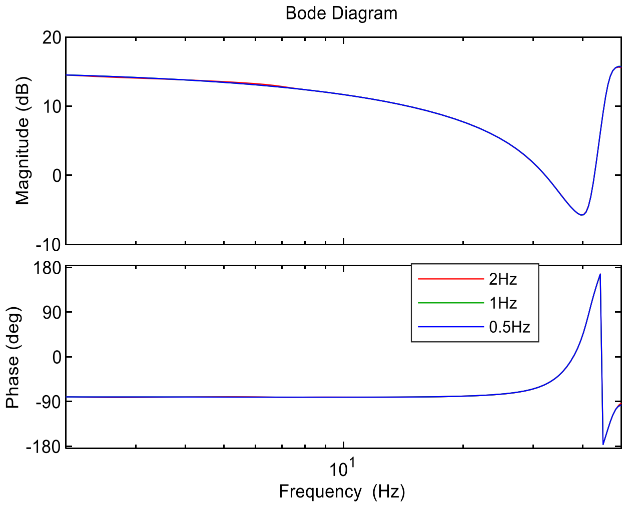

(d)

Figure 2.8 Estimated transfer function with different resolutions (a) 2Hz; (b) 1Hz; (c) 0.5Hz; (d) Combined

Mean squared error (MSE) [104] is widely utilized to evaluate the similarity between the data. It is defined as:

$$MSE = \frac{1}{N}\sum_{t=1}^{N} e^T(t)e(t) \tag{2.6}$$

where *e*(t) is the individual error between the calculated and the estimated data. N is the sample number.

Table 2.2 Impedance measurements with different resolution

Resolutions	0.5 Hz (reference)	1 Hz	2 Hz
Data Amount	97	49	25
Simulation Time	1 Day	2 Hours	50 Minutes
MSE	9.217e-06	1.264e-05	1.046e-05
Eigenvalue (frequency)	46.3114	46.3058	46.3277
Error (%)	0	0.0120	0.0351

From Table 2.2, the 1 Hz scanning resolution is accurate enough to do the impedance scanning. To analyse oscillations at a known frequency, it is reasonable to perform impedance sweeps with increased resolution near that frequency to obtain a more accurate impedance model.

2.5 Validation

2.5.1 Simulation model

In this section, the harmonic injection module and measurements module are presented. The function for each component is introduced and the parameter settings are explained.

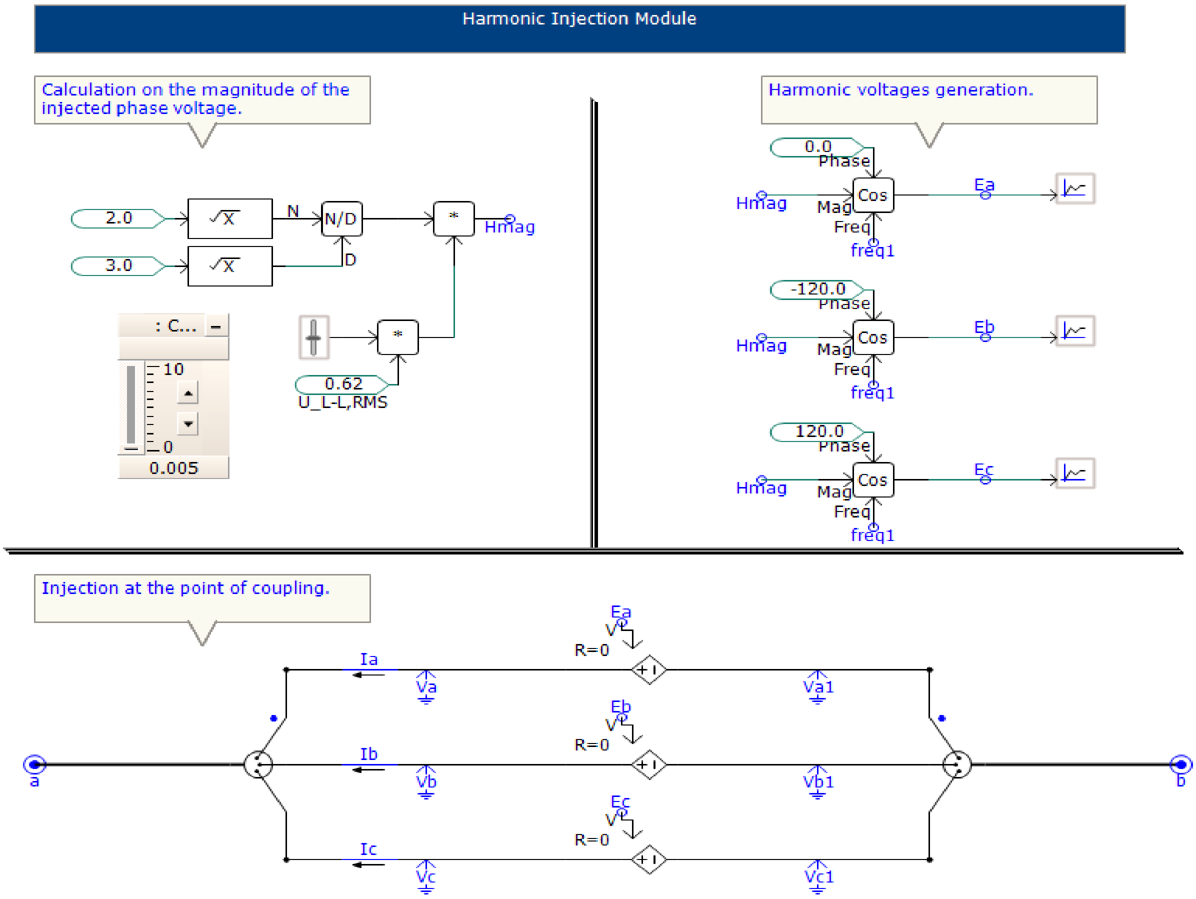

Figure 2.9 Harmonic injection and measurements module.

Figure 2.9 introduces the process of how to generate the amplitude and phase of the three-phase harmonic signal and measure the voltage and current at the connection point. When describing the voltage level of a system, the RMS value of the line voltage is often used. $\boldsymbol{H}_{\mathrm{mag}}$ represents the amplitude of the phase voltage, and the conversion process between it and the effective value of the line voltage is given. The phases of the three-phase harmonic voltages differ by 120 degrees in sequence. One end of the harmonic injection and measurement module is connected to the inverter and the other end is connected to the system.

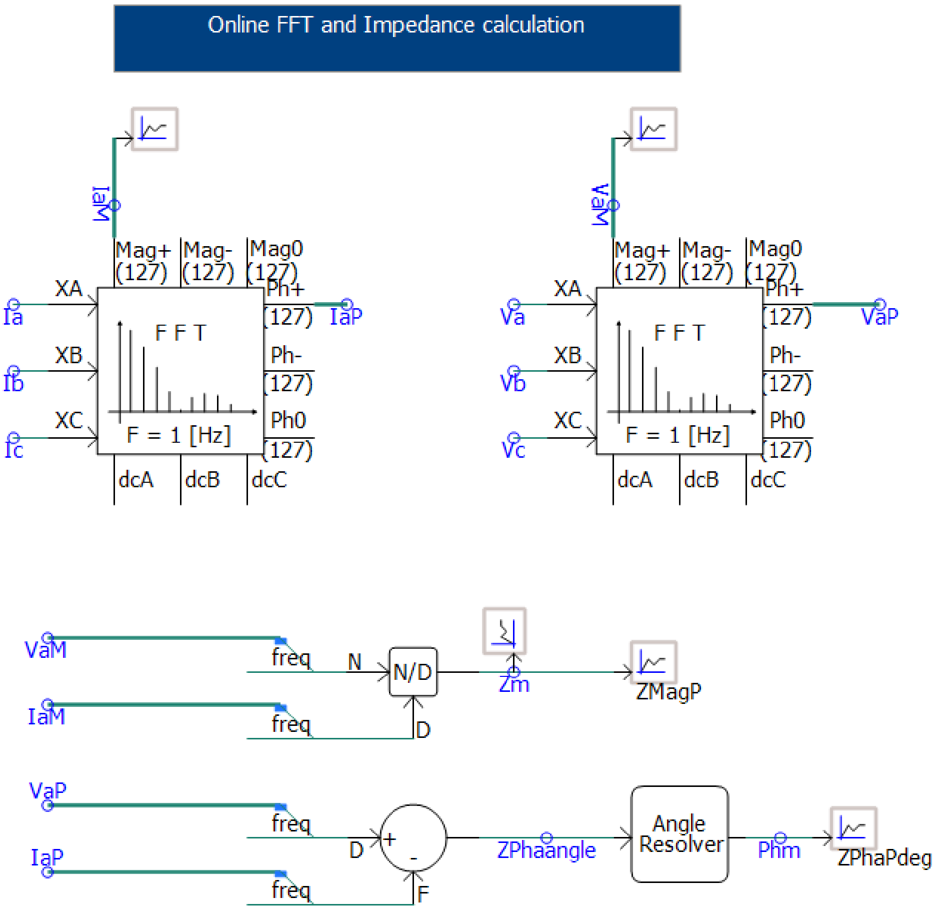

Figure 2.10 FFT and impedance calculation module.

Figure 2.10 describes the FFT and impedance calculation in PSCAD. The three-phase voltage and current are obtained from the measurement module and then imported to the FFT module to obtain the magnitude and phase angle. In the FFT module, the frequency of the fundamental wave is 1Hz and a total of 127 th harmonics are obtained after decomposition. The voltage and current of the specific order of harmonic are extracted and the amplitude and phase angle data of the impedance at a specific frequency are calculated.

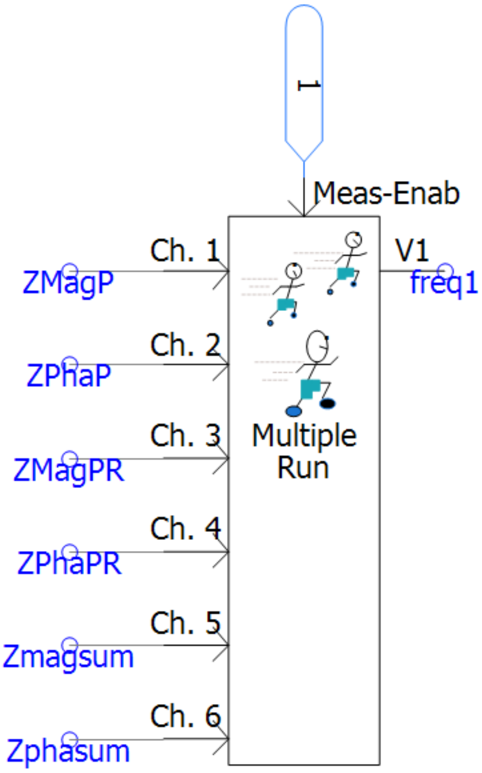

Figure 2.11 Data collection and multiple run module.

Figure 2.11 describes the multiple-run module and the data collected in the .out file. The multiple run module enables the automation to run PSCAD with varying harmonic frequency which is set from 1 Hz to 100 Hz with 1 Hz increment for each run. The recorded data for this component include the impedance magnitude and phase angle.

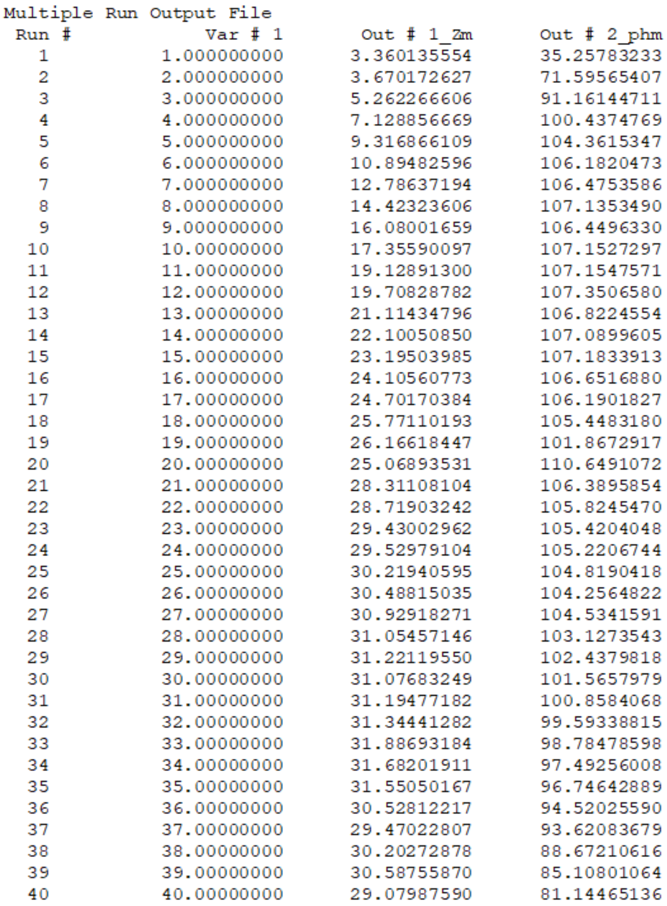

```
Multiple Run Output File
 Run #           Var # 1        Out # 1_Zm      Out # 2_phm
   1         1.000000000       3.360135554      35.25783233
   2         2.000000000       3.670172627      71.59565407
   3         3.000000000       5.262266606      91.16144711
   4         4.000000000       7.128856669      100.4374769
   5         5.000000000       9.316866109      104.3615347
   6         6.000000000       10.89482596      106.1820473
   7         7.000000000       12.78637194      106.4753586
   8         8.000000000       14.42323606      107.1353490
   9         9.000000000       16.08001659      106.4496330
  10         10.00000000       17.35590097      107.1527297
  11         11.00000000       19.12891300      107.1547571
  12         12.00000000       19.70828782      107.3506580
  13         13.00000000       21.11434796      106.8224554
  14         14.00000000       22.10050850      107.0899605
  15         15.00000000       23.19503985      107.1833913
  16         16.00000000       24.10560773      106.6516880
  17         17.00000000       24.70170384      106.1901827
  18         18.00000000       25.77110193      105.4483180
  19         19.00000000       26.16618447      101.8672917
  20         20.00000000       25.06893531      110.6491072
  21         21.00000000       28.31108104      106.3895854
  22         22.00000000       28.71903242      105.8245470
  23         23.00000000       29.43002962      105.4204048
  24         24.00000000       29.52979104      105.2206744
  25         25.00000000       30.21940595      104.8190418
  26         26.00000000       30.48815035      104.2564822
  27         27.00000000       30.92918271      104.5341591
  28         28.00000000       31.05457146      103.1273543
  29         29.00000000       31.22119550      102.4379818
  30         30.00000000       31.07683249      101.5657979
  31         31.00000000       31.19477182      100.8584068
  32         32.00000000       31.34441282      99.59338815
  33         33.00000000       31.88693184      98.78478598
  34         34.00000000       31.68201911      97.49256008
  35         35.00000000       31.55050167      96.74642889
  36         36.00000000       30.52812217      94.52025590
  37         37.00000000       29.47022807      93.62083679
  38         38.00000000       30.20272878      88.67210616
  39         39.00000000       30.58755870      85.10801064
  40         40.00000000       29.07987590      81.14465136
```

Figure 2.12 The impedance data in the PSCAD out file

Figure 2.12 shows the results of the simulation with multiple run modules. The first column of data represents the number of runs, the second column of data is the harmonic frequency under this operation, the third column of data is the amplitude of the system under test at this frequency, and the fourth column of data is the phase angle of the system under test at this frequency. Further stability analysis can be implemented with the output impedance data.

2.5.2 Results and discussions

The code and simulation model are developed for validation. The parameters for the inverter are provided in Appendix B.

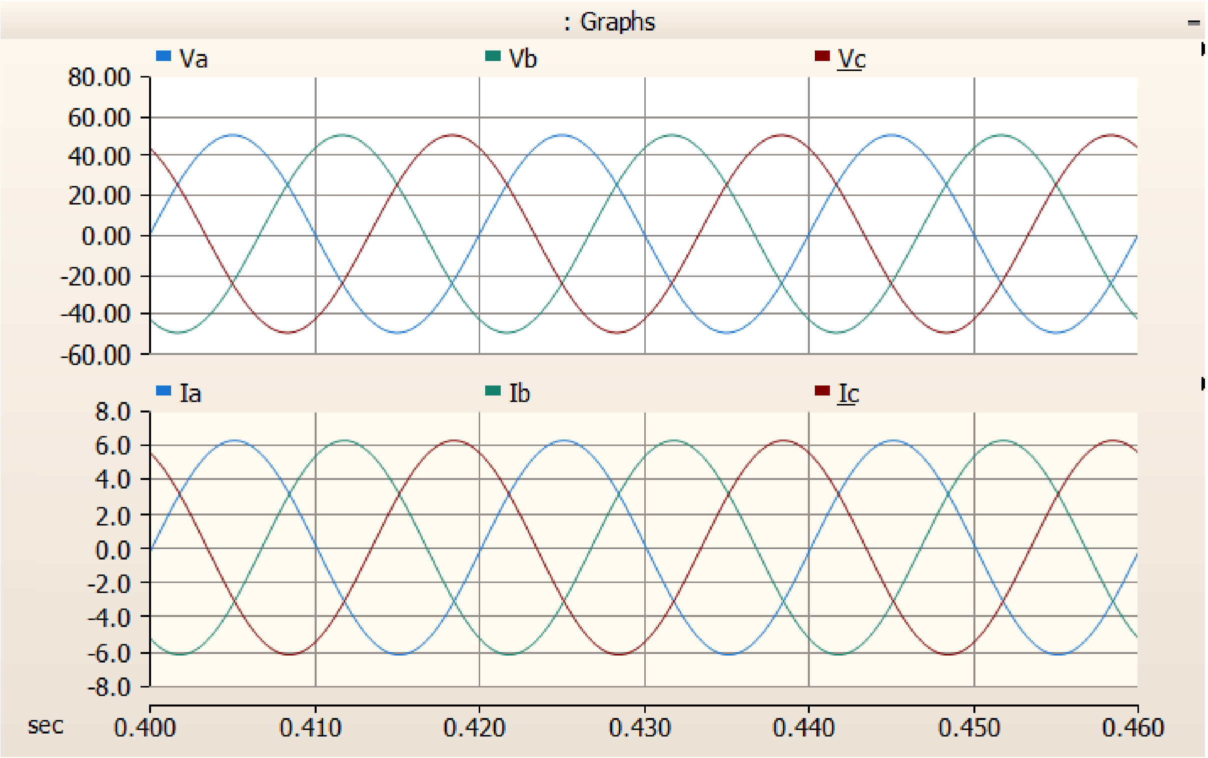

Figure 2.13 The output voltage and current of the inverter

Figure 2.13 shows the output current and voltage waves when the impedance scanning module is connected. The connection of a harmonic injection module should not change the operating point of the system.

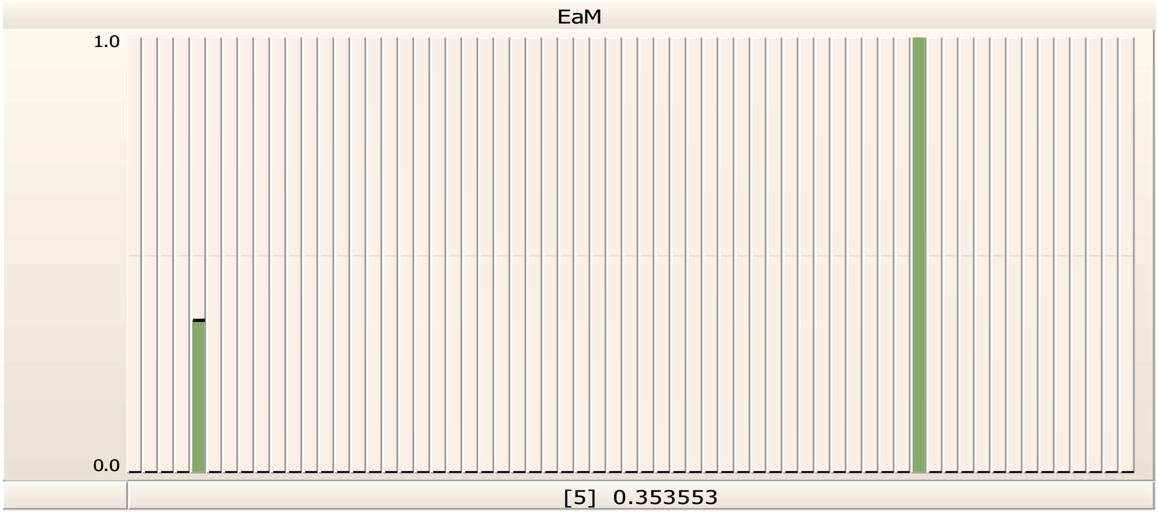

Figure 2.14 Positive sequence harmonic voltage with FFT

Figure 2.14 shows the amplitude of the voltage injection which is 1 % of the system rating voltage. A single harmonic injection method is used, and the system operates multiple times. When the fifth operation is performed, the injected harmonic frequency is 5 Hz.

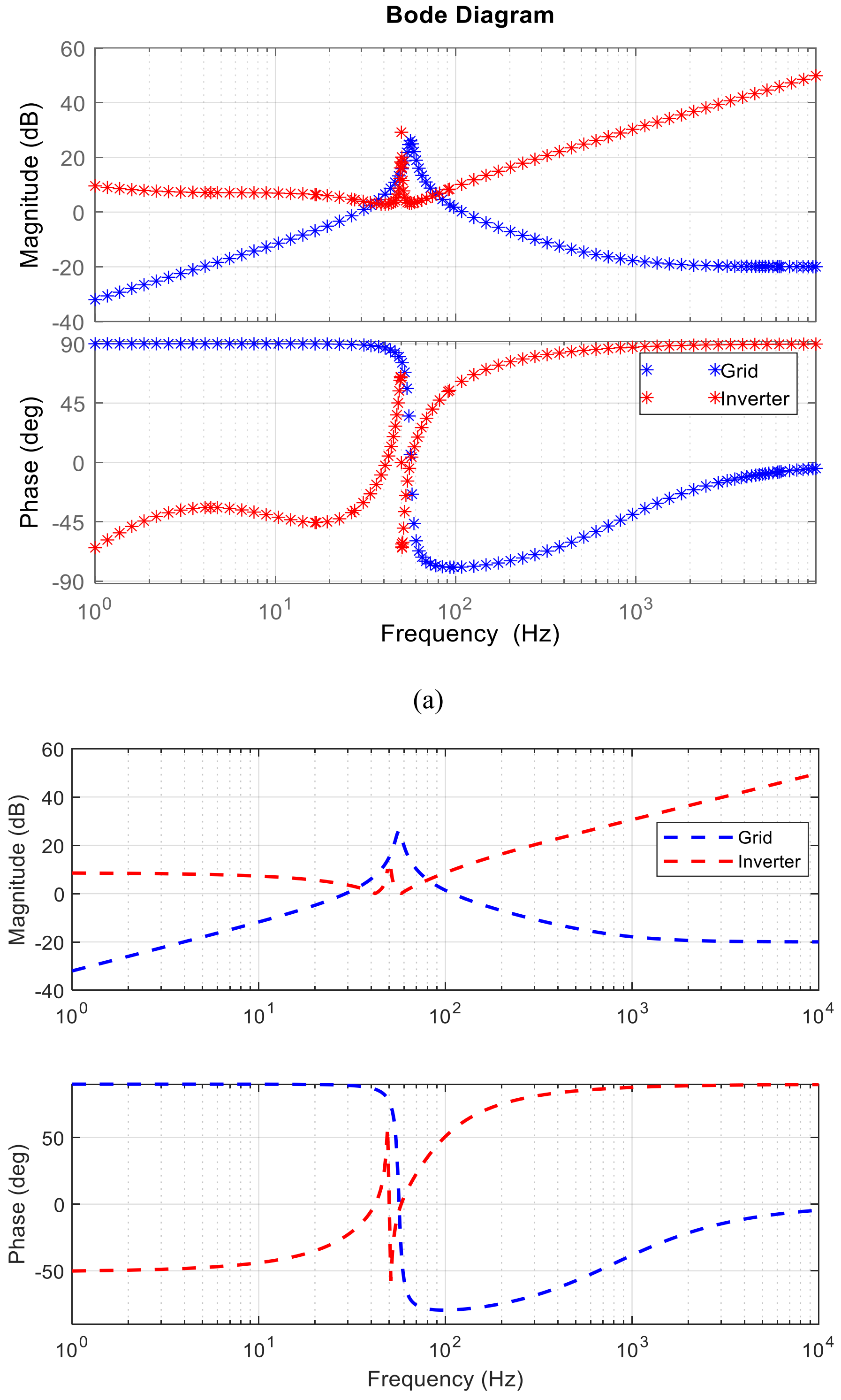

(a)

(b)

Figure 2.15 The VSC impedance (a) measurements model (b) state space model

Figure 2.15 shows the results from the analytical model and the measurements model. The similarity between the two models was analysed with a quantitative assessment using the model fitting index.

Akaike's final prediction error (FPE) [105] is defined as:

$$\text{FPE} = \det\left(\frac{1}{N} E^T E\right)\left(\frac{1+\frac{np}{N}}{1-\frac{np}{N}}\right) \tag{2.7}$$

where n_p is the number of free parameters in the model. np includes the number of estimated initial states. N is the number of samples in the estimation dataset. E is the N-by-n_y matrix of prediction errors, where n_y is the number of output channels.

Table 2.3 Evaluation model quality

Model evaluation	Grid impedance	Inverter impedance
MSE	2.956e-23	0.01152
FPE	2.966e-23	0.01156

According to Table 2.3, both inverter and grid impedance show a small value in MSE and FPE. Therefore, the measurement-based impedance model can represent the characteristics of the inverter when the detailed inverter model is unknown.

2.6 Summary

In Chapter 2, the impedance modelling method has been introduced and implemented with validation. Systematic guidance has been provided for the amplitude of the injected signal and the resolution of the impedance scanning. According to the results, the impedance data is stable when the amplitude of the harmonic injection is within 5%. When the amplitude increases to 15%, the curve shape is significantly different from previous cases. Hence, a proper amplitude of the harmonic voltage injection of less than 5% is required to obtain the measurement impedance. From the numerical comparisons between 0.5-Hz, 1-Hz and 2-Hz impedance scanning resolutions, the 1-Hz impedance scanning resolution is accurate enough to carry out the impedance modelling.

The impedance measurements data match well with the mathematical modelling results. The next step is to use these impedance data to analysis the system stability. This methodology is named as impedance-based stability analysis and will be introduced in chapter 3.

3. Impedance-based stability analysis

3.1 Introduction

Frequency scanning requires injecting a small signal into a time domain simulation of the system over a range of frequencies at steady state which is time intensive, especially for multiple inverters, detailed models at different operating points. Therefore, a preliminary screening method would be useful to ascertain the likelihood of interaction between power electronics equipment in transmission system operator (TSO) level network. The Multi infeed interaction factor (MIIF) [106]-[107] index is used for screening a large network to quantify potential risks between inverters. If a risk is identified, then secondly a full-scale analysis is automated using an automation tool as a scripting tool. Figure 3.1 describes the overview of the two-step method.

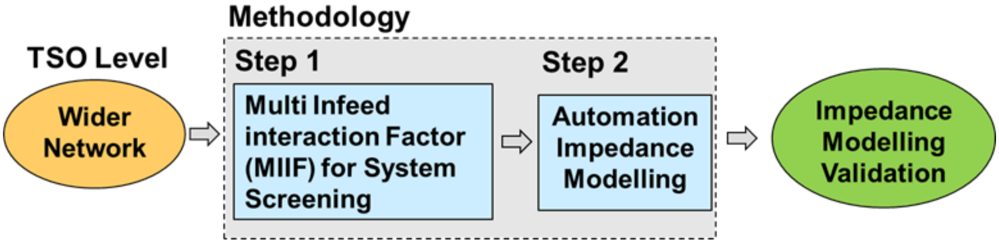

Figure 3.1 A two-step screening method

This Chapter covers the systematic procedure of identifying the potential oscillation in the network. The multi-infeed impact factor is presented, which is the simple and fast index to evaluate the control interaction in Section 3.2. The system strength is described using the short circuit ratio and its modified index in Section 3.3. The impedance-based stability theory is presented in Section 3.4. Case studies are given in Section 3.5.

3. 2 Multi-infeed impact factor

With an increasing number of IBRs, it was essential to develop a methodology to screen the likelihood of interactions between IBRs and to prioritise using the frequency scan toolbox where there is more risk of a control interaction. The MIIF requires only one voltage change and one measurement because it is only at fundamental frequency compared to many perturbations over an extensive range of frequencies. It is, therefore, a proper screening method before spending a lot of effort digging out more information. It looks simply at the coupling in terms of the electrical distance between inverters and the power rating of the IBRs.

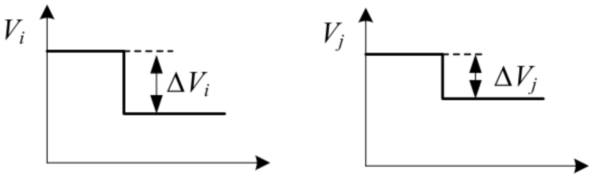

Figure 3.2 Voltage perturbation at bus ***i*** and voltage change measurements at bus ***j***

$$MIIF_{j,i} = \frac{\Delta V_i}{\Delta V_j} \tag{3.1}$$

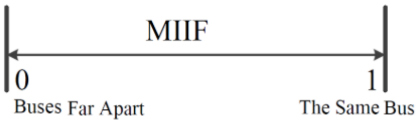

Figure 3.3 The range of MIIF and information

Figure 3.2 describes the voltage injection at bus ***i*** and the measurements of voltage change at bus ***j***. In Figure 3.3, the MIIF is a number between 1 and 0 describing the electrical distance via the voltage coupling between two IBRs. With 1 being at the same inverter bus and 0 being infinitely apart.

3. 3 SCR and system strength

The oscillation normally happens when a system is relatively weak. If the grid following inverter could operate normally in the weak grid, then it should be stable as well in the strong grid. Therefore, the system test is performed under a weak grid in most cases.

A weak grid is commonly defined as a power grid with a low short-circuit ratio (SCR). A weak grid can be obtained by increasing the impedance of the system and the target is to find the boundaries of stability. SCR could be used to identify whether the system is strong or not. The SCR of a synchronous generator is defined in IEC34-4 [108] as “The ratio of the field current for rated armature voltage on open–circuit to the field current for rated armature current on sustained symmetrical short circuit, both with the machine running at rated speed”. It is also defined as the short circuit capacity contributed from the network divided by the rated power of the converter interfaced device:

$$SCR = \frac{S_{ac}}{P_{dc}} = \frac{SCL}{P_{dc}} = \frac{1}{P_{dc}} * \frac{U^2}{Z_{eq}} \tag{3.2}$$

Table 3.1 Parameter definition and description of SCR

Symbol	Definition
$S_{ac} = SCL$	The short-circuit capacity of the system;
P_{dc}	The rated power of the converter interfaced device;
U	The rated voltage of the bus;
Z_{eq}	The equivalent impedance of the AC system.

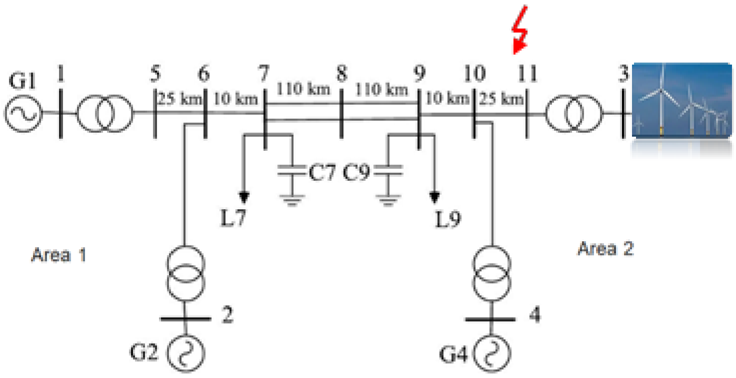

Figure 3.4 Modified Kundur’s two-area Test benchmark [109]

$$SCR = \frac{S_{ac1}}{P_{WF4}} = \frac{\sqrt{3} * 400kV * 4.30kA}{700MW} = 4.25 \tag{3.3}$$

Table 3.2 System stability under different lengths of transmission line

Length (km)	25	50	75	100	125	150	175	200

Fault current (kA)	4.30	3.85	3.39	3.04	2.63	2.32	2.26	1.86
SCR	4.25	3.81	3.36	3.01	2.60	2.30	2.24	1.84
Stability (Y/N)	Y	Y	Y	Y	Y	Y	Y	N

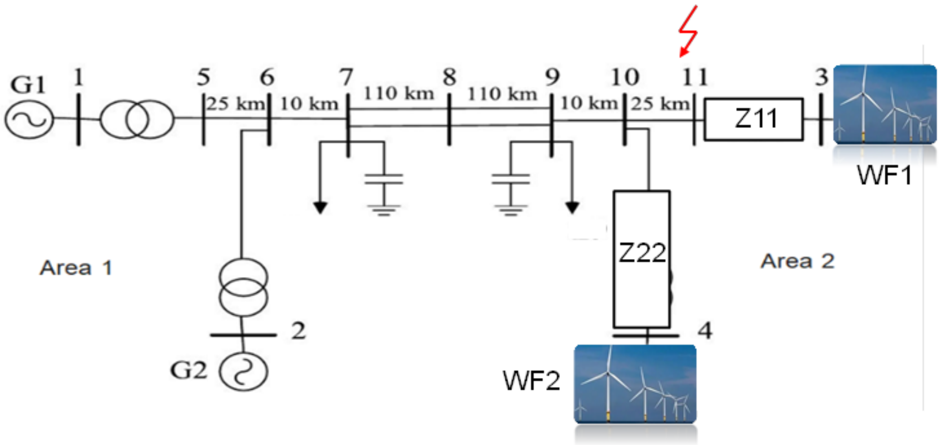

Case: G1, G2 - SGs; G3 - WF1, G4 - WF2
Z11, Z22 – Impedance of line and transformer

Figure 3.5 Benchmark test system with fault at bus 11

Assessing the potential for interaction of the multiple HVDC links connecting to the same region in a network. The objectives are to assess:

(1) Impact of adjacent existing WFs on the performance of the proposed WF as seen at its connection point.

(2) The impact of the new WF affected the adjacent existing WFs as seen at their connection points.

This method allows the calculation of the SCR at the WF connection point, medium voltage collection grid, and wind turbine terminals.

$$ESCR_i = \frac{S_i}{P_{WFi}+\sum_j(WFIF_{ji}*P_{WFj})} \tag{3.4}$$

Wind Farm Interaction Factor (WFIF) is defined as follows:

$$WFIF_{ij} = \frac{\Delta V_i}{\Delta V_j} \tag{3.5}$$

where ΔV_i is the voltage change observed on the bus ***i*** for a small voltage change ΔV_j at bus *j*.

If WF is far apart from the injection point which will have a low WFIF, whereas, for nearby buses, WFIF should be closer to unity.

$$WFIF_{ij} \in (0,1] \tag{3.6}$$

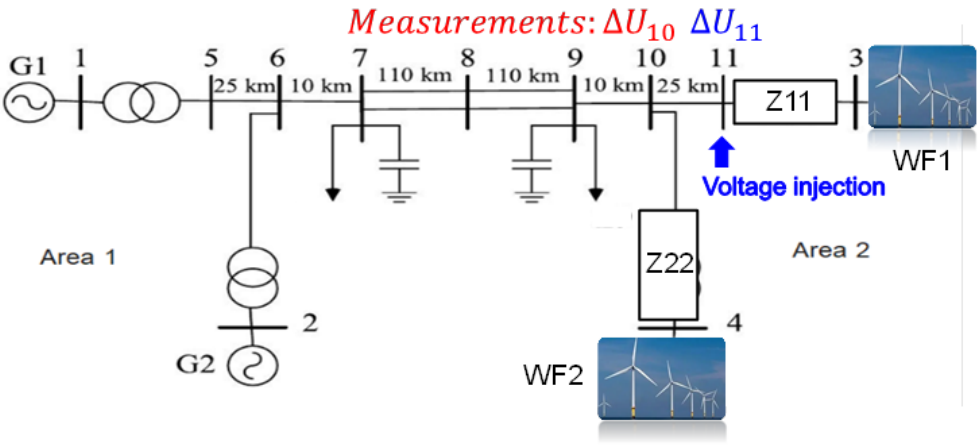

Case: G1, G2 - SGs; G3 - WF1, G4 - WF2
Z11, Z22 – Impedance of line and transformer

Figure 3.6 The schematic diagram of measuring MIIF

The ESCR could be calculated using the measurement data. The ESCR for WF1 and WF2 are obtained with modified two area four machine benchmarks.

$$ESCR_{WF\mathbf{1}} = \frac{\sqrt{3}*400kV*2.5kA}{700MW+0.72*700MW} = 1.43 \tag{3.7}$$

$$ESCR_{WF\mathbf{2}} = \frac{\sqrt{3}*400kV*2.5kA}{700MW+0.67*700MW} = 1.48 \tag{3.8}$$

Meanwhile, the critical case is set up by increasing the distance between Bus 11 and Bus 10.

$$ESCR_{WF\mathbf{1}} = \frac{\sqrt{3}*400kV*2.5kA}{700MW+\mathbf{0.29}*700MW} = 1.91 \tag{3.9}$$

$$ESCR_{WF\mathbf{2}} = \frac{\sqrt{3}*400kV*2.5kA}{700MW+\mathbf{0.25}*700MW} = 1.97 \tag{3.10}$$

It can be concluded that when two buses are close, the ESCR of the wind farm increase cause the coupling effect is not strong.

Table 3.3 ESCR values under the different distances between bus 10 and 11

Objectives	P_{dc}	CSCR	Original distance: 25km			Critical distance: 150km		
			WFIF	ESCR	Difference (%)	WFIF	ESCR	Difference (%)
WF1	700	1.23	0.72	1.43	16.26	0.29	1.91	55.28
WF2	700	1.23	0.67	1.48	20.32	0.25	1.97	60.16

3. 4 Principle of stability analysis

The wider network can be represented with a voltage source in series with a grid impedance. The character of the inverter is similar to a current source in parallel with an output impedance. Hence, the whole interconnected system is shown in Figure 3.7. The assumption includes that the grid can be assumed to be stable without the inverter, and the inverter to be stable when the grid impedance is zero.

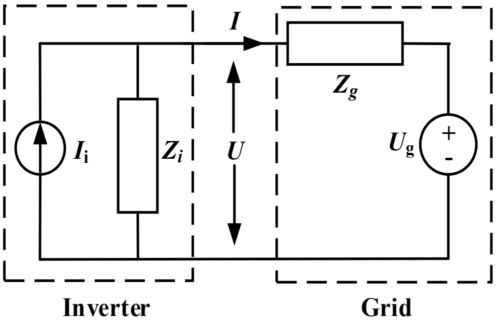

Figure 3.7 The partitioned interconnected system

$$I(s) = \frac{I_c(s)Z_0(s)}{Z_0(s)+Z_g(s)} - \frac{V_g(s)}{Z_0(s)+Z_g(s)} \tag{3.11}$$

$$I(s) = [I_i(s) - \frac{V_g(s)}{Z_0(s)}] \cdot \frac{1}{1+Z_g(s)/Z_i(s)} \tag{3.12}$$

$$U(s) = \left[Z_g(s)I_i(s) + U_g(s)\right]\frac{1}{1+Z_g(s)/Z_i(s)} \tag{3.13}$$

$$L(s) = Z_g(s)/Z_0(s) \tag{3.14}$$

The Nyquist criterion can evaluate if the network is stable or not. When L(s) satisfy the Nyquist criterion, the system is stable. However, the revealed information from Nyquist is limited and sometimes it is not clear from the plot. The stability of the interconnected system can also be determined with a close-loop transfer function. Besides, the real part of the eigenvalues of the close loop transfer function is always negative, so the system is stable.

$$H(s) = \frac{1}{1+Z_g(s)/Z_0(s)} \tag{3.15}$$

$$H(s)\ is\ stable \rightarrow \forall real(\lambda) < 0 \tag{3.16}$$

The information provided by eigenvalue includes the damping and frequency of the oscillation. The individual eigenvalue is dependent on all parameters and some of them may be the main factors.

3. 5 Validation

The time domain data from the EMT simulation is processed using FFT to capture the frequency. The estimated oscillation modes using Eigenvalues loci from the impedance model are 45.3Hz and 54.6Hz. As the grid impedance increases, the eigenvalues move towards the right direction which indicates the potential instability issue. The oscillation modes identified by FFT based on EMT simulation are 46.0Hz and 54.0Hz. As the error between prediction and experiment is within 1 Hz (2% tolerance when the reference is 50 Hz), the impedance modelling based on the measurement is acceptable for further stability analysis.

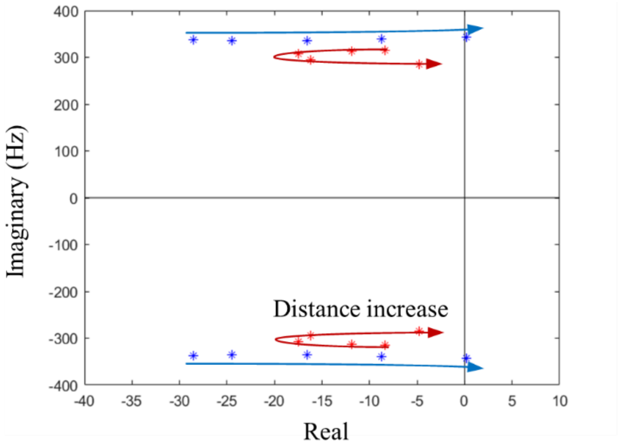

(a) eigenvalue

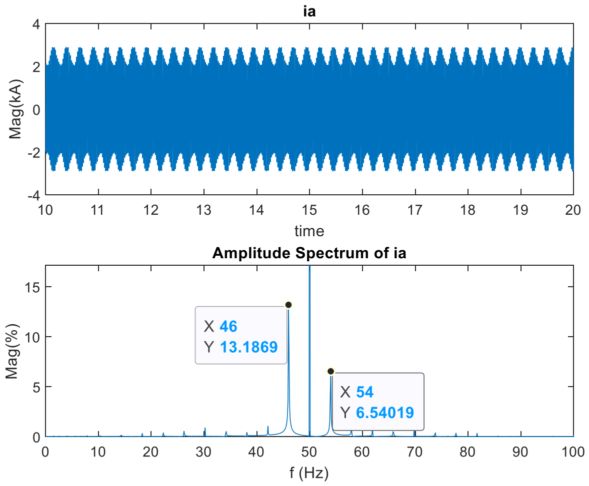

(b) Current curve and its FFT results

Figure 3.8 Validation with frequency domain results and time domain results

3. 6 Summary

This Chapter systematically evaluates the stability of interconnected systems. The detailed conclusions are summarized as follows:

(1) First, the perturbation is imposed at a specific location according to MIIF, and the response in the network is observed to obtain relevant information about weak locations.

(2) The two indicators of grid short-circuit ratio and grid strength are further explored to explain the stability of the network.

(3) Finally, the conditions and principles for determining stability are introduced, and the Fourier transform is performed on the waveform of the above unstable phenomenon. The validity of the stability theory is further proved by comparing the mathematically derived oscillation frequencies with the imaginary parts of the eigenvalues estimated from the impedance model.

4. Impedance reshaping methods for white-box model

4.1 Introduction

Impedance reshaping methods refer to techniques employed to modify and optimize the impedance characteristics of electrical circuits or systems. These methods are widely adopted in various fields, including signal processing, telecommunications, and power systems. The primary goal of impedance reshaping is to tailor the impedance profile to meet specific requirements, improving the performance or functionality of the system. This can involve adjusting the magnitude and phase angle in a specific range of frequency, mitigating reflections, or matching impedances for efficient power transfer. Techniques such as impedance-matching networks, filters, and reactive components are commonly used in impedance reshaping. By strategically designing and implementing these methods, engineers can enhance the overall efficiency, signal integrity, and reliability of electronic systems, contributing to advancements in diverse fields of technology.

For a conventional inverter, the maximum output power is limited and will lose stability when it exceeds a specific range. The negative resistance characteristic caused by PLL serves as the main factor causing system instability. There are two main methods to increase the maximum values of the output power. One is to reduce the PLL bandwidth or outer loop bandwidth, but the cost is to influence the dynamic character of the system. This Chapter develops a novel control topology-based impedance weighting method to mitigate this problem. The proposed method can effectively expand the stable operating range of the inverter. First, the state space model is built in Section 4.2. Then the impedance-based analysis is provided in Section 4.3. Further verification of the proposed strategy is implemented via simulation in Section 4.4.

4.2 State space model

The control system includes a PLL, an inner current loop, an active power outer loop, and an AC voltage amplitude outer loop. The PLL is to lock the phase and frequency of the three-phase AC voltage composite vector Vo at the PCC point to provide a rotation angle for coordinate transformation. The function of the current loop is to enable the inverter output current to follow the given value. The deviation of the outer loop power and voltage determines the given value of the current inner loop. Finally, the inverter's output voltage is controlled by changing the modulation wave.

The circuit differential equation in the three-phase coordinate system is:

$$\begin{cases} L_g \frac{di_{oa}}{dt} = v_{oa} - v_{ga} - R_g \cdot i_{oa} \\ L_g \frac{di_{ob}}{dt} = v_{ob} - v_{gb} - R_g \cdot i_{ob} \\ L_g \frac{di_{oc}}{dt} = v_{oc} - v_{gc} - R_g \cdot i_{oc} \end{cases} \tag{4.1}$$

$$\begin{cases} C_f \frac{dv_{oa}}{dt} = i_{oa} - i_{ga} \\ C_f \frac{dv_{ob}}{dt} = i_{ob} - i_{gb} \\ C_f \frac{dv_{oc}}{dt} = i_{oc} - i_{gc} \end{cases} \tag{4.2}$$

$$\begin{cases} L_f \frac{di_{ca}}{dt} = v_{ca} - v_{oa} - R_f \cdot i_{ca} \\ L_f \frac{di_{cb}}{dt} = v_{cb} - v_{ob} - R_f \cdot i_{cb} \\ L_f \frac{di_{cc}}{dt} = v_{cc} - v_{oc} - R_f \cdot i_{cc} \end{cases} \tag{4.3}$$

Perform Park transformation on equations (4.1) - (4.3):

$$T_{3s-2r} \begin{bmatrix} \dot{X}_a \\ \dot{X}_b \\ \dot{X}_c \end{bmatrix} = \begin{bmatrix} \dot{X}_d - \omega X_q \\ \dot{X}_q + \omega X_d \end{bmatrix} \tag{4.4}$$

The circuit differential equation in the dq coordinate system is:

$$\begin{cases} v_{od} - v_{gd} = L_g \frac{di_{od}}{dt} + R_g i_{od} - \omega L_g i_{oq} \\ v_{oq} - v_{gq} = L_g \frac{di_{oq}}{dt} + R_g i_{oq} + \omega L_g i_{od} \end{cases} \tag{4.5}$$

$$\begin{cases} i_{cd} - i_{od} = C_f \frac{dv_{od}}{dt} - \omega C_f v_{oq} \\ i_{cq} - i_{oq} = C_f \frac{dv_{oq}}{dt} + \omega C_f v_{od} \end{cases} \tag{4.6}$$

$$\begin{cases} v_{cd} - v_{od} = L_f \frac{di_{cd}}{dt} + R_f i_{cd} - \omega L_f i_{cq} \\ v_{cq} - v_{oq} = L_f \frac{di_{cq}}{dt} + R_f i_{cq} + \omega L_f i_{cd} \end{cases} \tag{4.7}$$

The linearized small signal equation is the same as above except that all the variables are replaced by their incremental changes of the variables.

The linearized small signal equation for the coordinate transformation is:

$$\begin{cases} \Delta v_{od}^{ctrl} = \Delta v_{od} + v_{oq0} \cdot \Delta\theta_{pll} \\ \Delta v_{oq}^{ctrl} = \Delta v_{oq} - v_{od0} \cdot \Delta\theta_{pll} \end{cases} \tag{4.8}$$

$$\begin{cases} \Delta i_{cd}^{ctrl} = \Delta i_{cd} + i_{cq0} \cdot \Delta\theta_{pll} \\ \Delta i_{cq}^{ctrl} = \Delta i_{cq} - i_{cd0} \cdot \Delta\theta_{pll} \end{cases} \tag{4.9}$$

$$\begin{cases} \Delta v_{cd} = \Delta v_{cd}^{ctrl} - v_{cq0} \cdot \Delta\theta_{pll} \\ \Delta v_{cq} = \Delta v_{cq}^{ctrl} + v_{cd0} \cdot \Delta\theta_{pll} \end{cases} \tag{4.10}$$

Differential equations for PLL:

$$\begin{cases} \frac{dInt_{pll}}{dt} = \frac{v_{oq}^{ctrl}}{V_o^*} \\ \frac{d\theta_{pll}}{dt} = \omega_{pll} = K_{p\_pll} \cdot \frac{v_{oq}^{ctrl}}{V_o^*} + K_{i\_pll} \cdot Int_{pll} + \omega_N \end{cases} \tag{4.11}$$

where Int_{pll} represents the state variable of the integrator.

Linearized small-signal equations for PLLs:

$$\begin{cases} \frac{d\Delta Int_{pll}}{dt} = \frac{\Delta v_{oq}^{ctrl}}{V_o^*} \\ \frac{d\Delta\theta_{pll}}{dt} = \Delta\omega_{pll} = K_{p\_pll} \cdot \frac{\Delta v_{oq}^{ctrl}}{V_o^*} + K_{i\_pll} \cdot \Delta Int_{pll} \end{cases} \tag{4.12}$$

Differential equations for current inner loop control

$$\begin{cases} \frac{dInt_{id}}{dt} = {i_{cd}}^* - {i_{cd}}^{ctrl} \\ {v_{cd}}^* = K_{p\_id}\left({i_{cd}}^* - {i_{cd}}^{ctrl}\right) + K_{i\_id} \cdot Int_{id} - \omega_N L_f {i_{cq}}^{ctrl} + V_o^* \end{cases} \tag{4.13}$$

$$\begin{cases} \frac{dInt_{iq}}{dt} = {i_{cq}}^* - {i_{cq}}^{ctrl} \\ {v_{cq}}^* = K_{p\_iq}\left({i_{cq}}^* - {i_{cq}}^{ctrl}\right) + K_{i\_id} \cdot Int_{iq} - \omega_N L_f {i_{cd}}^{ctrl} + 0 \end{cases} \tag{4.14}$$

where Int_{id} and Int_{iq} are variables of the integrator under current inner loop control.

When $\omega_N = \omega$, the linearized small signal equation of current inner loop control:

$$\begin{cases} \frac{d\Delta Int_{id}}{dt} = \Delta {i_{cd}}^* - \Delta {i_{cd}}^{ctrl} \\ \Delta {v_{cd}}^* = K_{p\_id}\left(\Delta {i_{cd}}^* - \Delta {i_{cd}}^{ctrl}\right) + K_{i\_id} \cdot \Delta Int_{id} - \omega L_f \Delta {i_{cq}}^{ctrl} \end{cases} \tag{4.15}$$

$$\begin{cases} \frac{d\Delta Int_{iq}}{dt} = \Delta {i_{cq}}^* - \Delta {i_{cq}}^{ctrl} \\ \Delta {v_{cq}}^* = K_{p\_iq}\left(\Delta {i_{cq}}^* - \Delta {i_{cq}}^{ctrl}\right) + K_{i\_id} \cdot \Delta Int_{iq} - \omega_N L_f \Delta {i_{cd}}^{ctrl} \end{cases} \tag{4.16}$$

Differential equations of power outer loop and voltage outer loop:

$$\begin{cases} \frac{dInt_P}{dt} = P^* - P_{LPF}^{ctrl} \\ i_{cd}^* = K_{p\_P}\left(P^* - {P_{LPF}}^{ctrl}\right) + K_{i\_P} \cdot Int_P \end{cases} \tag{4.17}$$

$$\begin{cases} \frac{dInt_V}{dt} = V_o^* - V_{oLPF}^{ctrl} \\ i_{cq}^* = K_{p\_V}(-1)\left(V_o^* - V_{oLPF}^{ctrl}\right) + K_{i\_V}(-1) \cdot Int_V \end{cases} \tag{4.18}$$

The linearized small signal equation is the same as above except that all the variables are replaced by their incremental changes of the variables.

Calculation formulas for active power and voltage amplitude:

$$\begin{cases} P^{ctrl} = \frac{3}{2}\left(v_{od}^{ctrl} \cdot i_{cd}^{ctrl} + v_{oq}^{ctrl} \cdot i_{cq}^{ctrl}\right) \\ V_o^{ctrl} = \sqrt{\left(v_{od}^{ctrl}\right)^2 + \left(v_{oq}^{ctrl}\right)^2} \end{cases} \tag{4.19}$$

In the stable state, v_{od}^{ctrl}=V_o， v_{oq}^{ctrl}=0. The linearized small signal equation i

$$\begin{cases} \Delta P^{ctrl} = \frac{3}{2}\left(i_{cd0}\Delta v_{od}^{ctrl} + i_{cq0}\Delta v_{oq}^{ctrl} + V_o \Delta i_{cd}{}^{ctrl}\right) \\ \Delta V_o^{ctrl} = \Delta v_{od}^{ctrl} \end{cases} \tag{4.20}$$

Differential equation for low pass filter:

$$\begin{cases} \frac{dP_{LPF}^{ctrl}}{dt} = \omega_{LPF} \cdot P^{ctrl} - \omega_{LPF} \cdot P_{LPF}^{ctrl} \\ \frac{dV_{oLPF}^{ctrl}}{dt} = \omega_{LPF} \cdot V_o^{ctrl} - \omega_{LPF} \cdot V_{oLPF}^{ctrl} \end{cases} \tag{4.21}$$

where ω_{LPF} represents cutoff frequency in the low-pass filter.

When $\Delta v_{gd} = 0$， $\Delta v_{gq} = 0$, then the state-space function can be achieved：

$$\Delta\dot{x}_{14\times1} = A_{14\times14} \cdot \Delta x_{14\times1} + B_{14\times2} \cdot \Delta u_{2\times1} \tag{4.22}$$

where $\Delta u_{2\times1} = [\Delta P^{*}, \Delta V_o^{*}]^T$

Normally ΔP^{*} and ΔV_o^{*} equals to zero, and eq (4.22) could be simplified as

$$\Delta\dot{x}_{14\times1} = A_{14\times14} \cdot \Delta x_{14\times1} \tag{4.23}$$

where $A_{14\times14}$ =

$$\begin{bmatrix}
\frac{-R_g}{L_g} & \omega & \frac{1}{L_g} & 0 & 0 & 0 & 0 & 0 & 0 & 0 & 0 & 0 & 0 & 0 \\
-\omega & \frac{-R_g}{L_g} & 0 & \frac{1}{L_g} & 0 & 0 & 0 & 0 & 0 & 0 & 0 & 0 & 0 & 0 \\
\frac{-1}{C_f} & 0 & 0 & \omega & \frac{1}{C_f} & 0 & 0 & 0 & 0 & 0 & 0 & 0 & 0 & 0 \\
0 & \frac{-1}{C_f} & -\omega & 0 & 0 & \frac{1}{C_f} & 0 & 0 & 0 & 0 & 0 & 0 & 0 & 0 \\
0 & 0 & \frac{-1}{L_f} & 0 & \frac{R_f + K_{p\_id}}{-L_f} & 0 & \frac{K_{p\_id}}{L_f} & 0 & \frac{K_{p\_id}K_{i\_P}}{L_f} & 0 & 0 & A_{12,5} & A_{13,5} & 0 \\
0 & 0 & 0 & \frac{-1}{L_f} & 0 & \frac{R_f + K_{p\_iq}}{-L_f} & 0 & \frac{K_{p\_iq}}{L_f} & 0 & \frac{K_{p\_iq}K_{i\_V}}{-L_f} & 0 & A_{12,6} & 0 & A_{14,6} \\
0 & 0 & 0 & 0 & -1 & 0 & 0 & 0 & K_{i\_P} & 0 & 0 & -i_{cq0} & -K_{p\_P} & 0 \\
0 & 0 & 0 & 0 & 0 & -1 & 0 & 0 & 0 & -K_{i\_V} & 0 & i_{cd0} & 0 & K_{p\_V} \\
0 & 0 & 0 & 0 & 0 & 0 & 0 & 0 & 0 & 0 & 0 & 0 & -1 & 0 \\
0 & 0 & 0 & 0 & 0 & 0 & 0 & 0 & 0 & 0 & 0 & 0 & 0 & -1 \\
0 & 0 & 0 & \frac{1}{V_o} & 0 & 0 & 0 & 0 & 0 & 0 & 0 & -1 & 0 & 0 \\
0 & 0 & 0 & \frac{K_{p\_pll}}{V_o} & 0 & 0 & 0 & 0 & 0 & 0 & K_{i\_pll} & -K_{p\_pll} & 0 & 0 \\
0 & 0 & \frac{3}{2}i_{od0} \cdot \omega_{LPF} & \frac{3}{2}i_{oq0} \cdot \omega_{LPF} & \frac{3}{2}v_{od0} \cdot \omega_{LPF} & 0 & 0 & 0 & 0 & 0 & 0 & 0 & -\omega_{LPF} & 0 \\
0 & 0 & \omega_{LPF} & 0 & 0 & 0 & 0 & 0 & 0 & 0 & 0 & 0 & 0 & -\omega_{LPF}
\end{bmatrix}$$

$$\Delta x_{14\times1} = [\Delta i_{od}, \Delta i_{oq}, \Delta v_{od}, \Delta v_{oq}, \Delta i_{cd}, \Delta i_{cq}, \Delta Int_{id}, \Delta Int_{iq}, \Delta Int_P, \Delta Int_V, \Delta Int_{pll}, \Delta\theta_{pll}, \Delta P_{LPF}^{ctrl}, \Delta V_{oLPF}^{ctrl}]^T$$

The eigenvalues of the matrix $A_{14\times 14}$ indicate whether the system is stable or not. The boundary of stable operation can be determined based on the location of the eigenvalues under multiple operating points.

4.3 Impedance model

The frequency domain impedance model is derived, then the transfer function of each module is:

$$\begin{cases} B_{Lg}=\begin{bmatrix} sL_g+R_g & -\omega L_g \\ \omega L_g & sL_g+R_g \end{bmatrix}, B_{Cf}=\begin{bmatrix} sC_f & -\omega C_f \\ \omega C_f & sC_f \end{bmatrix} \\ B_{Lf}=\begin{bmatrix} sL_f+R_f & -\omega L_f \\ \omega L_f & sL_f+R_f \end{bmatrix}, B_{decpl}=\begin{bmatrix} 0 & -\omega L_f \\ \omega L_f & 0 \end{bmatrix} \\ B_{PI-PV}=\begin{bmatrix} G_{pi\_P} & 0 \\ 0 & -G_{pi\_V} \end{bmatrix}, B_{PI-I}=\begin{bmatrix} G_{pi\_I} & 0 \\ 0 & G_{pi\_I} \end{bmatrix} \\ B_{LPF}=\begin{bmatrix} G_{LPF} & 0 \\ 0 & G_{LPF} \end{bmatrix}, B_{pll-Vc=}=\begin{bmatrix} 0 & -v_{cq0}/V_o\cdot G_{pll} \\ 0 & v_{cd0}/V_o\cdot G_{pll} \end{bmatrix} \\ B_v=\begin{bmatrix} 3/2\cdot V_o & 0 \\ 0 & 0 \end{bmatrix}, B_{pll-Ic}=\begin{bmatrix} 0 & -i_{cq0}/V_o\cdot G_{pll} \\ 0 & i_{cd0}/V_o\cdot G_{pll} \end{bmatrix} \\ B_i=\begin{bmatrix} 3/2\cdot i_{cd0} & 3/2\cdot i_{cq0} \\ 1 & 0 \end{bmatrix}, B_{pll-Vo}=\begin{bmatrix} 0 & 0 \\ 0 & G_{pll} \end{bmatrix} \end{cases} \tag{4.24}$$

$$\begin{cases} G_{pi\_P}=K_{p\_P}+\frac{K_{i\_P}}{s} \\ G_{pi\_V}=K_{p\_V}+\frac{K_{i\_V}}{s} \\ G_{pi\_I}=K_{p\_I}+\frac{K_{i\_I}}{s} \\ G_{\mathrm{LPF}}=\frac{\omega_{\mathrm{LPF}}}{s+\omega_{\mathrm{LPF}}} \\ G_{pll}=\frac{2\zeta\omega_n s+\omega_n^2}{s^2+2\zeta\omega_n s+\omega_n^2} \end{cases} \tag{4.25}$$

The control block can be described in Figure 4.1.

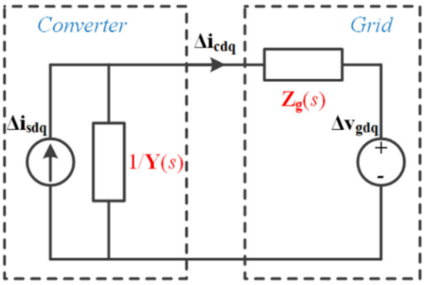

Figure 4.1 Norton-Thevenin small signal equivalent circuit

The linearized model of the grid-connected inverter is represented by the Norton-Thevenin equivalent. The entire network is separated from the inverter and the grid. The inverter can be equivalent to a current source connected in parallel with an admittance $Y(s)$, and the grid is represented as a voltage source connected and its impedance $Z_g(s)$.

$$Z_g(s) = \left(B_{Lg}^{-1} + B_{Cf}\right)^{-1} \approx B_{Lg} \tag{4.26}$$

$$Y(s) = \left[B_{Lf} + B_{PI-I} - B_{decpl} + B_{PI-I}B_{PI-PV}B_{LPF}B_V\right]^{-1} \cdot \left[I - \left(B_{PI-I} - B_{decpl} + B_{PI-I}B_{PI-PV}B_{LPF}B_v\right) \cdot B_{pll-Ic} - B_{pll-Vc} + B_{PI-I}B_{PI-PV}B_{LPF}B_i \cdot \left(I - B_{pll-Vo}\right)\right] \tag{4.27}$$

According to the superposition theorem, the output current at the PCC is:

$$\Delta i_{cdq} = \frac{1/Y(s)}{1/Y(s)+Z_g(s)}\Delta i_{sdq} - \frac{\Delta v_{gdq}}{1/Y(s)+Z_g(s)} = \left[\Delta i_{sdq} - Y(s) \cdot \Delta v_{gdq}\right] \cdot \frac{1}{I+Y(s)\cdot Z_g(s)} \tag{4.28}$$

The stability is determined by matrix $Y(s) \cdot Z_g(s)$. Therefore, the stable operating range is identified based on the Nyquist plot under multiple operating points.

The maximum output power is subject to static and dynamic power limits. When the grid-side impedance ratio is given, the static power limit can be calculated as equation (4.29) and (4.30).

$$\mathrm{SCR} = \frac{S_{\mathrm{SC}}}{S_N} = \frac{V_g/|Z_g|}{I_{\mathrm{inv(rated)}}} \tag{4.29}$$

$$P_{\mathrm{(p.u.)max}} = i\left[\frac{(R_g/X_g)}{\sqrt{(R_g/X_g)^2+1}} + 1\right]_{od(\text{ p.u. })max} \tag{4.30}$$

When SCR=1, the static power limit is 1 p.u., and the dynamic power limit is only 0.61 p.u., which shows that the dynamic power limit is more stringent than the static. Therefore, the dynamic power limit mainly affects the maximum output power of the grid-connected inverter under a weak grid. If a suitable measure is used to improve the stability, the dynamic power limit will be close to the static value.

$$\mathbf{Y}(s) = \begin{bmatrix} \dfrac{\frac{1}{sL_f+R_f}\cdot\frac{s}{s+\omega_i}+\frac{i_{cd0}}{V_O}\cdot\frac{\omega_p}{s}\cdot\frac{\omega_i}{s+\omega_i}}{1+\frac{\omega_p}{s}\cdot\frac{\omega_i}{s+\omega_i}} & \dfrac{\frac{i_{cq0}}{V_O}\cdot\frac{[(sL_f+R_f)\omega_i+sR_f]\cdot G_{pll}}{(sL_f+R_f)(s+\omega_i)}+\frac{i_{cq0}}{V_O}\cdot\frac{\omega_p}{s}\cdot\frac{\omega_i}{s+\omega_i}}{1+\frac{\omega_p}{s}\cdot\frac{\omega_i}{s+\omega_i}} \\ \dfrac{-I_{max}}{V_o}\cdot\dfrac{\omega_v}{s}\cdot\dfrac{\omega_i}{s+\omega_i} & \dfrac{(1-G_{pll})}{sL_f+R_f}\cdot\dfrac{s}{s+\omega_i} - \dfrac{i_{cd0}}{V_o}\cdot\dfrac{[(sL_f+R_f)\omega_i+sR_f]\cdot G_{pll}}{(sL_f+R_f)(s+\omega_i)} \end{bmatrix} \tag{4.31}$$

where $G_{pll} = (2\zeta\omega_n s + \omega_n^2)/(s^2 + 2\zeta\omega_n s + \omega_n^2)$

The simplified admittance matrix is given as Equ (4.32):

$$\boldsymbol{Y}(s) \approx \begin{bmatrix} \dfrac{(1-G_p)}{sL_f+\omega_i L_f} + \dfrac{G_p}{R_d} & \dfrac{G_p+(1-G_p)\cdot G_{pll}}{-R_q} \\ \dfrac{\omega_v}{-sX_m} & \dfrac{(1-G_{pll})}{sL_f+\omega_i L_f} + \dfrac{G_{pll}}{-R_d} \end{bmatrix} \tag{4.32}$$

where $R_d = V_o/i_{cd0} > 0$， $R_q = V_o/(-i_{cq0}) > 0$， $X_m = V_o/I_{max} > 0$。

The ideal globally stable admittance matrix is:

$$\boldsymbol{Y}_{\text{ideal}}(s)=\begin{bmatrix}\frac{1}{sL_f+\omega_i L_f} & 0\\ 0 & \frac{1}{sL_f+\omega_i L_f}\end{bmatrix} \tag{4.33}$$

Comparing equations (4.32) with (4.33), the negative resistance term introduced by the PLL is the main unstable determinant, and the negative inductance and resistance are another trigger. Therefore, reducing the bandwidth of the PLL, power outer loop, and voltage outer loop can help improve system stability, but at the expense of reduced dynamic performance. An auxiliary control loop can be added to enhance stability while having a faster dynamic response. Figure 4.2 shows the control block diagram of the proposed auxiliary PLL.

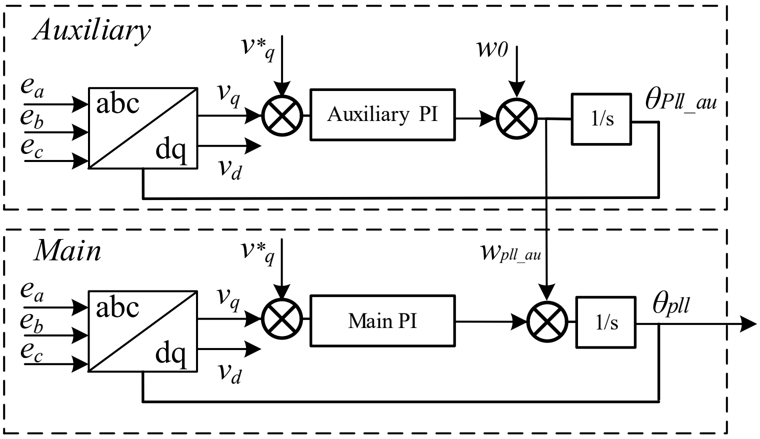

Figure 4.2 Improved control strategy schematic

4.4 Validation

The simulation is completed to prove the applicability of the reshaping method. The control parameters and operating conditions are shown in Appendix B.

4.4.1 Original experiment results

The information of the operating point is input into the state space equation and draws the changing trend of its characteristic root, as shown in Figure 4.3.

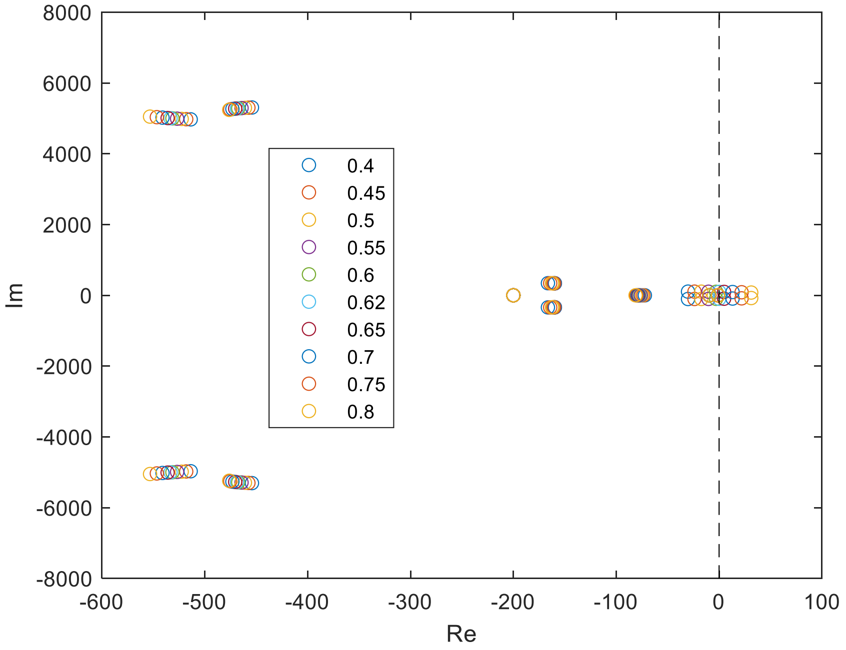

Figure 4.3 Eigenvalue under different power outputs

According to Figure 4.3, the real part of eigenvalues goes towards the right as the output power reference increases from 0.4 p.u. to 0.8 p.u. The active power of the system under a critical stable operation margin is approximately 0.62 p.u.

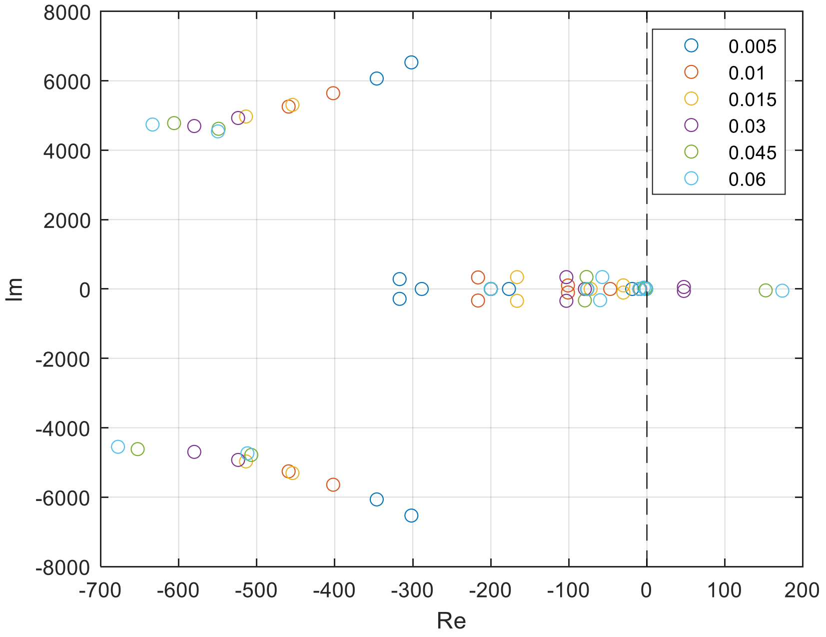

Figure 4.4 Eigenvalues under different system strengths

Figure 4.4 shows the change of eigenvalues with different system strengths by changing the inductance. The real part of the eigenvalue moves to the right, and as the system impedance increases, the stability decreases. This result is consistent with the conclusion of Chapter 3.

The case study has been implemented and verified, and the system parameters follow Appendix B. The traditional control strategy simulation model before improvement is shown in Figures 4.5 - 4.10 below.

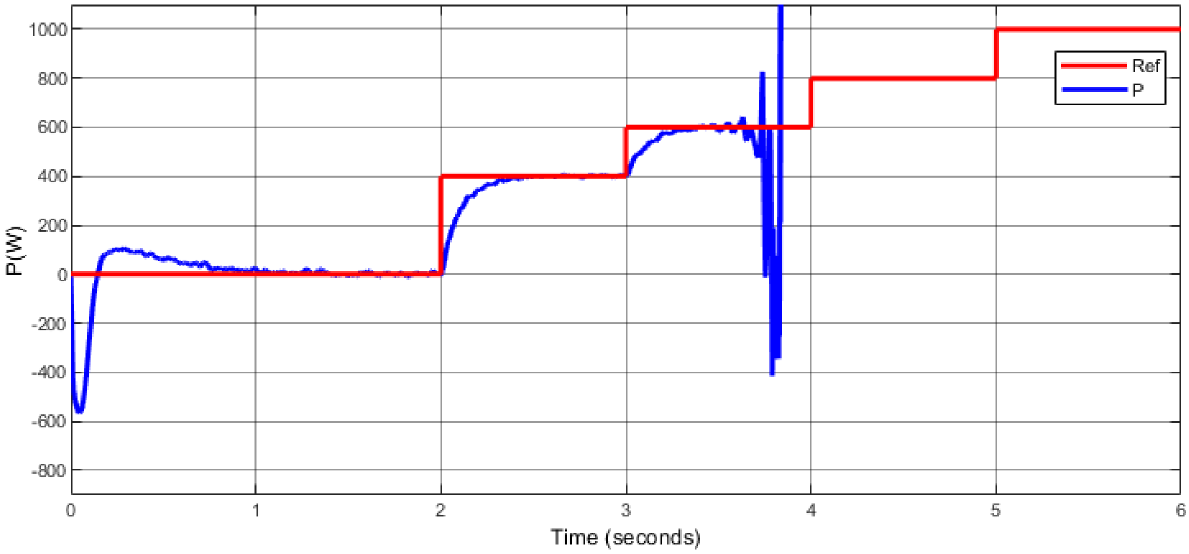

Figure 4.5 Power curve from 0 W to 1000W

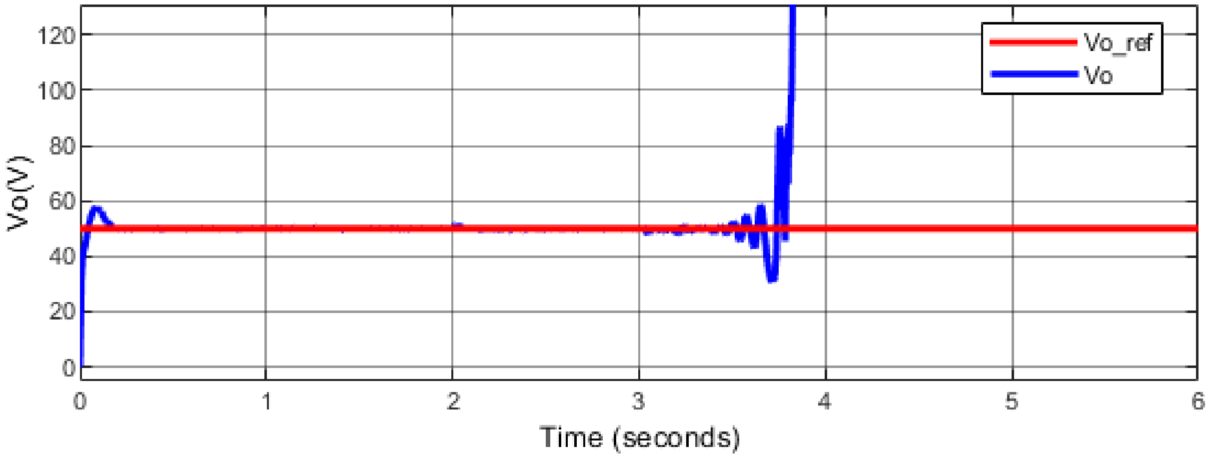

Figure 4.6 Voltage amplitude at PCC

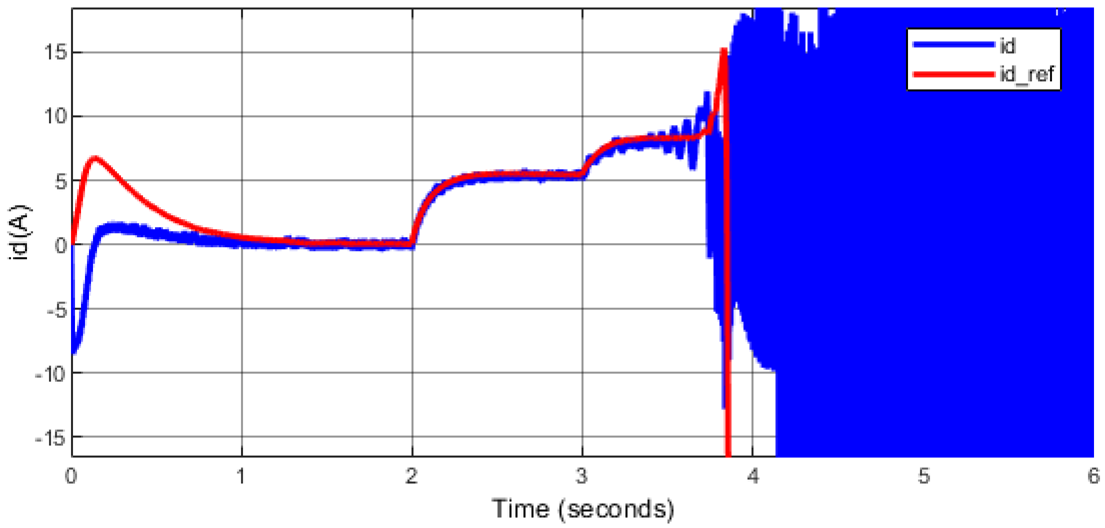

Figure 4.7 Inverter d-axis current output

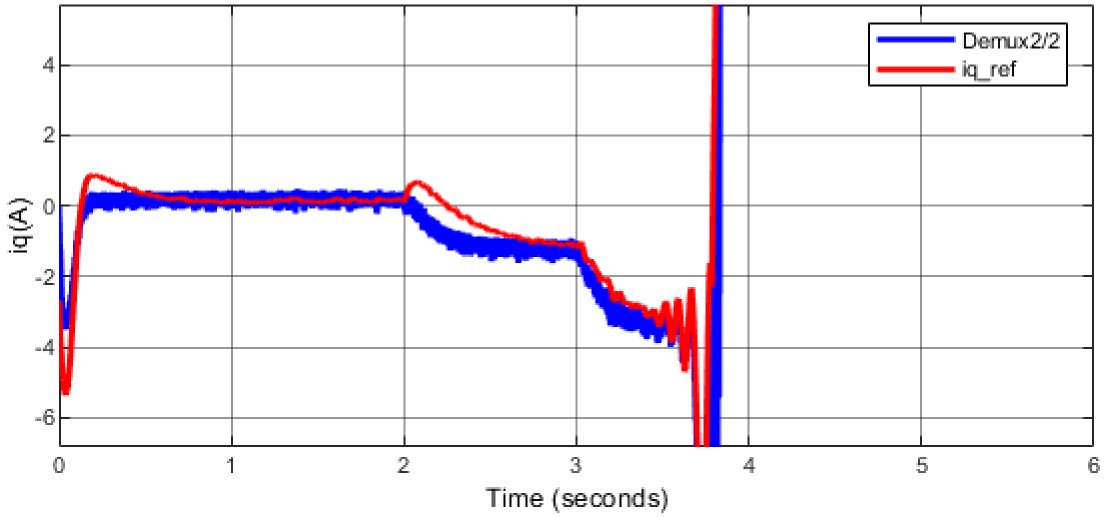

Figure 4.8 Inverter q-axis current output

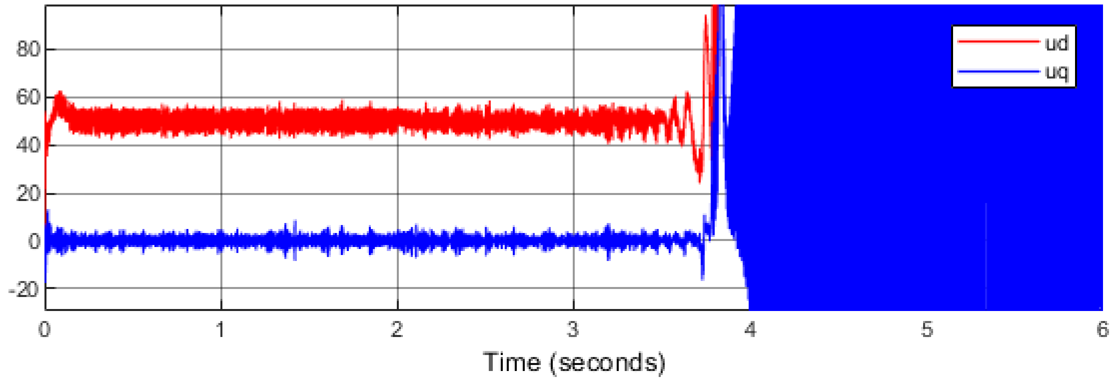

Figure 4.9 PCC point dq axis voltage

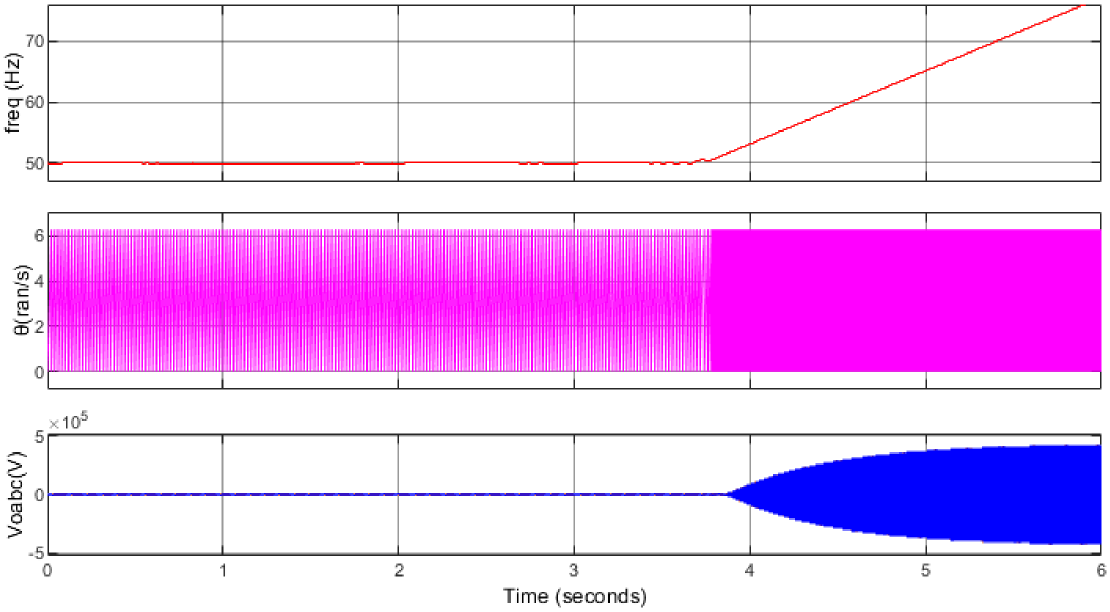

Figure 4.10 Phase locked loop frequency, phase angle, and U_{oabc}.

Figure 4.5-10 shows that the system loses stability with output power increasing to 600 W, and the phase-locked loop loses its tracking ability. This shows that the stability boundary of the traditional control before improvement is slight, and the output power is limited.

4.4.2 Simulation results of impedance reshaping

The enhanced dual PLL impedance reshaping control strategy simulation model is shown in the Figure 4.11-4.16 below.

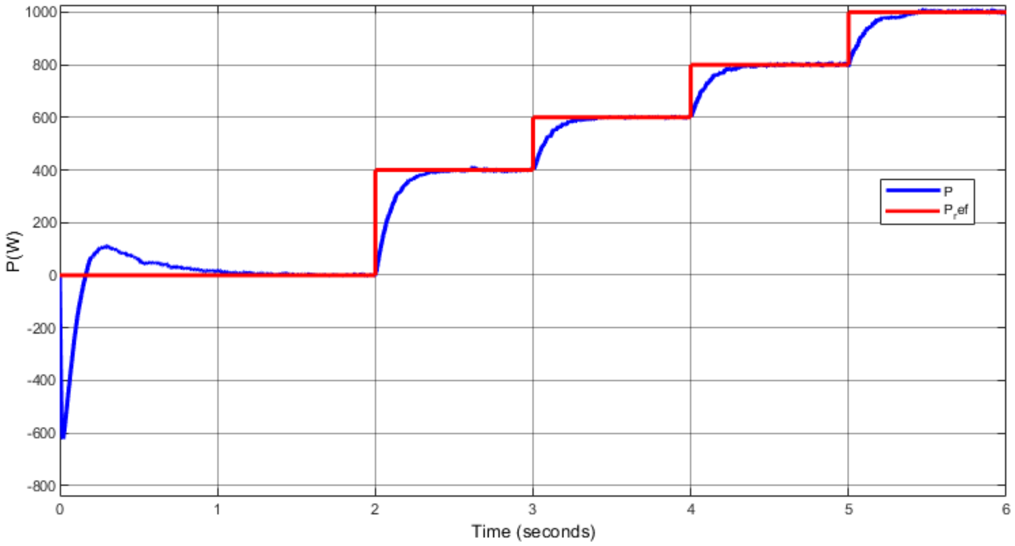

Figure 4.11 Power curve from 0 W to 1000W

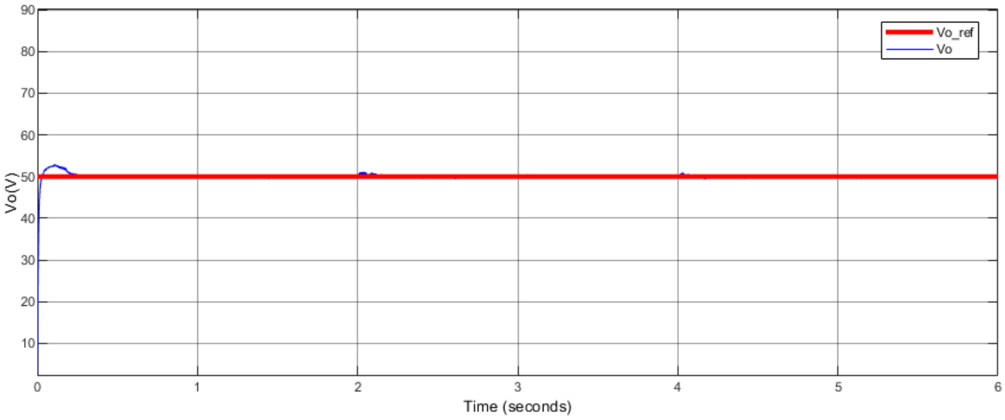

Figure 4.12 Voltage amplitude at PCC

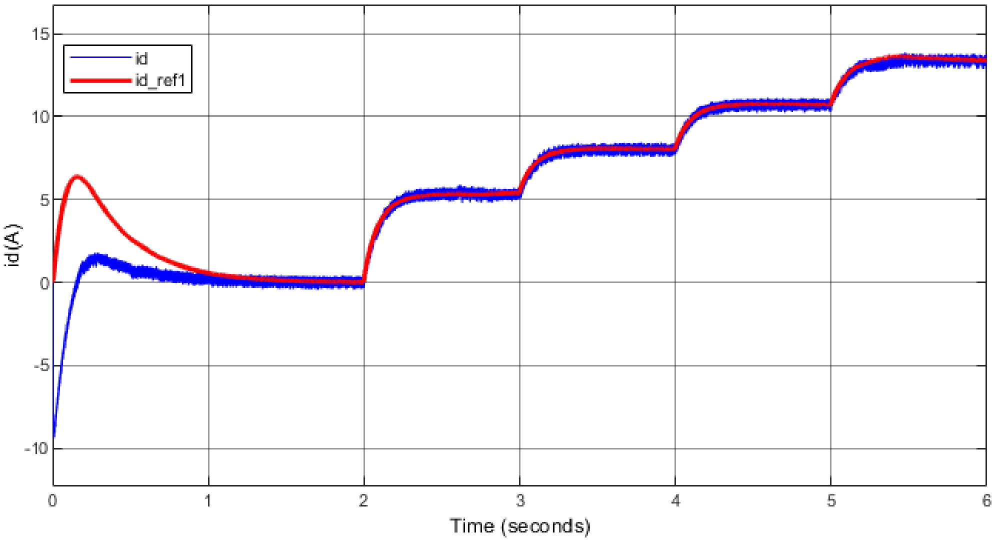

Figure 4.13 Inverter output d-axis current output

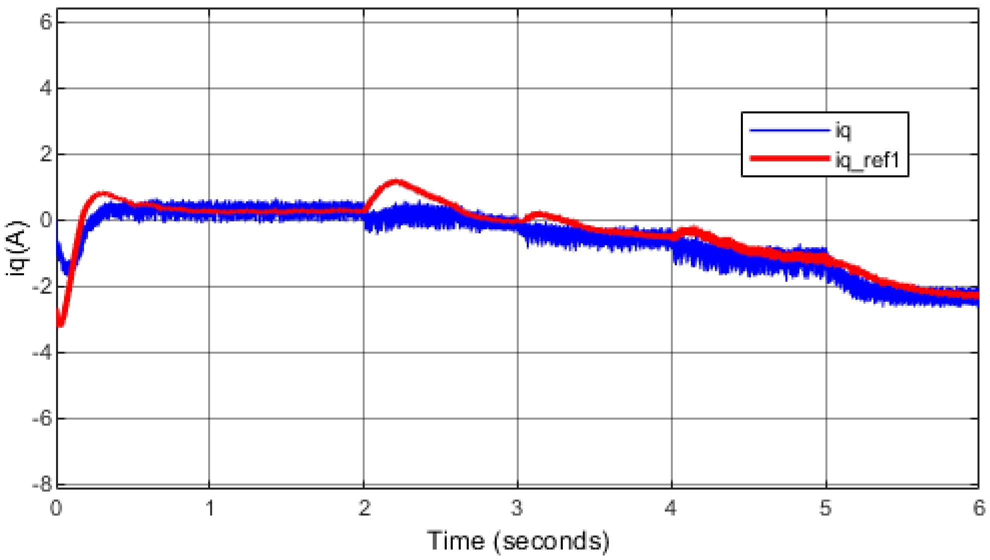

Figure 4.14 Inverter q-axis current output

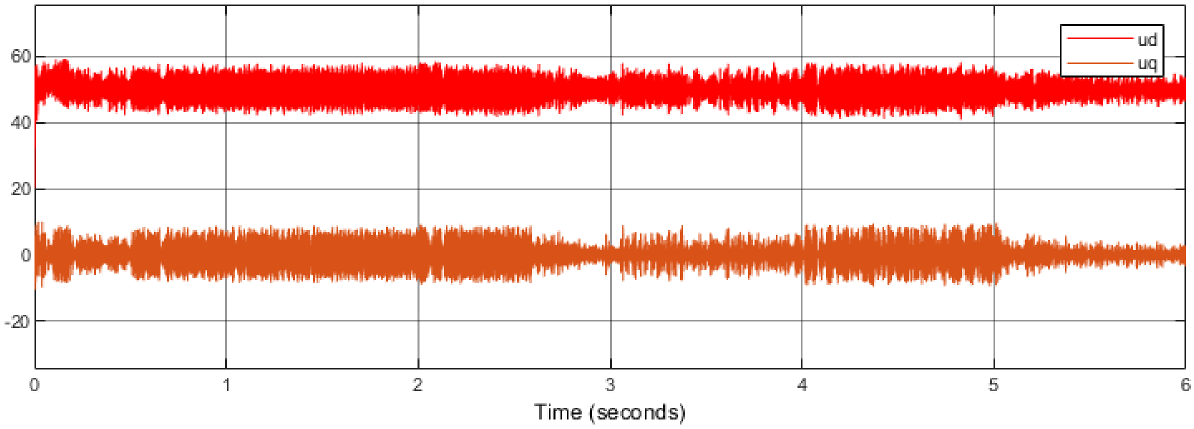

Figure 4.15 dq-axis voltage at PCC point

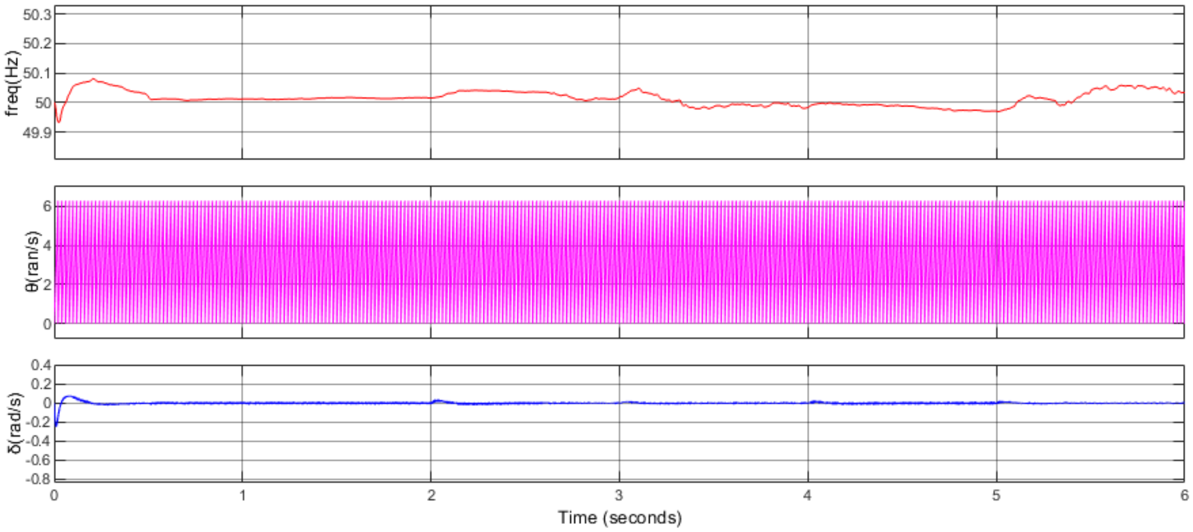

Figure 4.16 Phase-locked loop frequency, phase angle, δ

According to the results, the system operates under output power 0~1000W, and the phase-locked loop tracking ability is satisfying, which indicates that the stable boundaries are extended by impedance reshaping control where the output power range is greatly increased. Besides, as the grid impedance increases, the system strength is weakened, making the operation of the inverter unstable.

4.5 Summary

The frequency-dependent impedance model relies on the control and operating points. Manufacturer and power companies could use this to understand the behaviour of the inverter and grid without revealing the detailed system components and parameters information to their partner. The operating points can be defined according to the impedance information. Besides, the stabilization range can be extended by modifications in the impedance curve or transfer function due to improved control.

For small-scale white-box models, stability analysis can be performed via state-space modelling with detailed parameters. The detailed conclusions are summarized as follows:

(1) The state space equation and impedance model have been established, respectively. Stability conclusions based on state-space equations and impedance models have been verified through time-domain simulations.

(2) Aiming at the problem of the small stable operation range of the inverter, an auxiliary phase-locked loop has been proposed without sacrificing the system's dynamic performance.

5. Impedance tuning methods for black-box model

5.1 Introduction

The white box model provides control and parameters to users which gives freedom to reshap the impedance. This Chapter deals with the black box model in which the control and parameters are unknown to users. Normally, the active power, reactive power, or AC voltage can be set as expected. When the inverter is connected to the wider network, the engineer should find out if it could operate under extreme conditions. The idea to find out the operating range is by adding perturbation and observing the eigenvalue moving direction which is introduced in Section 5.2. The principle of applying this method in stability analysis is given in Section 5.3. In Section 5.4, practical cases provide evidence that this strategy helps tune the operating parameters and enhance stability. Finally, the summary is presented in Section 5.5.

5.2 Perturbation and observation algorithms

Measurement-based optimization can understand the stability boundaries of the system without access to inverter control information. At the same time, it can also analyze the operating conditions under which the inverter has better stability based on the changing trend of the eigenvalues.

Perturbation and observation (P&O) algorithms mainly apply disturbances at the output voltage of the photovoltaic array at a fixed time and then decide the following action with a change in output power to achieve maximum power tracking. In Figure 5.1, we record the power value P1 before the disturbance. When the output voltage increases, we record the power value as P2. Compare the power value. The size of P1 and P2. If the power value P2<P1, the previous step change should be cancelled. Change the direction of the disturbance and modify it to increase

the step size V; if the power value P2>P1, the small step disturbance can be retained. Then the normal direction of the disturbance should be kept and continue to reduce the step size.

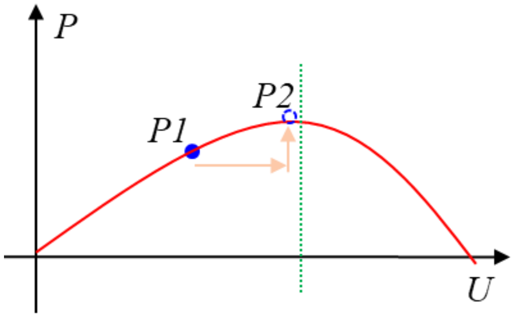

Figure 5.1 Principle of Perturb and Observe Algorithms

5.3 Application in stability analysis

The strategy of perturbation and observation can also be applied in system stability optimization. Since the control of an inverter is often agnostic, operators can usually only adjust a limited number of parameters. The reference output power distance is used here. When it is changed, the system impedance is scanned again to obtain updated characteristic values. Based on the eigenvalue groups under multiple different operating points, a schematic diagram of the operating area boundary can be drawn, as shown in the figure below. Since the effects of the active output are almost monotonic, the deviation trend of the eigenvalue is captured with different references, thereby summarizing whether the impact under current changes is weakened or enhanced.

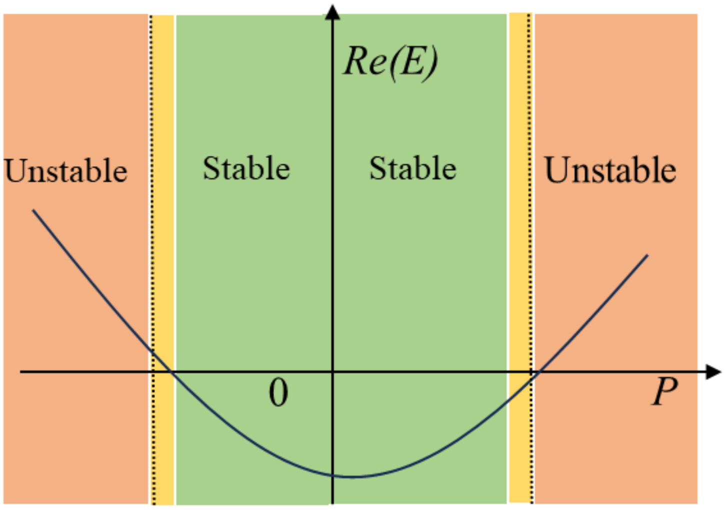

Figure 5.2 The eigenvalues and reference active power

5.4 Validation and experiment

Case 1 is used as a comparison reference object and different SCRs, reference active power and reference AC voltage are designed, respectively. By conducting impedance scanning on the inverter and system at the above operating points, we can obtain the transfer function for determining stability based on the impedance data and obtaining its eigenvalues. The impedance bode plots of test cases are drawn separately, as shown in Figure 5.3.

Table 5.3 Test cases and their conditions

Test cases	SCR	P_ref (p.u.)	Uac_ref (p.u.)	Maximum Damping
Case 1	3.0	1.00	1.00	-18.99
Case 2	2.0	1.00	1.00	-9.23
Case 3	3.0	0.60	1.00	-3.72
Case 4	3.0	1.00	0.95	-16.49

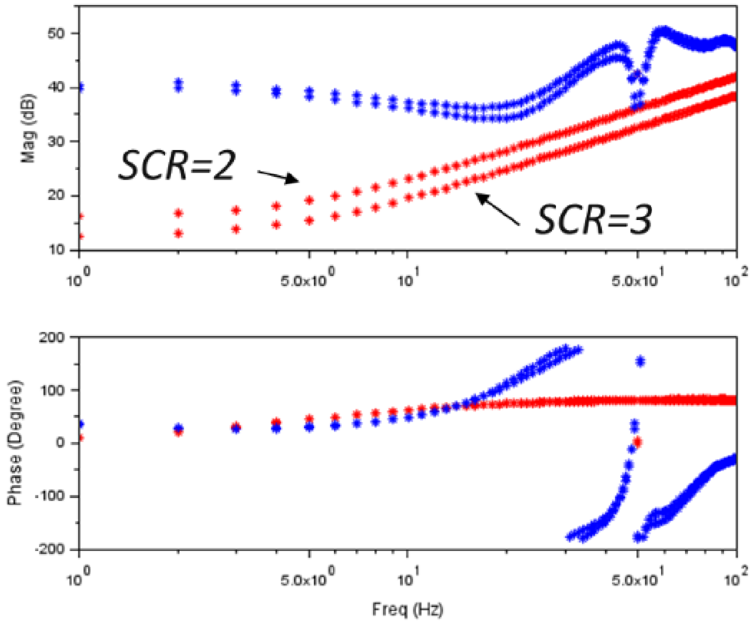

(a) Case 1 and Case 2

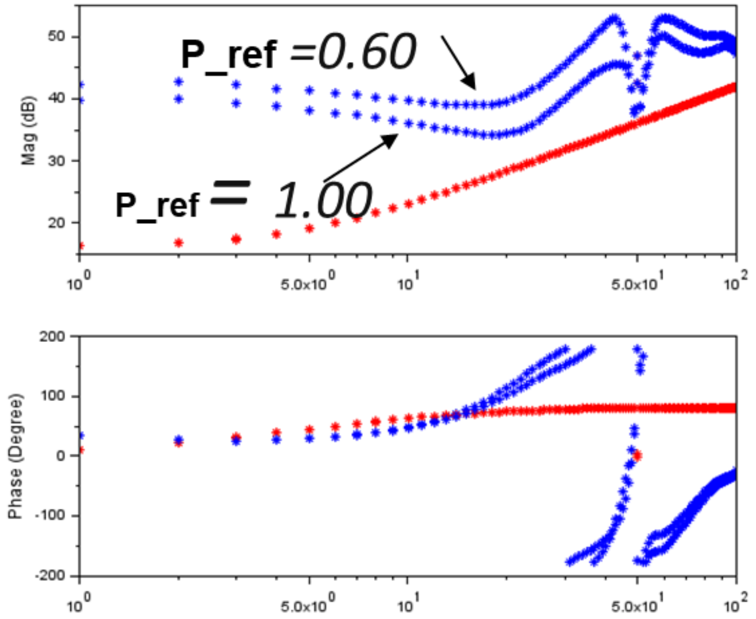

(b) Case 1 and Case 3

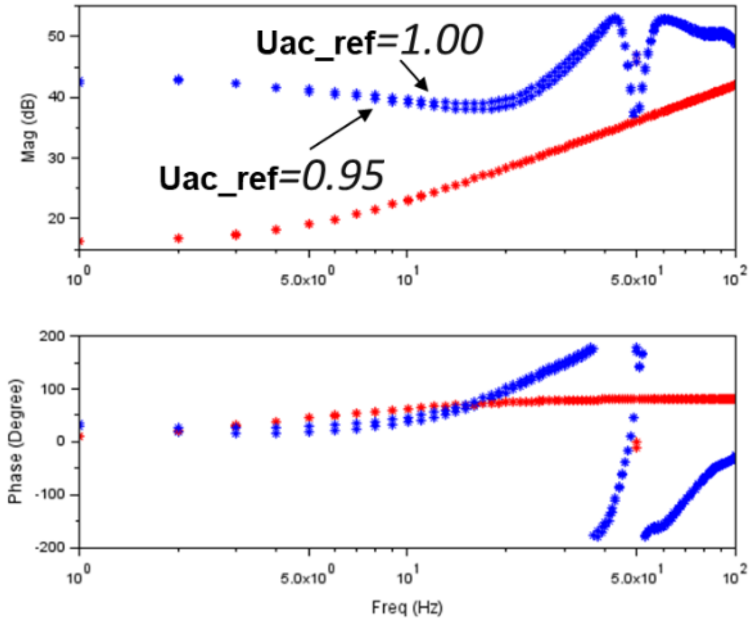

(c) Case 1 and Case 4

Figure 5.3 Bode plots for comparison

To further understand the trend of system eigenvalues changing with parameters, this involves changing P_{ref} in the case of a constant voltage reference value and changing the voltage reference value in the case of a constant active power reference value. The reference value of AC voltage is constant at 1 p.u., and the P_{ref} ranges from 0.1 p.u. to 1.0 p.u., with 0.1 p.u. as a step size of the change. The eigenvalues are plotted in Figure 5.4.

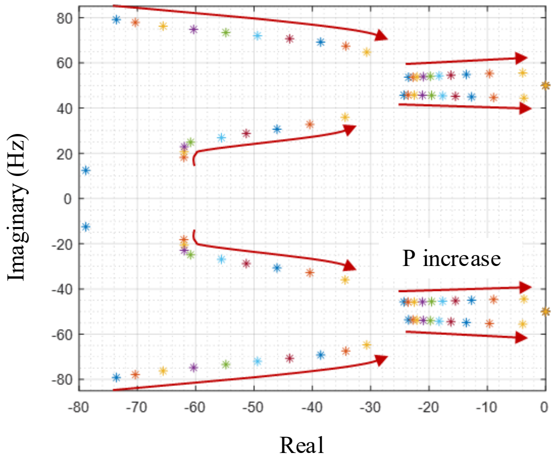

Figure 5.4 Eigenvalue under different P reference

Figure 5.4 shows that as the active reference value increases, the changing trend of the eigenvalues. The real part of the eigenvalue increases, the system damping decreases, and the system stability decreases. It can be concluded that with a smaller active power output, the system is more stable.

The P_{ref} is constant at 1.0 p.u., and the U_{acref} is from 0.95 p.u. to 1.05 p.u., with 0.01 p.u. as a step size. The eigenvalues are plotted in Figure 5.5.

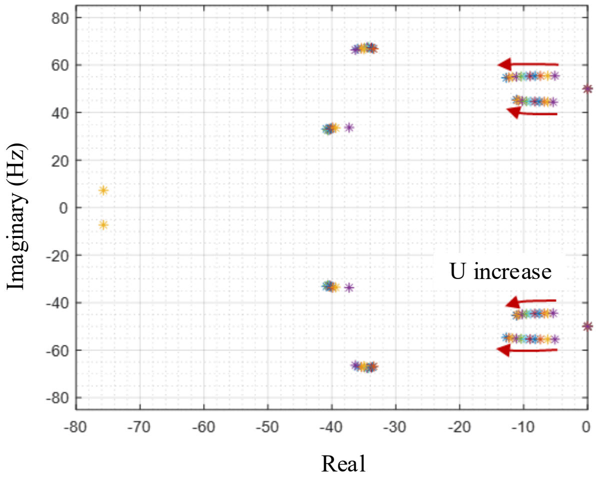

Figure 5.5 Eigenvalue under different U_{ac} reference

Figure 5.5 shows that as the AC voltage reference value increases, the changing trend of the eigenvalues. The real part of the eigenvalue decreases, the system damping increases and the system stability increases. It can be concluded that with a high AC voltage reference, the system is more stable. A preliminary conclusion can be arrived based on Figure 5.4 and Figure 5.5. Compared with the voltage reference of the system, the system stability is more sensitive to the reference of active power.

5.5 Summary

Inverter manufacturers normally cannot share control details, making the analysis of system stability more difficult. The detailed conclusions are summarized as follows:

1. A tuning method with perturbation and observation has been proposed for the black box model which is a result-based optimization method suitable for the application. With the impedance model characteristics obtained by impedance measurements, the eigenvalues of the power grid can be obtained to determine the stability.
2. The eigenvalues shift due to disturbance can guide the parameter setting of the inverter. This method can be used to find the operating region where the inverter operates stably, thereby guiding the engineers to deal with stability analysis with the black box model.

6. Data-driven automation method: clustering and aggregation of multiple operating point impedance models

6.1 Introduction

In principle, an impedance model corresponds to an operating point. This means that the impedance model is operating point dependent as it is a kind of small signal model. For a practical application, we will need to generate a very large number of impedance models. Sharing a very large number of impedance models with stakeholders is neither efficient nor practical. Hence the major objective of this Chapter is to propose a data-driven clustering method and then an aggregation method to derive a small number of impedance models from a very large number of impedance models across a very large number of operating points. Furthermore, based on the methods proposed, a data-driven automation toolbox is developed. Using the data-driven automation toolbox can dramatically reduce the developer's workload.

This Chapter is arranged as follows. The impedance models for multiple operating points based on measurements are presented in Section 6.2. A clustering method with an index for identifying the similarity of impedance data is proposed in Section 6.3. An aggregation method is proposed in Section 6.4 where errors of eigenvalues between the aggregated model and each model before the aggregation should be within the tolerance. Then, the key features and interface of the toolbox are demonstrated in Section 6.5. Finally, the summary is presented in Section 6.6.

6.2 Multiple operating points

6.2.1 Problem description

Linearized analysis methods for a specific operating point represent the stability of an interactive system at that operating point. Impedance measurements must be conducted at multiple operating points to analyse the stability under numerous conditions and enhance the system's robustness. Researchers developed one impedance tool [110] to automatically obtain the impedance of the inverter but it lacks ability to run large number of operating points. Another stability analysis tool [111] adopts repeat cases whereas it has some limitations on large-scale networks. Comprehensively weighing the ease of use and universality of the toolbox, the toolbox proposed in the thesis has a higher practical value and can be applied to large system models while considering impedance models at multiple operating points.

Table 6.1 provides the operating point information determined by active power reference value, reactive power reference value, SCR, etc. To efficiently obtain the impedance model at multiple operating points, starting a simulation with initial conditions is normally required, which is achieved using a Snapshot File. This feature enables multiple runs with the pre-set condition, and the parameters are changed with Python scripts.

In theory, it is possible to test all operating points to provide a robust model to developers, but it is not practical. This is because traversing all operating points will take considerable time and effort. Therefore, it is more sensible to classify and aggregate the results of many operating points and select an appropriate number of representative impedance curves to represent the entire curve.

Table 6.1 Variables under multiple operating points

Parameters	**P_ref**	**Uac_ref**	**SCR**	**X (to be confirmed)**
Row 1	1.0	1.05	3.0	……
Row 2	0.9	1.04	2.5	……
Row 3	0.8	1.03	2.0	……
……	……	……	……	……

6.2.2 Multiple operating point

The following contents cover three typical cases demonstrating why this impedance-based stability analysis relies on multiple operating data.

Table 6.2 Testing cases.

Case No.	Uac (p.u.)	Before step change	After step change
1	1.00	0.48	0.50
2	0.98	0.98	1.00
3	0.97	0.98	1.00

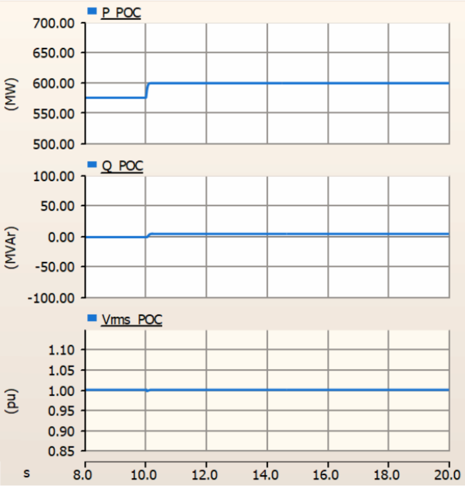

(a) P, Q, and Vrms at PCC

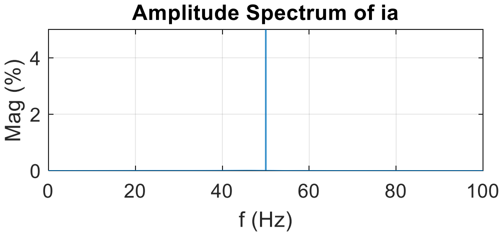

(b) FFT results

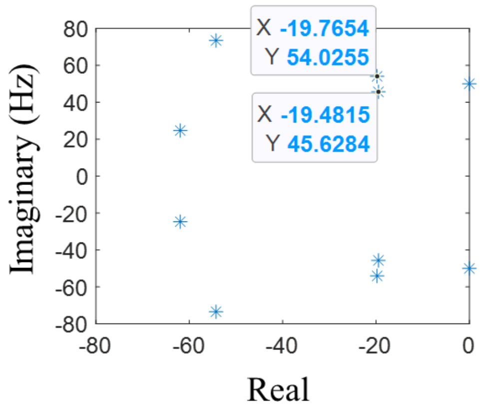

(c) Eigenvalues

Figure 6.1 Results for Case 1

Figure 6.1 indicates that case 1 belongs to a stable region, and the interconnected system is stable. The damping values are negative, and no oscillations were observed.

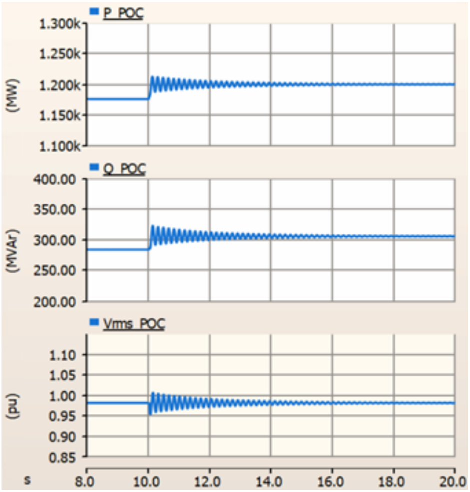

(a) P, Q, and Vrms at PCC

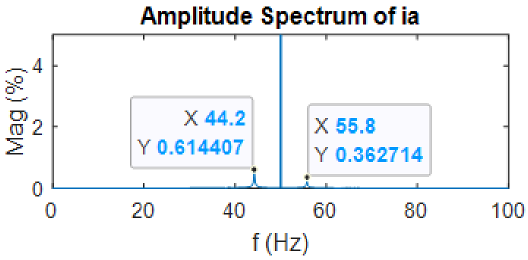

(b) FFT results

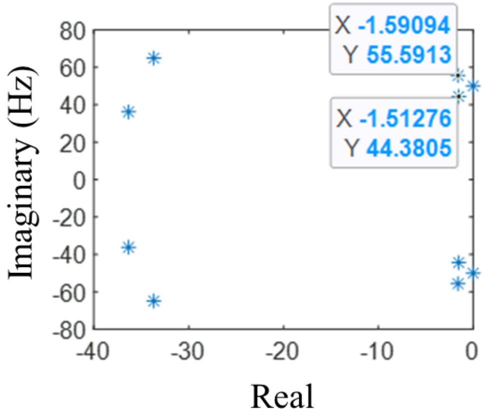

(c) Eigenvalues

Figure 6.2 Results for Case 2

Figure 6.2 shows that the interconnected system is at a stable margin for case two. Damping values are negative and small and Poor damped oscillations were observed. Oscillation frequencies are 44.4 Hz and 55.6 Hz which are observed from the FFT module, and 44.2 Hz and 55.8 Hz are estimated from impedance data.

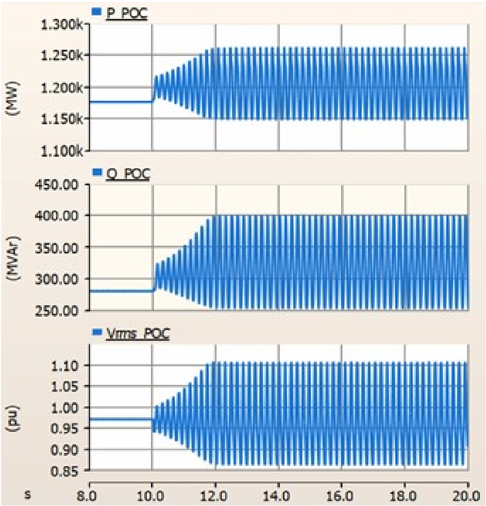

(a) P, Q, and Vrms at PCC

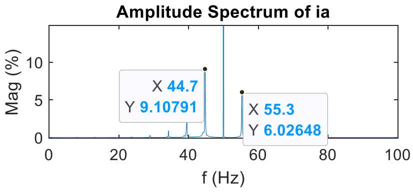

(b) FFT results

Figure 6.3 Results for Case 3

Figure 6.3 shows that the condition is located in an unstable area and the interconnected system is unstable for case 3. Damping values are positive and divergent oscillations were observed. Oscillation frequencies from EMT simulation are 44.4 Hz and 55.6 Hz, and from impedance scanning are 44.7 Hz and 55.3 Hz. It should be noted that the impedance measurements are based on stable state. Therefore, the eigenvalues are unknown for this unstable case.

The investigation of the effect of multiple operating points on the impedance curve is completed. It assumes that the control objective includes the P_{ref} and the U_{acref}. Then, the map for the operating point has two dime Dimensions (P_{ref} and U_{acref}). Therefore, the bode figure becomes a 3D plot with P_{ref} or U_{acref} serving as the additional dimensions. The U_{acref} is fixed as 1 p.u., and the P_{ref} is within 0.1 p.u. to 1.0 p.u. The impedance is plotted in Figure 6.4. When the P_{ref} is constant, the three-dimensional impedance Bode diagram is obtained by changing the AC voltage reference range within 0.95 p.u. -1.05 p.u. in Figure 6.5.

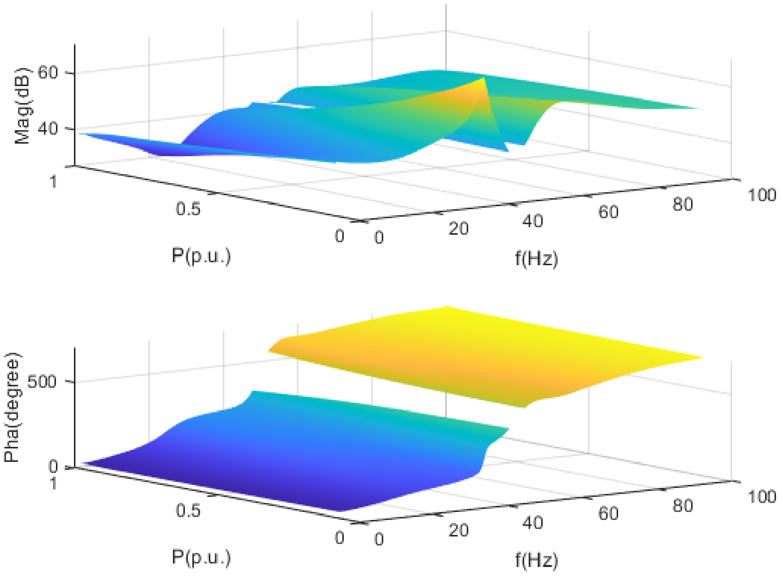

Figure 6.4 Bode plots with a different active power reference

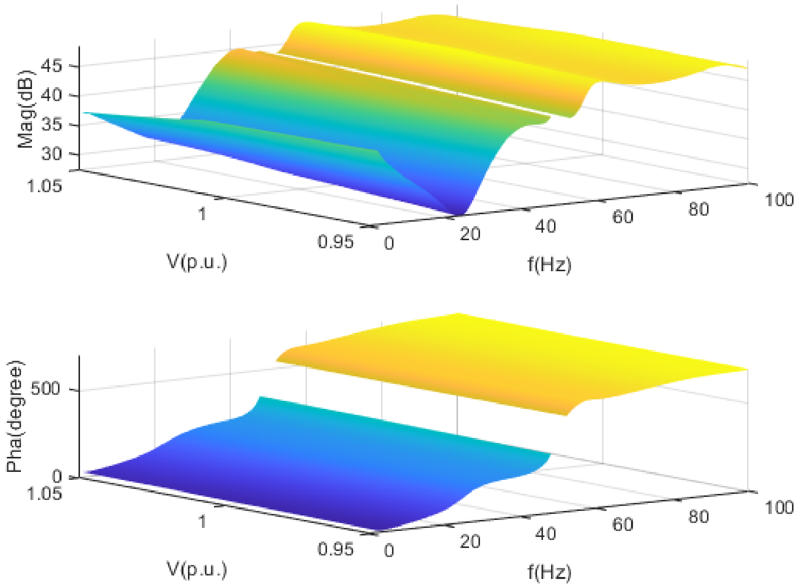

Figure 6.5 Bode plots with different AC voltage reference

Figures 6.4 and 6.5 show the impedance data under multiple operating points. The impedance is less sensitive to AC voltage reference compared to output power.

The intense transfer functions are unapplicable for practical engineering applications, so data processing including clustering and aggregation methods, are implemented, and described in detail in the following sections.

6.3 Clustering method of impedance data sets

6.3.1 Conventional clustering method

The large number of run points results in a larger number of transfer functions. Grouping analysis based on the characteristics of the impedance dataset is performed to group similar data in a cluster while being able to capture the differences between groups. The dominant classification methods include the grid by the fixed range split method and the K-means method with a set number of clusters. However, there is no specific method that especially satisfies industrial needs.

(1) Fixed range split: Data sets in grids of the same size form a cluster. The amount of data in the same grid may be different, but their parameters all belong to a particular range. Neighbouring grids also have similar data characteristics.

(2) K-Means: The Kmeans method starts by setting the number of clusters. Then generate the corresponding number of initial values, sort the data points in order, and select the most similar data centers to form the cluster. This method will cause the results to change due to the different locations of the initial centres. In addition, the number of clusters also affects the accuracy of the aggregated data.

$$J = \sum_{j=1}^{k} \sum_{i=1}^{n} \| x_i^{(j)} - c_j \|^2 \tag{6.1}$$

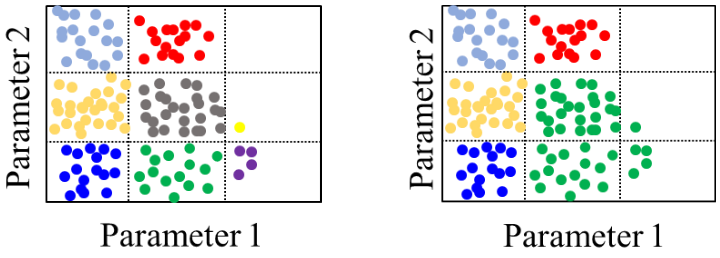

Figure. 6.6 Clustering on operating point using (a) fixed range split and (b) K-Means.

$$S_j^{(t)} = \{x_i : \|x_i - c_j^{(t)}\|^2 \le \|x_i - c_j^{(t)}\|^2 \forall j, 1 \le j \le k\} \tag{6.2}$$

$$c_j^{(t+1)} = \frac{1}{|S_j^{(t)}|} \sum_{x_i \in S_j^{(t)}} x_i \tag{6.3}$$

where t is the iteration times. x_i is each data point, S_j represents the cluster, c_j is the nearest centroid.

Grid methods have the drawback of low efficiency, and a small amount of data can occupy a grid. Kmeans methods can reduce the error between the aggregated data and the original data by increasing the number of clusters. However, it does not ensure that the accuracy meets the specified threshold, which is not applicable to practical engineering. The current challenge is defining the two impedance curves that are close to each other and should be clustered in the same group.

6.3.2 Discrete Frechet distance (DFD)

The traditional degree of similarity between two sets of data as judged by the MSE metric is not applicable to the classification of impedance data. The DFD method not only considers the distances of the corresponding data but also provides elasticity-like distances, which can mitigate the interference of the data bias due to the measurement error. Given two sequences of points, ***f*** and ***g*** donate *f*(P)=($P_1 \cdots P_2$, ··· P_i, ···, P_m) and g(Q)=(Q_1, Q_2, ···, Q_j, ···, Qn) where(P_1, Q_1)are the starting points, and(Pm, Qn)are the endpoints. The shortest rope length L (i, j) represents the maximum DFD dF (*f*, *g*) between f(P) and g(Q).

$$L(i,j) = \max_{t} L(t) = \max_{t} \left\| P_{i(t)} - Q_{j(t)} \right\| \tag{6.4}$$

where $\left\| P_{i(t)} - Q_{j(t)} \right\|$ is the Euclidean Distance between two points $\boldsymbol{P}_i$ and $\boldsymbol{Q}_j$ at time t.

$$\mathrm{d}_{\mathcal{F}}(f,g) = \min_{(i,j)\in\Pi(m,n)} L(i,j) = \min_{(i,j)\in\Pi(m,n)} \max_{t} \|P_{i(t)} - Q_{j(t)}\| \tag{6.5}$$

The distance dF(m, n) between f(P) and g(Q) can be calculated with (6.6).

$$\mathrm{d}_{\mathcal{F}}(m,n) = max(\|P_{i(t)} - Q_{j(t)}\|, min(\mathrm{d}_{\mathcal{F}}(m-1,n), \mathrm{d}_{\mathcal{F}}(m,n-1))) \tag{6.6}$$

Then, two sets of frequency domain impedance data can be evaluated to identify how close they are to each other.

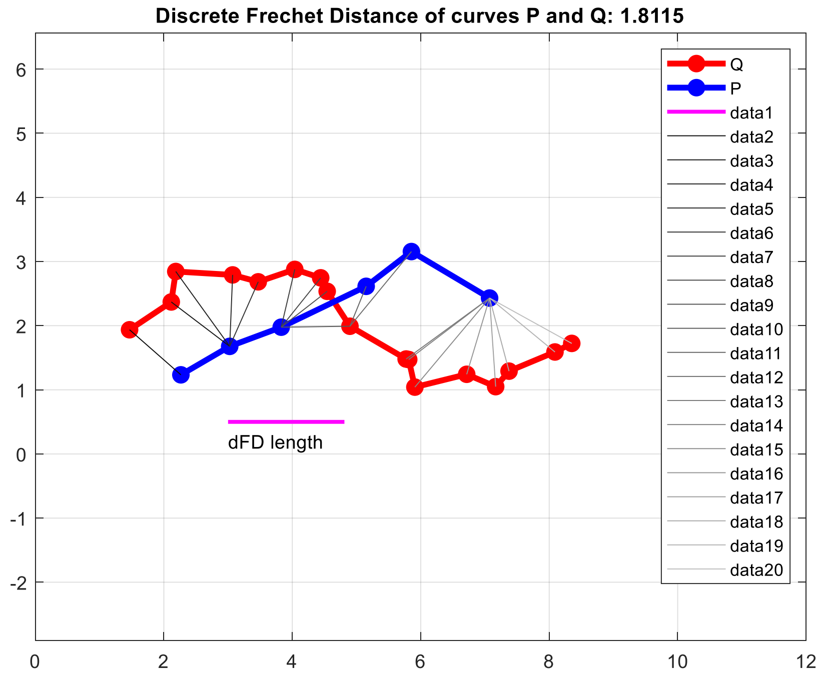

Figure 6.7 Schematic diagram of DFD

Figure 6.7 shows an example case of the DFD algorithm. There are two data sets (6 data in set P and 16 data in set Q). The length of the solid black line between corresponding data points is the distance value when calculating DFD. MSE cannot be used to evaluate the similarity of this kind of data set because the two data sets have different amounts of data, and their correspondence is difficult to determine.

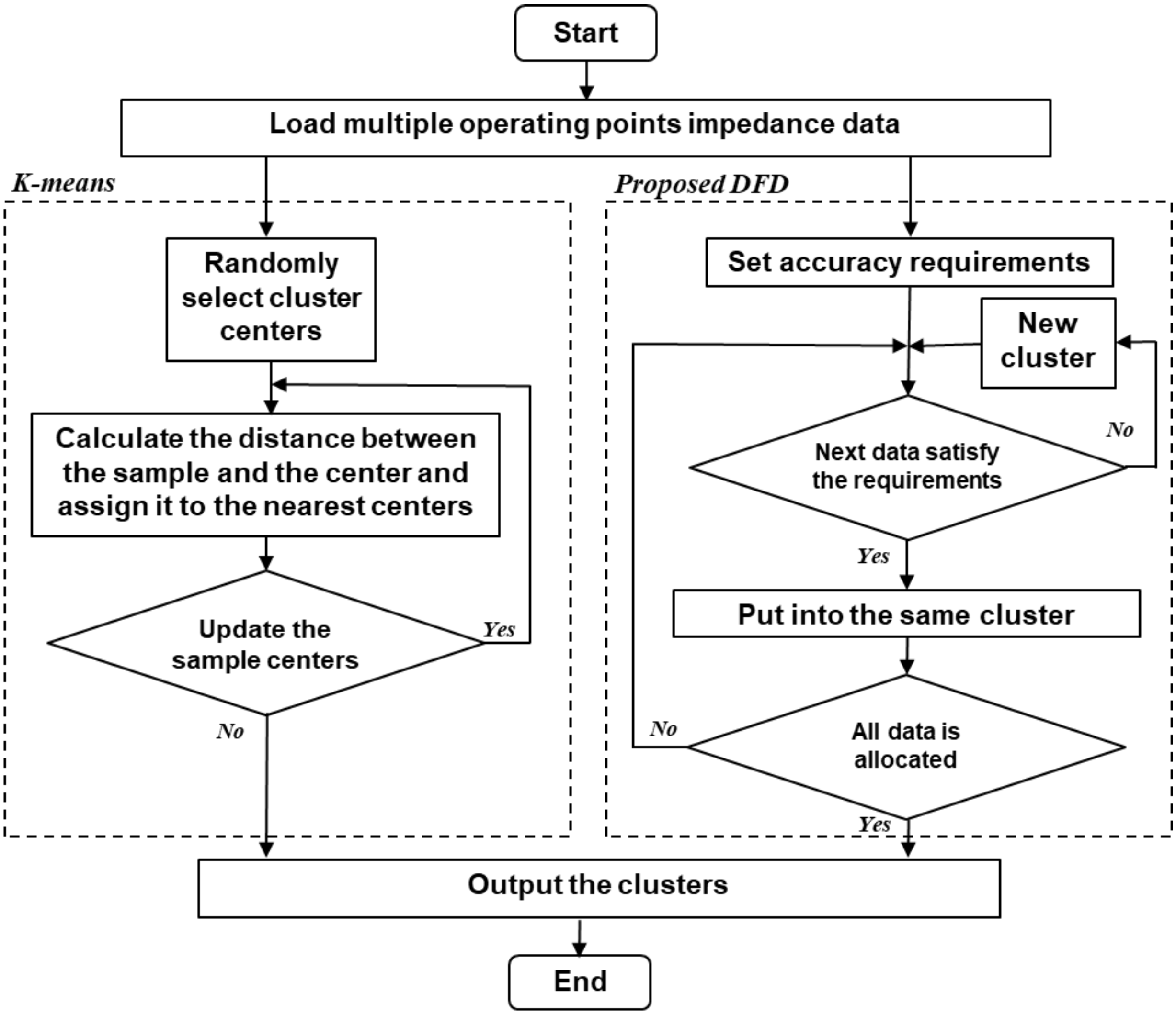

Figure 6.8 Flowchart for K-means and DFD

Figure 6.8 describes the main steps to perform the MSE and DFD algorithms. The major difference is that the K-means algorithm sets the number of clusters at the beginning, while the DFD method sets the clustering threshold.

6.3.3 Experiments and validation

The DFD method evaluates the similarity between the different operating points and the comparison to MSE is presented in Figure 6.9.

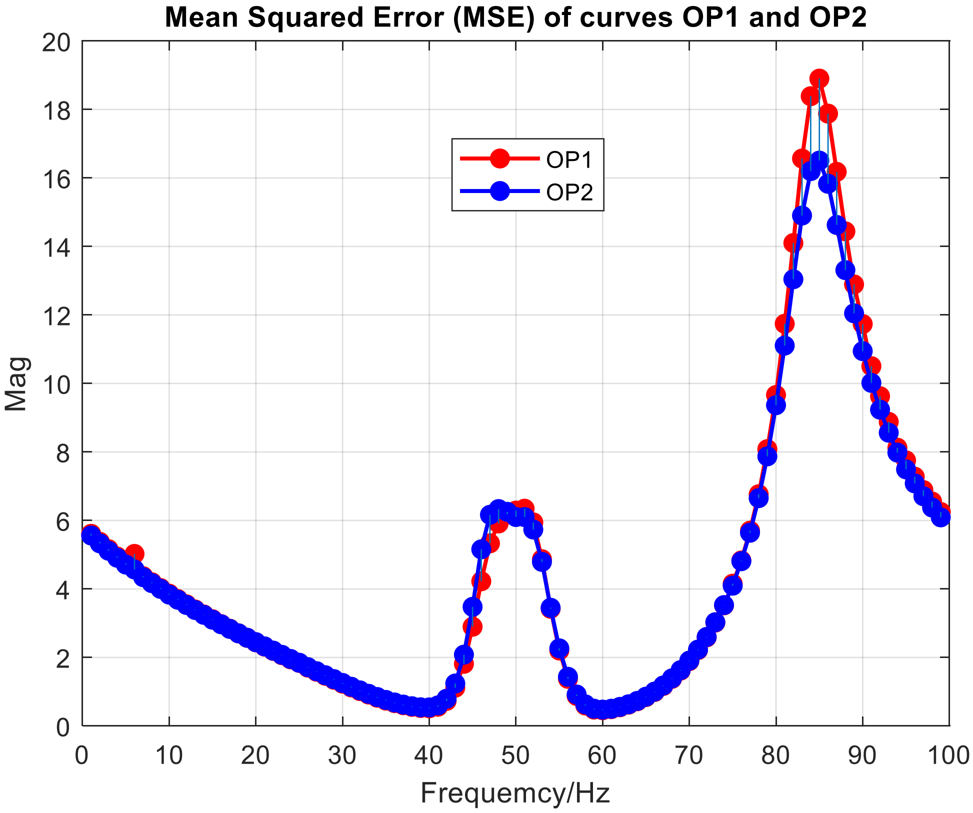

(a)

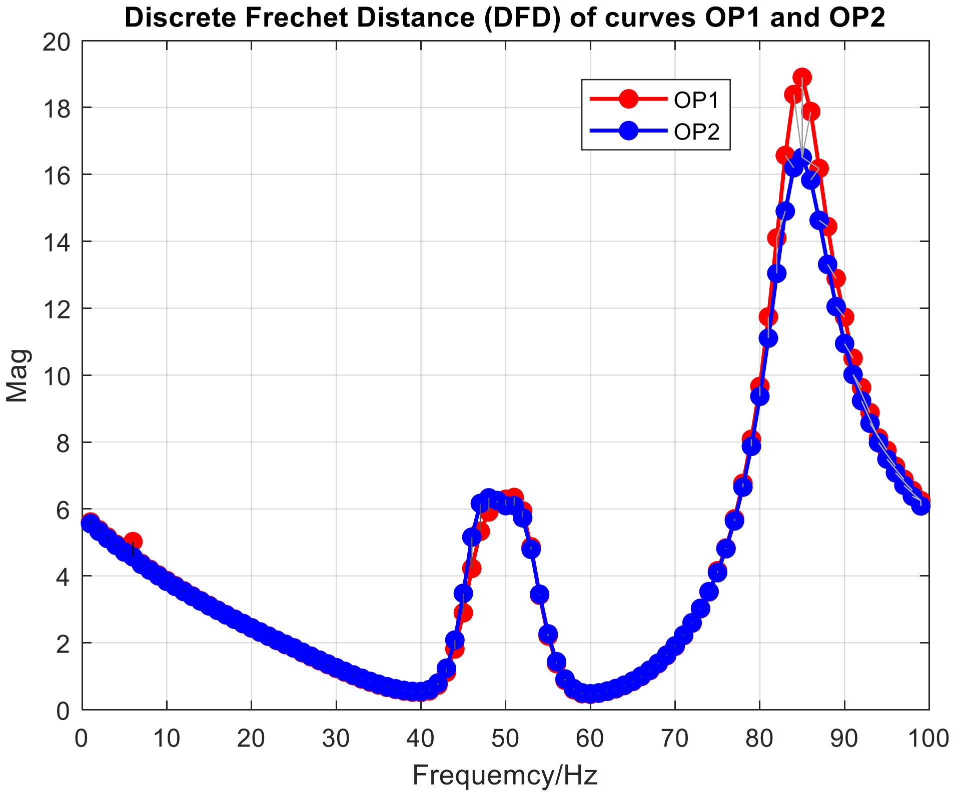

(b)

Figure 6.9 Similarity evaluation (a) MSE (b) DFD

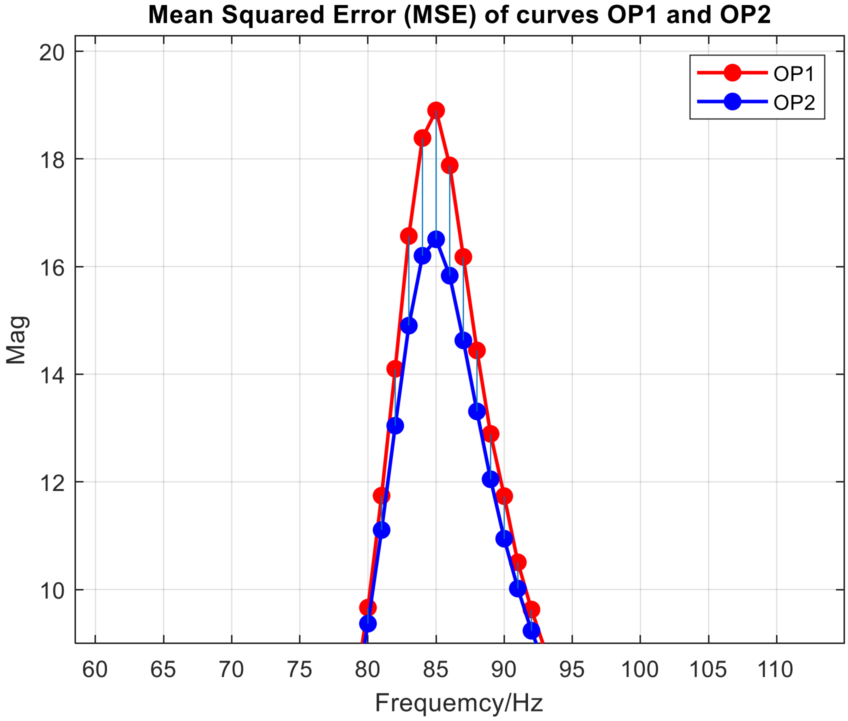

(a)

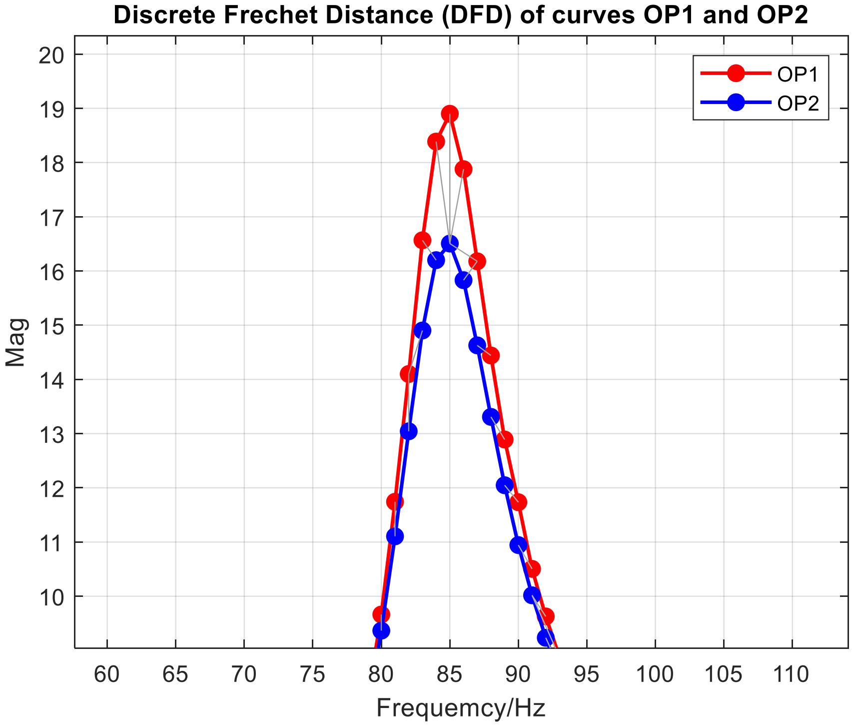

(b)

Figure 6.10 Partial magnification of results (a) DFD (b) MSE

Figures 6.9 and 6.10 provide the part of the results. The DFD distance is defined as the connection points at similar locations in the two sets of data instead of connecting data at corresponding frequencies in the MSE algorithm. The data between 82 Hz to 87 Hz is taken as an example. The MSE distance is more than 2 which indicates that two sets of data should be divided into different clusters. And the DFD results are within 0.5 which suggests the two sets of data should be clustered. Even these two sets of data should be clustered whereas the MSE would give different decisions. DFD considers the distance between adjacent data according to the sequence order of the data, which is suitable for similarity analysis of impedance data. Table 6.2 shows the operating points information to generate the data set for clustering.

Table 6.2 Dataset for clustering under multiple operating points

Operating points	Min	Max	Resolution	Case number
SCR	1.30	4.90	0.40	10
U_{ref} p.u.	0.95	1.05	0.01	11
P_{ref} p.u.	0.10	1.00	0.10	10
			Total:	1100

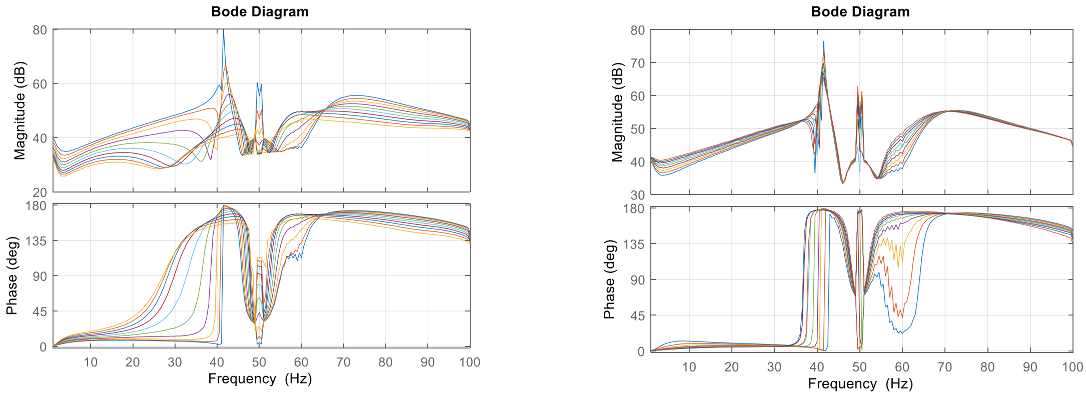

(a) (b)

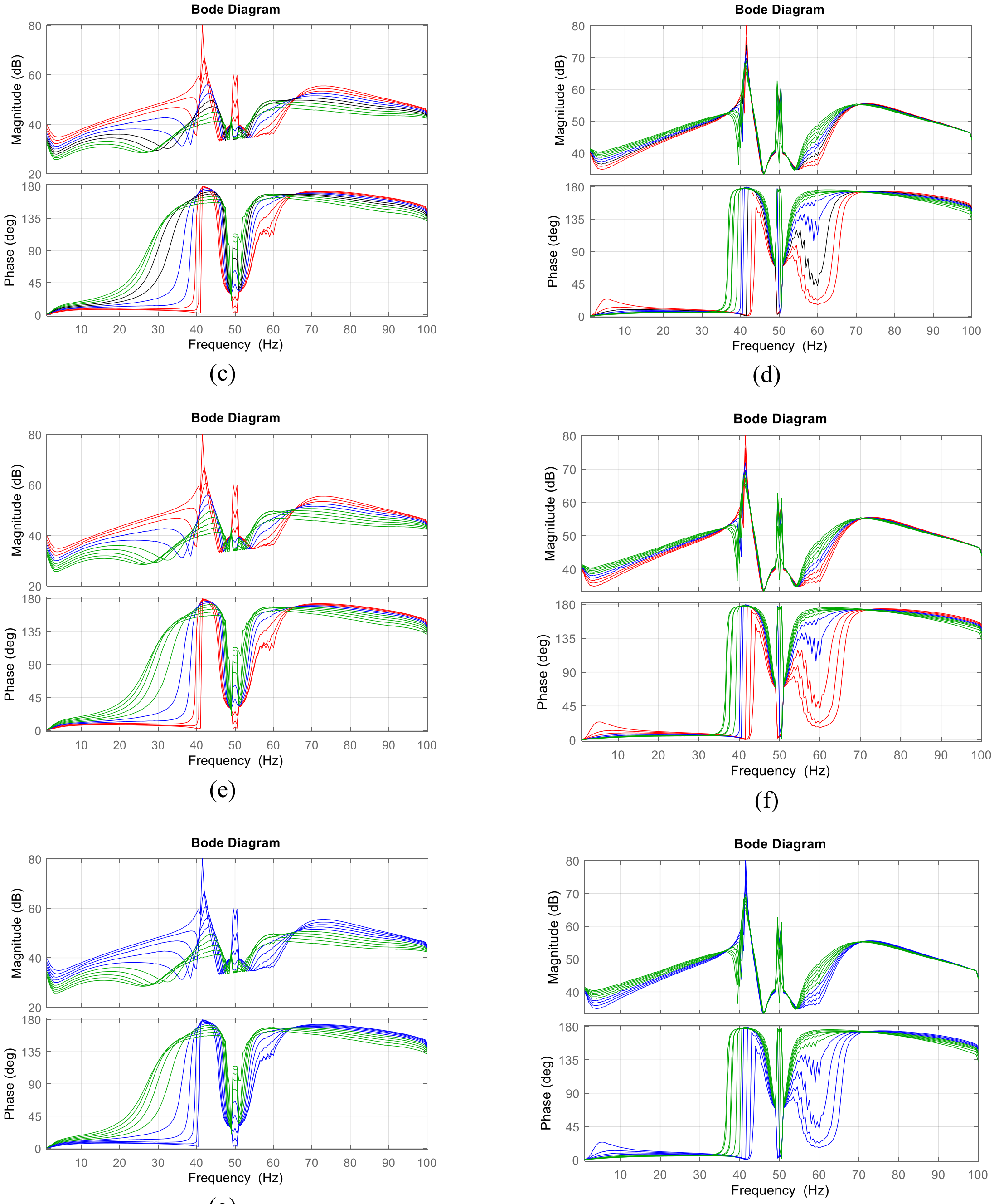

(c) (d) (e) (f) (g) (h)

Figure 6.11 Clustering results. (a) P cluster=10; (b) U cluster=10; (c) P cluster=5; (d) U cluster=5; (e) P cluster=3; (f) U cluster=3; (g) P cluster=2; (h) U cluster=2.

Figure 6.11 describes the results of clustering with multiple operating points. Ten operating points with different P reference have been clustered into 10 groups, 5 groups, 3 groups, and 2 groups. The same principle is also applied to the operating point data clustering with different voltage reference values. Table 6.3 shows the comparison between MSE values and DFD values. The DFD considers the distance of the real data to its closest predicted data, which is smaller than MSE.

Table 6.3 Comparison between MSE and DFD

Operating points (P_{ref} (p.u.))	MSE	DFD	Proportion
0.1	0.007284	0.005293	0.72661
0.2	0.005652	0.003088	0.54635
0.3	0.008230	0.004561	0.554226
0.4	0.002149	0.001412	0.657132
0.5	0.006248	0.003958	0.633424
0.6	0.004962	0.003503	0.705969
0.7	0.002846	0.001679	0.589991
0.8	0.002483	0.001253	0.504677
0.9	0.004249	0.002247	0.528868
1.0	0.009641	0.006483	0.672421

6.4 Aggregation of impedance models

6.4.1 Data shift method

Some impedance data is divided into the same cluster and should be aggregated with one transfer function. The conventional method is to calculate the average value of the data sets and the average value will represent the whole data. When there are individual missing or outliers in the data, there will be large differences in the average values. This chapter proposes a shift-based data aggregation method by adding a small frequency shift to the impedance data. The aggregated transfer function obtained by this method takes all original data into account and can cope with missing data.

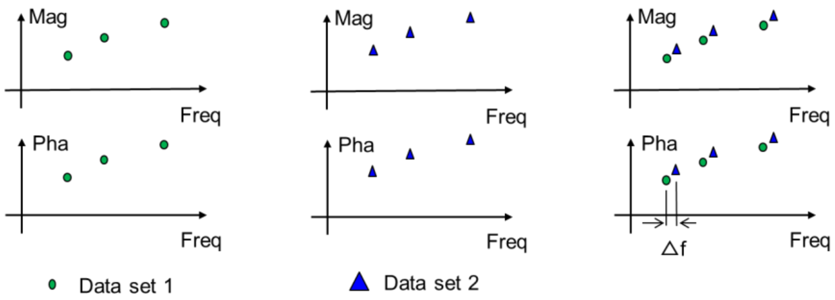

Figure 6.12 Data shift for impedance data

Figure 6.12 shows the principle of the data shift method. The shift frequency $\triangle f$ is normally set as 1% of the original frequency. Then the aggregated transfer function can be estimated with the newly generated data set.

The average mean square error (AMSE) defines the difference between the estimated aggregated transfer function and the actual impedance data is given as follows:

$$AMSE = \frac{\sum_{i=1}^{n} MSE_i}{n} = \frac{\sum_{i=1}^{n}(\frac{1}{N}\sum_{j=1}^{N}\left(Y_{Data(j)} - Y_{TF(j)}\right)^2)}{n} \qquad (6.7)$$

where the number of operating points is n in one cluster and the number of the data is N in one operating point. $Y_{Data(j)}$ represents the j-th impedance data and $Y_{TF(j)}$represents the data from the estimated transfer function.

6.4.2 Experiments and validation

The aggregated impedance model can capture the main characteristics of the raw models.

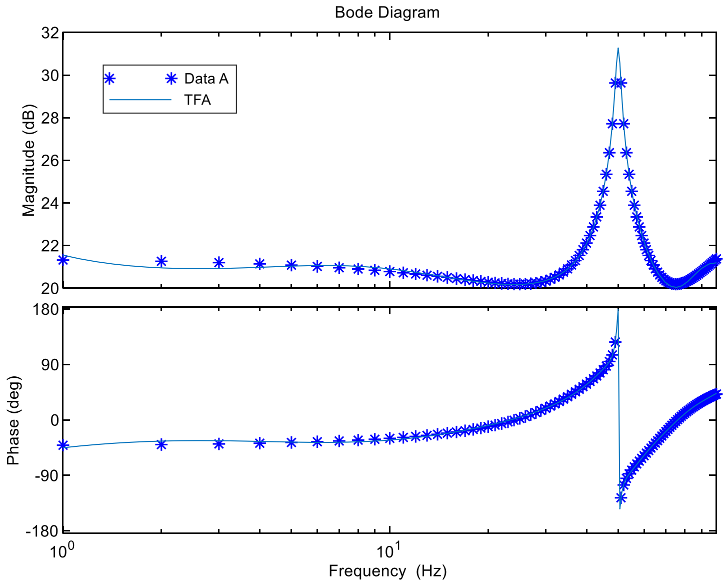
Bode Diagram
Magnitude (dB)
32
30
28
26
24
22
20
Data A
TFA
Phase (deg)
180
90
0
-90
-180
10^0
10^1
Frequency (Hz)

(a)

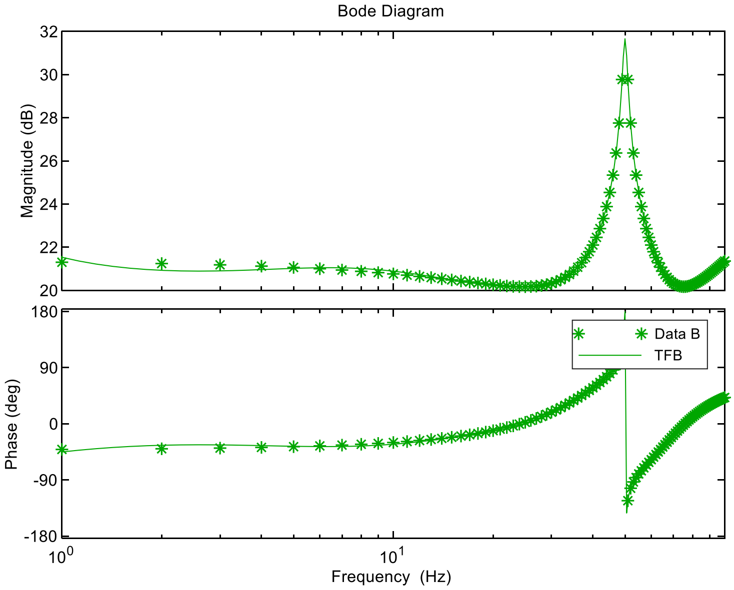
Bode Diagram
Magnitude (dB)
32
30
28
26
24
22
20
Data B
TFB
Phase (deg)
180
90
0
-90
-180
10^0
10^1
Frequency (Hz)

(b)

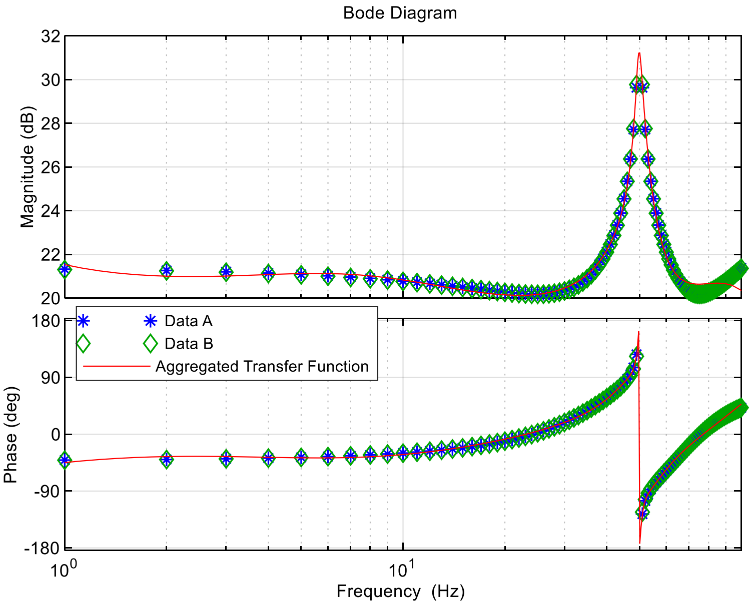

(c)

Figure 6.13 The aggregated transfer function and its original data (a) Operating point A (b)Operating point B (c) Aggregate transfer function using data set A and data set B

Figure 6.13 shows the data from two operating points and the aggregated transfer function. The aggregated transfer function matches the original impedance data.

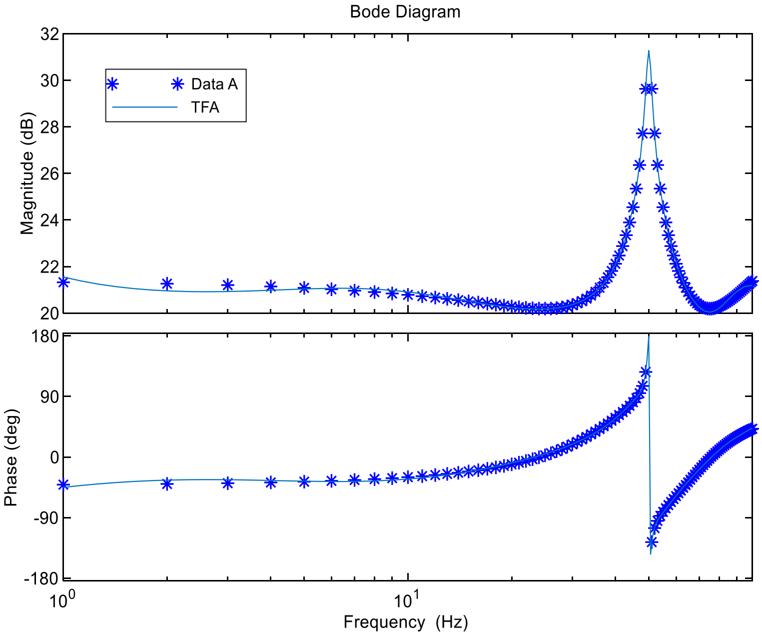

(a)

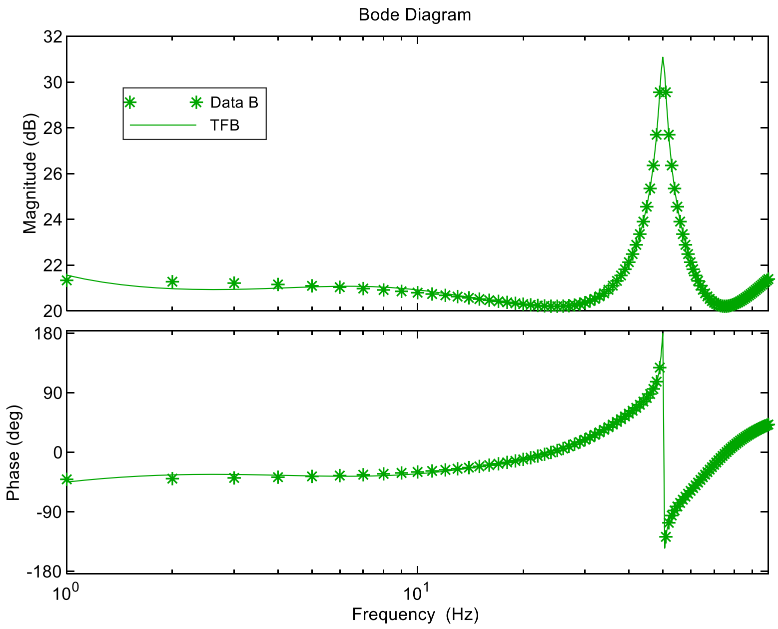

(b)

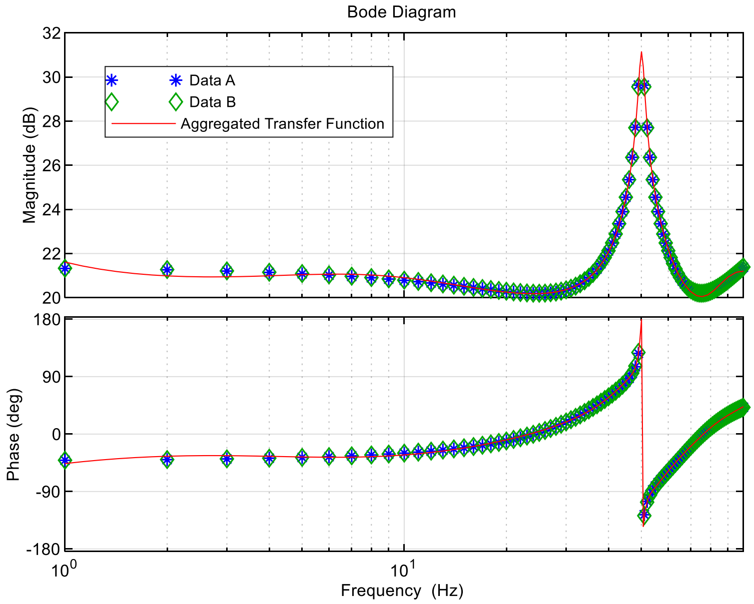

(c)

Figure 6.14 The aggregated transfer function and its original data (a) Operating point A (b) Operating point B (c) Aggregate transfer function using data set A and data set B.

Figure 6.14 shows the aggregated transfer function and the original data sets A and B. The aggregated transfer function has good consistency with the original data. Quantitative analysis data and transfer function similarity results are given in Table 6.4.

Table 6.4 Similarity comparison of aggregation transfer function

	Case 1			Case 2		
	Data A and TFA	Data B and TFB	Data A&B and aggregated TF	Data A and TFA	Data B and TFB	Data A&B and aggregated TF
U_{acref} (p.u.)	1.00	1.00		1.00	0.95	
P_{ref} (p.u.)	1.00	0.90		1.00	1.00	
MSE	0.1040	0.1079		0.1040	0.1022	
AMSE	0.1040	0.1079	0.3679	0.1040	0.1022	0.1313

Table 6.4 provides the similarity between the original data and the aggregated transfer function. This table indicates that the aggregated transfer function has a low AMSE which means it is similar to the original data.

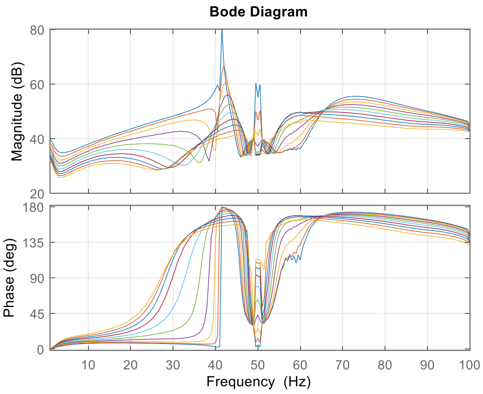

(a)

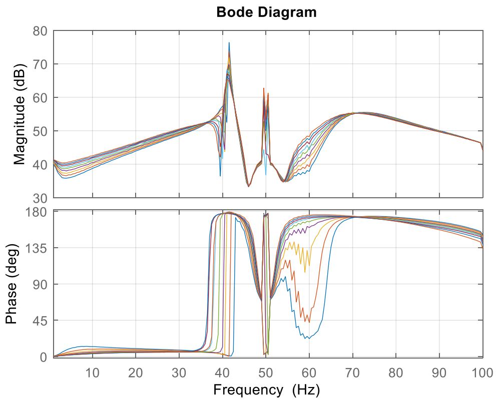

(b)

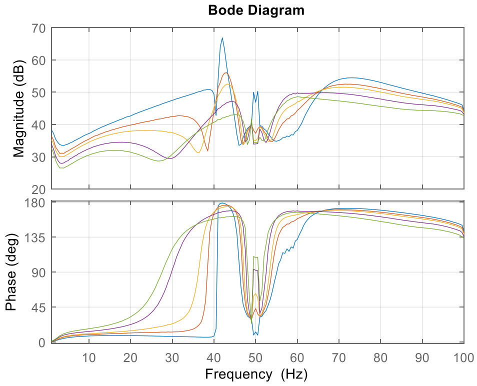

(c)

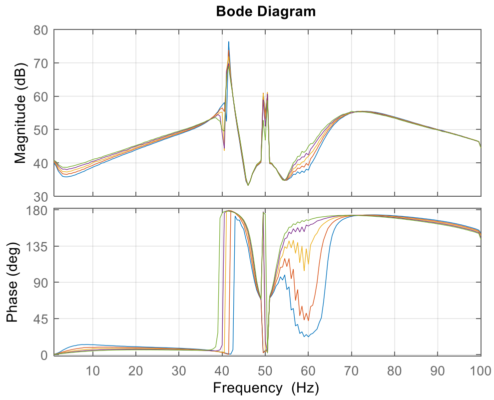

(d)

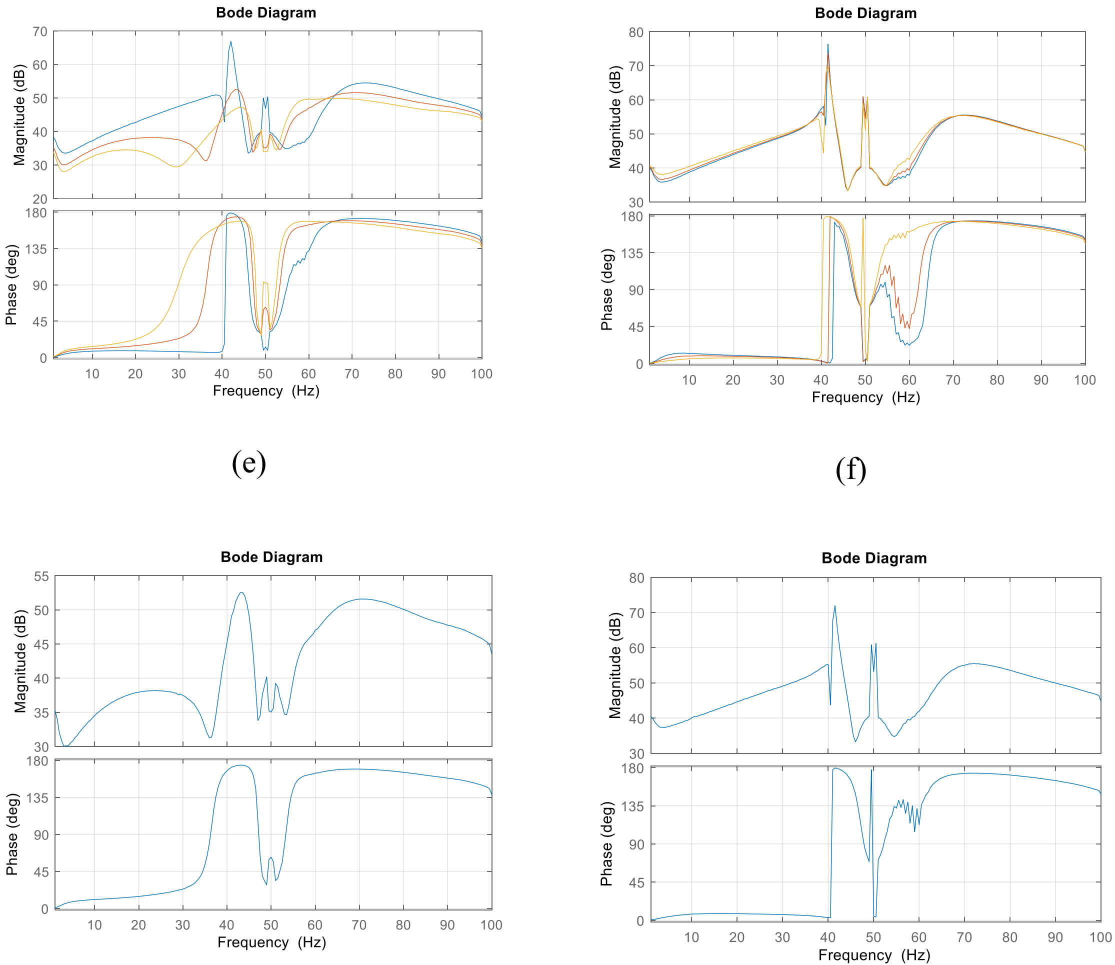

(e)

(f)

(g)

(h)

Figure 6.15 Aggregation results. (a) P cluster=10; (b) U cluster=10; (c) P cluster=5; (d) U cluster=5; (e) P cluster=3; (f) U cluster=3; (g) P cluster=1; (h) U cluster=1.

Figure 6.15 shows the original curves and the aggregated transfer function. When the number of clusters decrease, the error between the aggregated transfer function and the original data will increase. The comparison has been provided in Table 6.5. It shows that with the same cluster number, the DFD is smaller than the MSE which means the MSE is more sensitive to the aggregated data.

Table 6.5 Comparison of aggregation performance on MSE and DFD

Number of aggregated curves	MSE	DFD
10 (original)	<0.001	<0.001

5	<0.01	<0.006
3	<0.1	<0.01
1	<1	<0.04

6. 5 Transfer function network (TFNet): Stability analysis toolbox

6.5.1 Introduction to the toolbox

The developed impedance-based stability analysis toolbox in this work - TFNet is a comprehensive toolbox for impedance analysis in system stability. The versatile toolbox TFNet integrates Python, PSCAD, MATLAB, and Scilab to provide a streamlined and automated solution for impedance-related simulations and data processing. The main function of the software is shown in Figure 6.16.

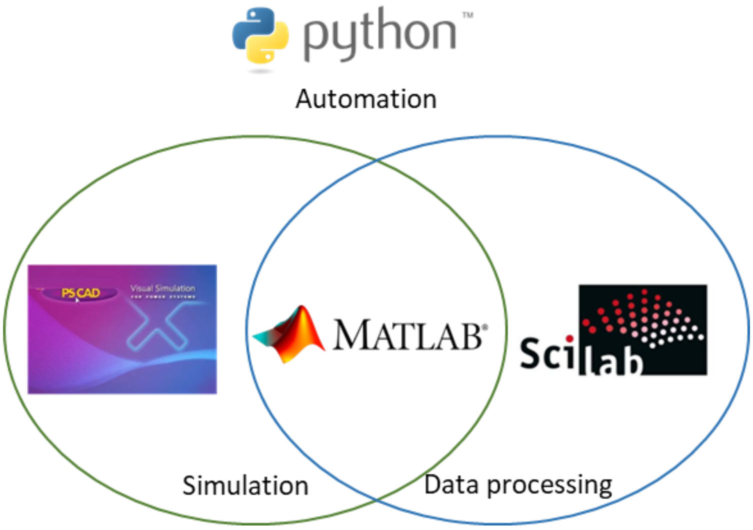

Figure 6.16 The supported software for the developed toolbox

The TFNet is supported by the following software:

(1) Python Automation: The toolbox utilizes Python for its automation capabilities, orchestrating the entire analysis process efficiently.

(2) PSCAD for Simulation: PSCAD is employed for detailed impedance simulations, enabling accurate modelling and analysis of electrical systems.

(3) MATLAB for Simulation and Data Processing: MATLAB plays a dual role in the toolbox, contributing to simulation tasks and handling data processing operations. This integration enhances the overall functionality of the toolbox.

(4) Scilab for Data Processing: Scilab is seamlessly integrated into the toolbox, providing additional capabilities for data processing tasks. This integration allows users to leverage the strengths of both MATLAB and Scilab based on their specific requirements.

The toolbox TFNet offers an automated workflow that simplifies the impedance analysis process: Python coordinates the entire workflow, ensuring a smooth interaction between PSCAD, MATLAB, and Scilab. PSCAD performs detailed simulations, capturing essential impedance characteristics of electrical systems. MATLAB handles both simulation tasks and subsequent data processing, offering a comprehensive solution for impedance analysis. Scilab contributes to advanced data processing, enhancing the toolbox's capabilities for in-depth analysis.

The main advantages of TFNet include:

(1) Efficiency: The automated workflow minimizes manual intervention, improving overall efficiency in impedance analysis.

(2) Versatility: Integration with multiple tools ensures versatility, allowing users to choose the right tool for specific tasks within the impedance analysis workflow.

(3) Comprehensive Analysis: The toolbox enables comprehensive impedance analysis, combining the strengths of PSCAD, MATLAB, and Scilab for accurate results.

In conclusion, the impedance analysis toolbox is a powerful and flexible solution, offering an automated and integrated approach to impedance analysis using Python, PSCAD, MATLAB, and Scilab. Whether you are focused on simulation tasks or data processing, this toolbox provides a seamless and efficient workflow for impedance analysis in electrical systems.

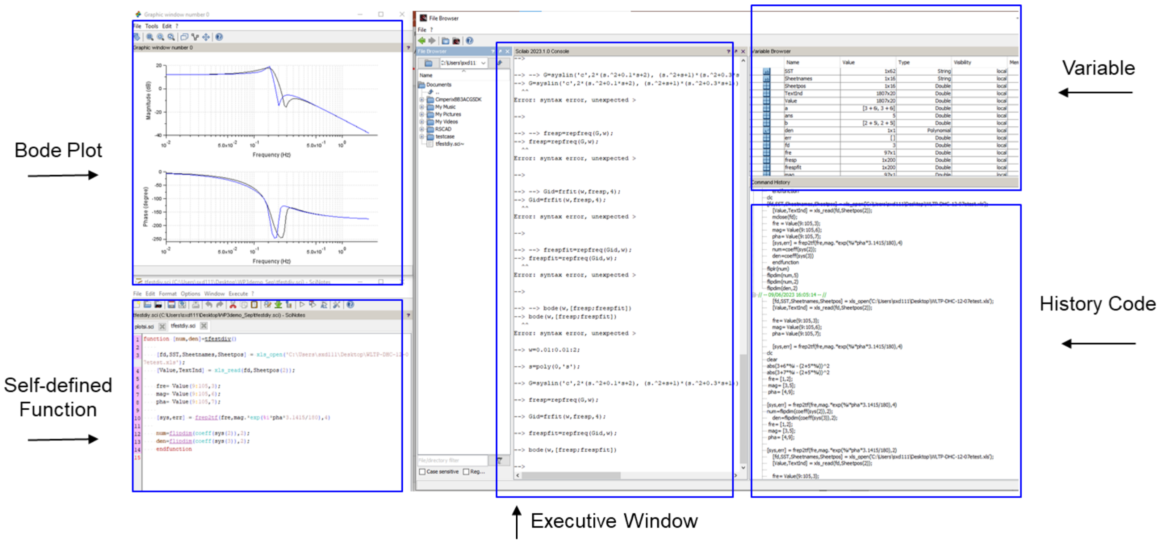

```
function [num,den]=tfestdiy()

    [fd,SST,Sheetnames,Sheetpos] = xls_open('C:\Users\sxd111\Desktop\WLTP-DHC-12-0
7etest.xls');
    [Value,TextInd] = xls_read(fd,Sheetpos(2));

    fre= Value(9:105,3);
    mag= Value(9:105,6);
    pha= Value(9:105,7);

    [sys,err] = frep2tf(fre,mag.*exp(%i*pha*3.1415/180),4)

    num=flipdim(coeff(sys(2)),2);
    den=flipdim(coeff(sys(3)),2);
    endfunction
```

```
-->

--> --> G=syslin('c',2*(s.^2+0.1*s+2), (s.^2+s+1)*(s.^2+0.3*s
--> G=syslin('c',2*(s.^2+0.1*s+2), (s.^2+s+1)*(s.^2+0.3*s+1))
  ^^
Error: syntax error, unexpected >

-->

--> --> fresp=repfreq(G,w);
--> fresp=repfreq(G,w);
  ^^
Error: syntax error, unexpected >

-->

--> --> Gid=frfit(w,fresp,4);
--> Gid=frfit(w,fresp,4);
  ^^
Error: syntax error, unexpected >

-->

--> --> frespfit=repfreq(Gid,w);
--> frespfit=repfreq(Gid,w);
  ^^
Error: syntax error, unexpected >

-->

--> --> bode(w,[fresp;frespfit])
--> bode(w,[fresp;frespfit])
  ^^
Error: syntax error, unexpected >

--> w=0.01:0.01:2;

--> s=poly(0,'s');

--> G=syslin('c',2*(s.^2+0.1*s+2), (s.^2+s+1)*(s.^2+0.3*s+1))

--> fresp=repfreq(G,w);

--> Gid=frfit(w,fresp,4);

--> frespfit=repfreq(Gid,w);

--> bode(w,[fresp;frespfit])

-->
```

Name	Value	Type	Visibility
SST	1x62	String	local
Sheetnames	1x16	String	local
Sheetpos	1x16	Double	local
TextInd	1807x20	Double	local
Value	1807x20	Double	local
a	[3 + 6i, 3 + 6i]	Double	local
ans	5	Double	local
b	[2 + 5i, 2 + 5i]	Double	local
den	1x1	Polynomial	local
err	[ ]	Double	local
fd	3	Double	local
fre	97x1	Double	local
fresp	1x200	Double	local
frespfit	1x200	Double	local
mag	97x1	Double	local

```
    endfunction
  clc
  [fd,SST,Sheetnames,Sheetpos] = xls_open('C:\Users\sxd111\Desktop\WLTP-DHC-12-07etest.xls');
    [Value,TextInd] = xls_read(fd,Sheetpos(2));
    mclose(fd);
    fre = Value(9:105,3);
    mag= Value(9:105,6);
    pha= Value(9:105,7);
    [sys,err] = frep2tf(fre,mag.*exp(%i*pha*3.1415/180),4)
    num=coeff(sys(2));
    den=coeff(sys(3))
    endfunction
  fliplr(num)
  flipdim(num,5)
  flipdim(num,2)
  flipdim(den,2)
// -- 09/06/2023 16:05:14 -- //
    [fd,SST,Sheetnames,Sheetpos] = xls_open('C:\Users\sxd111\Desktop\WLTP-DHC-12-07etest.xls');
    [Value,TextInd] = xls_read(fd,Sheetpos(2));

    fre= Value(9:105,3);
    mag= Value(9:105,6);
    pha= Value(9:105,7);

    [sys,err] = frep2tf(fre,mag.*exp(%i*pha*3.1415/180),4)
  clc
  clear
  abs(3+6*%i - (2+5*%i))^2
  abs(3+7*%i - (2+5*%i))^2
  fre= [1,2];
  mag= [3,5];
  pha= [4,9];

  [sys,err] = frep2tf(fre,mag.*exp(%i*pha*3.1415/180),4)
  num=flipdim(coeff(sys(2)),2);
    den=flipdim(coeff(sys(3)),2);
  fre= [1,2];
  mag= [3,5];
  pha= [4,9];

  [sys,err] = frep2tf(fre,mag.*exp(%i*pha*3.1415/180),2)
    [fd,SST,Sheetnames,Sheetpos] = xls_open('C:\Users\sxd111\Desktop\WLTP-DHC-12-07etest.xls');
    [Value,TextInd] = xls_read(fd,Sheetpos(2));

    fre= Value(9:105,3);
```

Figure 6.17 The interface of Scilab

Figure 6.17 shows the user-friendly interface of Scilab. It includes the plot window, the program, and the history code. The software is free and open source, so users can optimize the interface and code according to their needs.

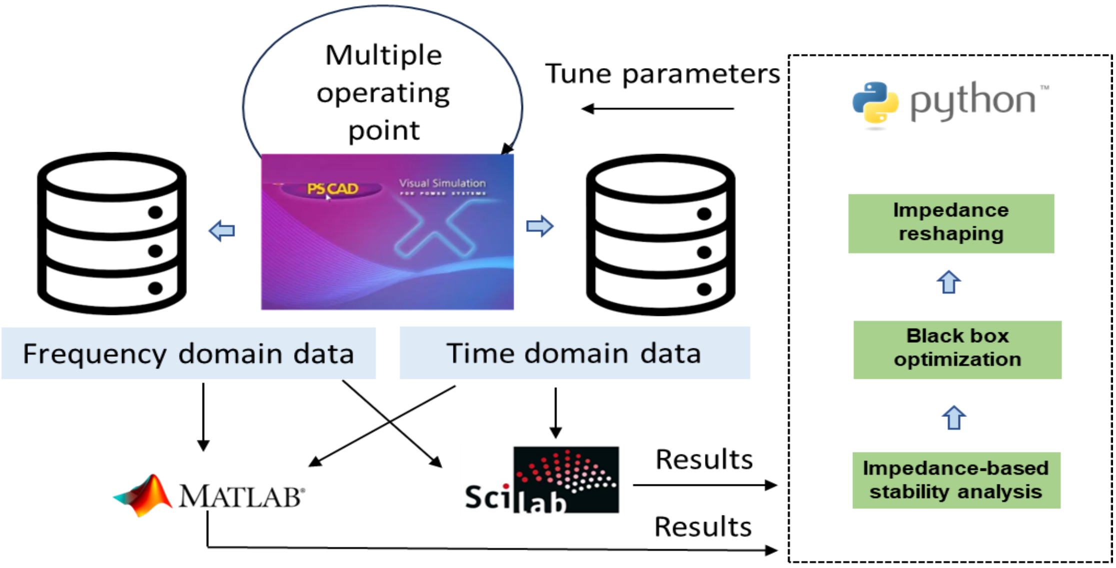

Figure 6.18 The framework of the developed data-driven tool - TFNet

Figure 6.18 shows the main flowchart of this toolbox. PSCAD run the simulation and outputs the time domain or frequency domain data for analysis. Matlab and Scilab load the data file and then calculate the transfer function and eigenvalues. Then the updated parameters are recommended, and Python enables the automation of the whole work.

6.5.2 Functionality

A software interface is developed to help the engineer to input data easily. Some key features are presented in Table 6.7.

Table 6.7 The key features of toolbox TFNet

No.	**Functionality**	**Description**
1	Multiple run	Simulation with variable during each run
2	Parallel run	Run a set of cases on different CPU cores
3	Snapshot	A Snapshot File helps the user start a simulation from a previous saved stable condition to reduce simulation time.
4	Harmonic injection	Three-phase voltage injection at PCC
5	Harmonic measurements	Measurement of voltage and current
6	Multiple operating points	Python script enables automatic change of operating point.
7	FFT analysis	Converter data from the time domain to frequency domain
8	Bode plot	Visualizing frequency domain impedance data
9	Transfer function estimation	Estimation of frequency domain impedance data
10	Eigenvalue calculation	Eigenvalue is obtained from the estimated transfer function.
11	Recommendation	Experience and theory provide advice on tuning parameters.
12	Automatic impedance reshaping	Update the control parameters from the recommendation

6.5.3 Demonstrations of TFNet: Stability analysis toolbox

A simple demonstration of the developed toolbox is given in this section. All modules are assembled and packaged for industrial practice. For new starters and people unfamiliar with Python, this tool also provides a user-friendly interface window, as shown in Figure 6.16. The engineer can set up specific frequencies according to their requirements.

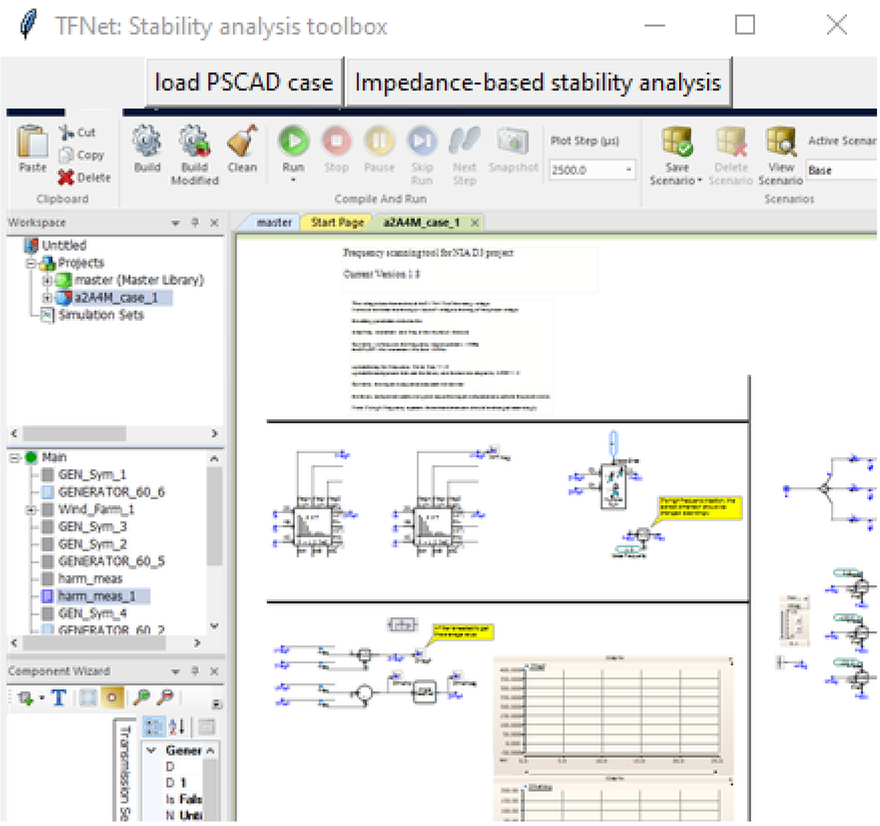

Figure 6.19 The interface window of the toolbox

For senior exports, the freedom to reprogram it or make further development on the codes is offered to enhance their ability.

6.6 Summary

In this Chapter, a data-driven automation method for clustering and aggregation of multiple operating point impedance models has been proposed. The detailed conclusions are summarized as follows:

(1) Automation scanning: The robust model is based on a data set from multiple operating points. This automation scanning is implemented with a Python script which avoids manually setting a large number of simulation scenarios and improves operating efficiency.

(2) Clustering method: a novel clustering method has been proposed based on DFD. Compared to the conventional threshold like MSE, this novel method handles well with the impedance data under different conditions.

(3) Aggregation method: a data shift method has been proposed to aggregate the original data sets without losing the characteristic of the raw impedance data.

(4) The data-driven toolbox has been developed to save time and effort from setting a large number of operating points.

7. Data-driven automation method: Bayesian optimisation to determine stability boundary

7.1 Introduction

Another challenge for impedance modelling under multiple operating points is the time required for simulation especially when the system is large. Fast determining the stable boundary of system operation is of great help to the industry.

Chapter 6 is focused on data clustering and aggregation under multiple operating points. Different to Chapter 6, the objective of this Chapter is to quickly determine the stability boundary of the interconnected network using limited information. Similar to that in Chapter 6, the known information may include the *P*, *Q* and *U* at the PCC. The operation conditions can be regarded as the inputs and the eigenvalues are the outputs, which form a black box model.

Typically, a black-box function can be thought of as a mapping from R^N to R. However, the analytic expression of the mapping relation and the way it works are unknown, so we can only guess the structure of the black-box function by continuously inputting information into the black-box and then using the output to get the relationship. The following Figure 7.1 shows the mapping relation for a generic black-box problem.

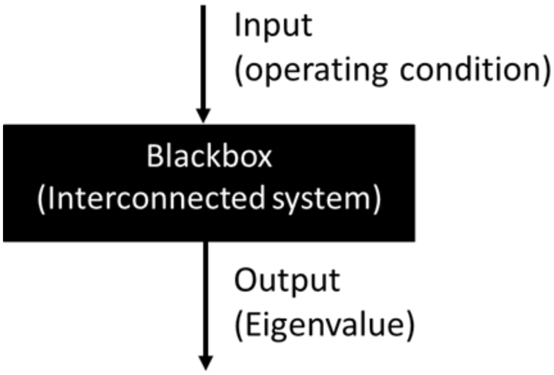

Figure 7.1 Principle of Black box model

In response to the problem of time-consuming traversal of the operating points to find a stable operating range, three optimization methods are compared in Section 7.2. A toolbox based on a Bayesian optimization algorithm based on a black-box model is proposed in Section 7.3. Then, the case studies are implemented to validate the proposed method in Section 7.4. Finally, the summary is presented in Section 7.5.

7.2 Comparison of the methods

7.2.1 Grid search

Grid search is fundamental black-box optimization. The user performs a set of values for individual parameters to be optimized and then evaluates the performance on a grid consisting of the Cartesian product of these parameters. Since the number of evaluations required grows exponentially with the parameters, it is challenging to use for large black-box optimization with many parameters. In addition, if we make the mesh very dense (the base of the set of values corresponding to each parameter is too large), it is computationally expensive even when the number of parameters is small. Assuming that a goal exists in three dimensions with x, y, and z values, the grid search process will perform x*y*z computations to obtain the global optimum.

7.2.2 Random search method

Random search randomly selects possible values of parameters for performance evaluation until the given computing resources are exhausted. When the parameters are much more important, the random search algorithm is often more effective than the grid search method. Generally speaking, when we evaluate the performance of a parameter in total, the grid search can only evaluate each parameter at a position, while the random search can determine the performance of taking different values for each point.

Because the random search algorithm makes no assumptions about the machine learning algorithm and can approximate the optimal solution of the model given sufficient computing resources, it is a useful baseline for evaluating a black-box optimization algorithm. Random search is often combined with more complex optimization algorithms to improve the algorithm's convergence rate and increase the model's exploitability. Because the stochastic optimization algorithm can search the entire parameter space, it is often used to initialize some more complex algorithms. Figure 7.2 shows the grid and random search of nine trials for optimizing.

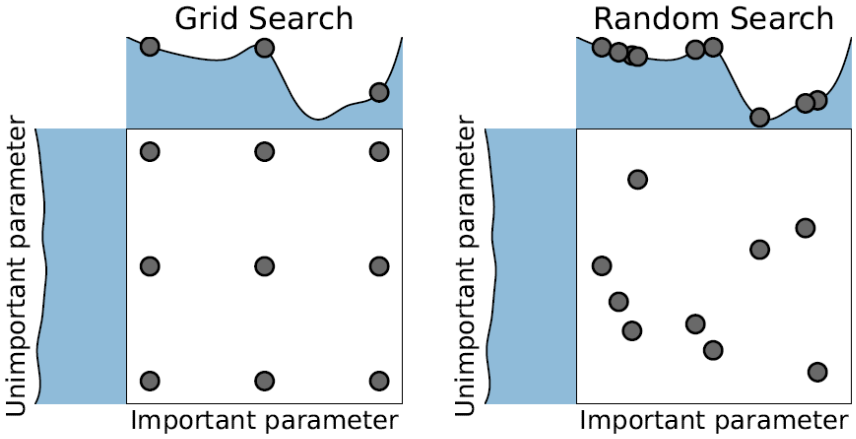

Figure 7.2 Schematic diagram for grid search and random search [112]

7.2.3 Bayesian optimization

Bayesian optimization is a black-box algorithm considering previous experience. The Bayesian theorem describes the posterior distribution of the objective function by constructing a probabilistic model, which is used to select the next sampling point to maximize the sampling value.

The core idea is to model the distribution of the objective function using Gaussian Process Regression (GPR). GPR considers the objective function as a stochastic process consisting of a series of training data points (inputs and outputs) and describes the probability distribution of this stochastic process through a Gaussian probability model. Bayesian optimization satisfies the objective quickly by updating the data in the sample.

This method has two core processes prior function (PF) and acquisition function (AC). PF mainly uses GPR to model the prior distribution of the objective function. AC mainly includes Expected Improvement (EI), which is used to measure the contribution of each point to the optimization of the objective function and select the next sampling point.

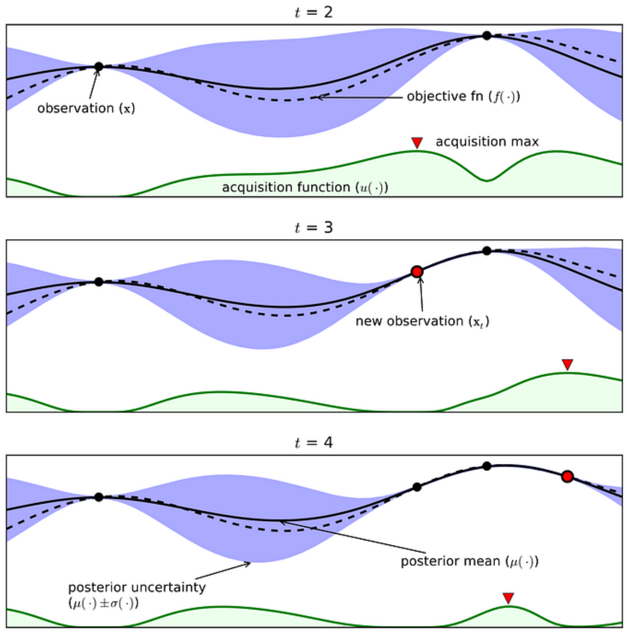

Figure 7.3 Bayesian optimization process flow [113]

Bayesian optimization is used in machine learning kind in AutoML algorithms to determine the hyperparameters of ML automatically. It is also a global extremum search method suitable for high-dimensional nonlinear nonconvex functions with better results and efficiency.

Bayesian optimization considers a function as a stochastic process that satisfies a specific distribution. It improves the accuracy of estimating the function and its extremes by finding the function values in the definition domain, updating the distribution estimate using Bayesian formulas, and then finding the most probable location of the extreme points based on the new distribution.

Table 7.1 The comparisons of the dominant methods

	Grid search	Random search method [112]	Bayesian optimization [113]

Definition	Exhaustively tries every combination of hyperparameters	Randomly tries a pre-defined number of combinations of hyperparameters	Use Bayesian theory to try a pre-defined number of combinations of hyperparameters
Advantage	Easy to understand and implement; easy to parallelize; works well for discrete and continuous spaces.	Relatively efficient	Learn from previous attempts; Significant efficient
Disadvantage	Computationally expensive in large search spaces; Memoryless (does not learn from previous attempts)	May miss important hyperparameters	Difficult to parallelize; Computationally behaviour than grid search and random search; sensitive to the choice of assumption

7.3 Application of Bayesian optimization

The stability analysis aims to understand the cause of the oscillation and find solutions to enhance the stability of the interconnected system. Hence, the practical issue can be reformed to look for the specific operating points in which the dominant eigenvalue is far away from the zero axis.

The index for operating points can be regarded as a function's input, and the function's output is the real part of the dominant eigenvalue from the impedance model. Then the target is to find the possible stable boundary.

$$f^* = f(x^*) = \min_{x \in D} f(x), D \subset \mathbb{R}^N \tag{7.1}$$

where D is a bounded N-dimensional region defined as

$$D = \{x \in \Omega: g_j(x) \leq 0, 1 \leq j \leq p\} \tag{7.2}$$

$$\Omega = [a, b] = \{x \in \mathbb{R}^N: a_i \leq x_i \leq b_i, 1 \leq i \leq N\} \tag{7.3}$$

with a, $b \in \mathbb{R}^N$. The objective function $f(x)$ from (7.1) and constraints $g_j(x) \leq 0$, $1 \leq j \leq p$, from (7.2) is continuous, nonlinear, and can be multiextremal.

Since Gaussian process regression assumes that f(x) follows a normal distribution, an analytical expression for the mathematical expectation can be obtained. Assuming that the mean value at point x is μ=μ(x), the variance is $\sigma^2 = \sigma^2(x)$. Let z=f(x), according to the definition of mathematical expectation EI could be calculated.

$$\begin{aligned} EI_n(x) &= \int_{-\infty}^{+\infty} (z - f_n^*)^+ \frac{1}{\sqrt{2\pi}\sigma} exp\left[-\frac{(z-\mu)^2}{2\sigma^2}\right] dz \\ &= \int_{f_n^*}^{\infty} (z - f_n^*) \frac{1}{\sqrt{2\pi}\sigma} exp\left[-\frac{(z-\mu)^2}{2\sigma^2}\right] dz \\ &= (\mu(x) - f(x^+))\Phi(Z) + \sigma(x)\phi(Z) \end{aligned} \tag{7.4}$$

where x+ is the current optimal solution, Φ and ϕ are the cumulative distribution function and the probability density function of the standard normal distribution, respectively, and z is the standardized improvement, calculated as follows:

$$Z = \frac{\mu(x) - f(x^+)}{\sigma(x)} \tag{7.5}$$

Expected improvement is one of the widely used acquisition functions. The expected improvement represents the gain at each point as a function of that point.

$$x_{n+1} = argmaxEI_n(x) \tag{7.6}$$

Impedance measurements need to be performed on the new operating point after obtaining the operating state of the new sampling point. To perhaps stabilize the range of operation, it is necessary to judge the new operating point, and if the real part of the eigenvalue obtained based on the system impedance of the new operating point is already smaller than the threshold value set in advance, it is considered that the system is currently in critical stability. If the real part of the eigenvalues does not satisfy the threshold condition, the parameter information of the next operating point is further obtained according to the above algorithm.

$$f(x_{n+1}) < \varepsilon \tag{7.7}$$

Then, the specific operating point with the maximum EI value is selected and its eigenvalues are observed. This eigenvalue is treated as new observation data to update the Bayesian optimization model. The update method is to calculate the new posterior distribution, the formula is as follows:

$$\mu_{n+1}(x) = k(x, x_{n+1})[K_{n+1} + \sigma_{n+1}^2 I]^{-1} y_{n+1} \sigma_{n+1}^2(x) \tag{7.8}$$

Here, x_{n+1} is the updated input, including the newly scanned port, and yn+1 is the corresponding output, i.e., the eigenvalue from the transfer function.

Algorithm 1 Sequential model-based optimization

```
Input: f, X, S, M
$D \leftarrow InitSamples(f, X)$
For $i \leftarrow |D| to\ T\ do$
    $p(y|x, D) \leftarrow Fitmodel(M, D)$
    $x_i \leftarrow argmax_{x \in X} S(x, p(y|x, D))$
    $y_i \leftarrow f(x_i)$    expensive step
    $D \leftarrow D \cup (x_i, y_i)$
End for
```

Whether the stopping condition is satisfied will be checked first. The condition can be that the preset number of scans is reached or that the EI values of all ports are below a specific threshold. If the stop condition is satisfied, the port scanning ends; otherwise, the program returns to the step of calculating the EI values and continues the following measurements.

The advantage is that the previous information can be used to lead the following scanning process through Bayesian optimization, thus avoiding ineffective scanning and improving scanning efficiency. In addition, this approach explores the complex patterns of port states, thus enhancing the efficiency of impedance measurements.

7.4 Experiments and validation

The preset target could be reached soon with black-box optimization. The Iris dataset is public for the classification performance of the methods. The results show that Bayesian has less time and the same score compared to grid search and random search which are in Table 7.2.

Table 7.2 The comparison of the performance of the method

Method	**Grid search**	**Random search**	**Bayesian**
Elapsed_time:	546.2	154.8	40.8
Best_score	0.9666666666666668	0.9666666666666668	0.9666666666666668

The Best_score attribute in RandomizedSearchCV or GridSearchCV denotes the highest average score achieved by the model on the validation set, using the optimal parameter combination identified during the cross-validation process. The specific score metric, such as accuracy or F1 score, depends on the problem at hand. A higher Best_score value indicates superior model performance on the validation set.

Throughout the cross-validation process, each parameter combination undergoes training and validation, with the corresponding score being computed. The best_score attribute captures the highest score attained among all parameter combinations. Consequently, upon completion of the search process, the best_score attribute provides a measure of the model's optimal performance.

As shown in Table 7.3, the effect of different system parameters such as Pref and Uacref on the characteristic locus of the impedance transfer function is different. When the eigenvalues are not sensitive to a parameter, we can reduce the step size of the change of that parameter, for instance, U_{ac}.

Table 7.3 Eigenvalues under multiple operating points

Uac	P Reference p.u.

	1	0.9	0.8	0.7	0.6	0.5	0.4	0.3	0.2	0.1
1.05	-8.68	-11.15	-13.67	-16.18	-18.71	-20.08	-21.41	-22.11	-23.13	-23.57
1.04	-8.03	-11.01	-13.8	-16.5	-18.48	-19.96	-21.3	-22.16	-22.96	-23.76
1.03	-7.3	-10.74	-13.78	-16.3	-18.32	-20.04	-20.95	-22.05	-22.95	-23.61
1.02	-6.28	-10.22	-13.51	-16.03	-18.08	-19.82	-20.93	-21.8	-23.01	-23.49
1.01	-5.07	-9.6	-13.07	-15.72	-17.81	-19.6	-21.02	-22.13	-23.19	-23.2
1.00	-3.72	-8.93	-12.7	-15.46	-17.67	-19.55	-20.98	-22.06	-22.74	-23.51
0.99	-2.29	-8.24	-12.25	-15.13	-17.45	-19.43	-20.86	-21.72	-23	-23.09
0.98	-1.51	-7.55	-11.82	-14.86	-17.24	-19.24	-20.7	-21.93	-22.79	-23.1
0.97	+	-6.8	-11.36	-14.56	-16.99	-18.96	-20.8	-21.78	-22.73	-23.11
0.96	+	-6.24	-10.86	-14.16	-16.75	-18.8	-20.55	-21.86	-22.77	-23.29
0.95	+	-5.12	-10.6	-13.83	-16.49	-18.63	-20.56	-22	-22.81	-23.14

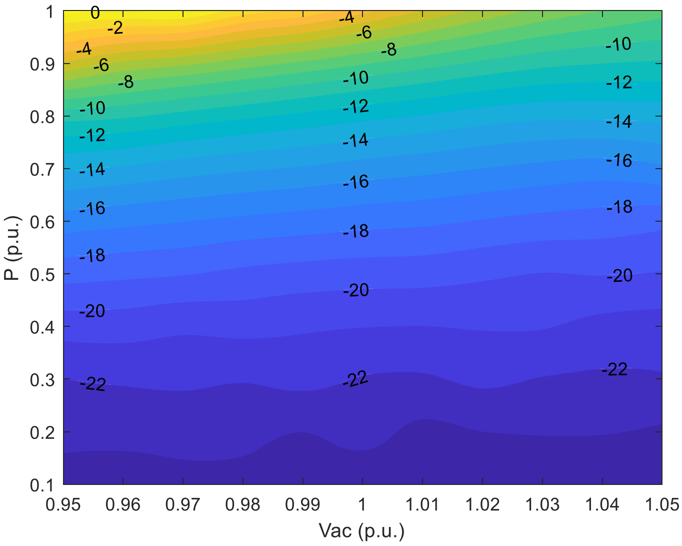

Figure 7.4 The max real part of eigenvalue under multiple operating points in a 2D view

Figure 7.4 describes the real part of the eigenvalues under multiple operating points. In Figure 7.4, under the condition of constant AC voltage, the large colour change indicates that the eigenvalues are more sensitive to the active power reference value. In Figure 7.4, under the condition of constant active power reference value, the small colour change indicates that the eigenvalues are not sensitive to the AC voltage reference value.

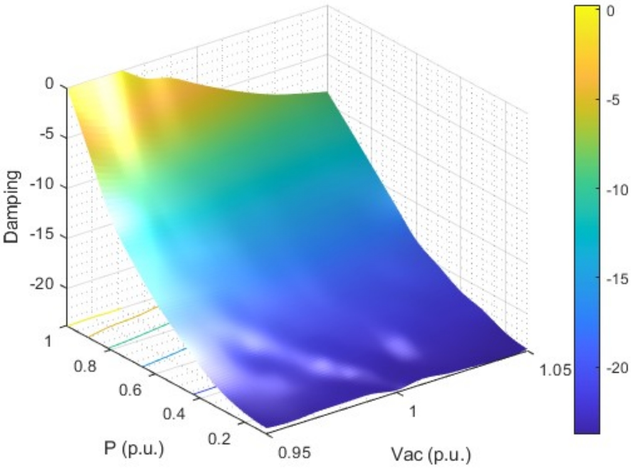

Figure 7.5 The max real part of eigenvalue under multiple operating points in a 3D view

Figure 7.5 describes the trend of eigenvalues under multiple operating points. A larger active output reference value and a smaller AC voltage reference value will weaken system stability.

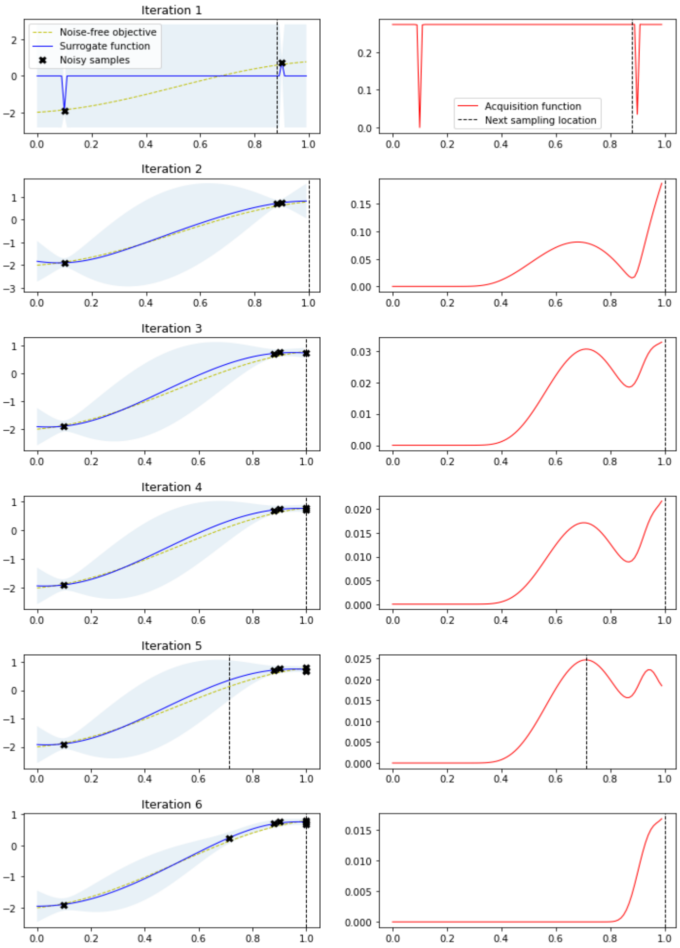

Figure 7.6 The procedure of the Bayesian optimization

Figure 7.6 describes the iterative of the Bayesian optimization. The initial data includes three operating points (U_{acref}=1 pu, P_{ref}=0.1, 0.99 pu) and their max real part of eigenvalues. In this case, the search gain after six iterations is far less than 1, and it can be considered that the worst stable operating point has been found. The comparison between the grid search method and Bayesian methods is given in Table 7.4. Compared with the grid search method, the efficiency of the Bayesian method is increased by 78.61% on a larger scale of operating points (Eg:1100 operating points).

Table 7.4 Comparison between grid search and Bayesian

Operating	Case description			Replication number		Efficiency
points	Range	Increment	Case number	Grid search	Bayesian	improvement
P	0.1-1.0	0.1	10	10	6.85	31.50%
U	0.95-1.05	0.01	11	11	6.29	42.82%
SCR	1.3-4.9	0.4	10	10	5.46	45.40%
Total			1100	1100	235.25	78.61%

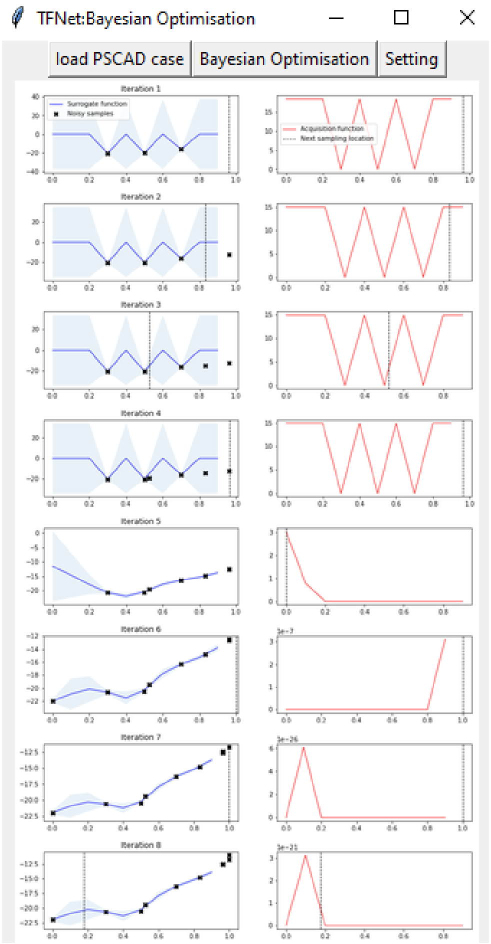

Figure 7.7 The interface of the toolbox

Figure 7.7 shows the front end of the toolbox which is a combination of the graphic design and the user interface. The setting interface allows users to enter the number of iterations and stop conditions according to specific requirements.

7.5 Summary

It is usually time-consuming to traverse all operating points to find the stability boundary of the interactive system. In this Chapter, the aim is to quickly find the boundary of stable operation and reduce the computing time. The two main contributions can be summarized as follows:

(1) A data-driven method using Bayesian optimization has been proposed to determine the stability boundary of the operating point. This method selects the next operating point based on the previous experience which reduces the simulation time compared to the grid search method.

(2) The data-driven method above has been developed into a data-driven toolbox Efficiency improvement, which automatically seeks the stability boundary of the interconnected system is developed. Some features have been pointed out, and further development is accessible to developers.

8. Conclusions and future work

8.1 Conclusions

This thesis focuses on impedance-based stability analysis methods and toolbox. The following key accomplishments were made.

8.1.1 EMT model and impedance implementation

The mathematical impedance model for the inverter is developed and validated with measurement data. The small MSE index is obtained to prove the high similarity between the two methods of modelling. The appropriate guidance is provided on the harmonic magnitude and injection resolution. If the amplitude of a harmonic is too large or too small, it will cause instability in the impedance scan. It is recommended that the amplitude of a single harmonic be about one percent of the fundamental wave. Since the frequency of subsynchronous oscillation is lower than the reference frequency, a resolution of 1 Hz is recommended for impedance scanning. For the specific frequency range and application scenario of interest, both harmonic amplitudes and frequencies should be adapted to obtain accurate impedance data.

8.1.2 Network screening and impedance-based stability

The MIIF is used for screening the network to check the electrical distance between inverters. Then SCR is adopted to identify whether the grid is weak or strong at the connection point. The impedance scan procedures are implemented when IBR is connected to a weak grid. When the impedance of the grid and inverter is captured individually, the close loop transfer function is used to determine whether the interconnected system is stable or not. More specifically, the eigenvalues estimated from the transfer function indicate the oscillation frequency and damping. The real part of the eigenvalue is negative which means the system has positive damping and is stable. The imaginary part of the eigenvalue represents the oscillation frequency.

The measurement impedance data reveals the oscillation characteristics and is applicable to predict potential oscillation phenomena when an inverter is connected to the system.

8.1.3 Impedance reshaping for stability enhancement

A novel control method that adds an auxiliary phase-locked loop to the traditional control method has been proposed to expand the stable operation range of the inverter. The active power reference range for stable operation of the inverter is determined by establishing a state space equation. A simulation model has been established to verify that the proposed auxiliary control method effectively expanded the operating range of the inverter.

8.1.4 Impedance tuning for stability enhancement

Confidentiality and variability of the parameters of power converters motivate applying system identification in power electronic systems. For the black box model where the inverter control parameters cannot be obtained, an automatic optimization control based on the disturbance observation method is designed. The main procedures are to apply a reference voltage disturbance to the operating point and observe the changing trend of the system eigenvalues. If the real part of the characteristic root of the system increases, it means that the disturbance is not conducive to the stability of the system. The range of stable operation of the system can be determined based on the disturbance results, and the system stability can also be enhanced by changing the operating point parameters.

8.1.5 Clustering and aggregation

To assess impedance behaviour across multiple operating points, a clustering method with discrete Frechet distance (DFD) has been proposed to evaluate the similarity between the impedance data and the estimated transfer function. This discrete Frechet distance provides a quantitative measure of system stability, aiding decision-making, and control strategies. An aggregation method based on data shift is proposed to aggregate the multiple event data without losing the original characteristic of the original data. The aggregated transfer function captures the characteristic of the original impedance data and has been used for industry practice.

8.1.6 Data-driven automation method and toolbox TFNet for impedance-based stability analysis

A data-driven method for clustering and aggregation has been proposed with an automation toolbox. This toolbox enables multi-run simulation under multiple operating points, impedance scans and measurements, impedance-based stability analysis and automatic impedance reshaping to enhance system stability.

8.1.7 Data-driven automation toolbox TFNet for black-box optimization

A black-box optimization method based on Bayesian optimization has been proposed to quickly find the stable operation boundary of the system without searching all operating points. The data-driven toolbox has been developed to make the whole progress automatically.

In summary, the research advances the understanding of impedance-related phenomena and equips the industry with practical tools for stability assessment and enhancement.

8.2 Future work

8.2.1 Unbalanced network coupling in DQ and sequence domain

Investigate the impact of unbalanced conditions (such as unbalanced loads, unbalanced generators, or transmission line impedance variations) on the network. The coupling effect between DQ components and sequence components will be explored. The analytical models or simulation tools should be developed to quantify the effects of unbalance on system stability and performance and propose mitigation strategies.

8.2.2 Predicting impedance in unstable operating points

Neural networks will be trained to learn the relationship between system parameters and impedance, which will enable the capture of the impedance curve with predicted data under unstable operating points. The feasibility of using neural networks will be investigated to predict impedance during unstable conditions. The accuracy and robustness of the trained models will be evaluated.

8.2.3 Estimation of the inverter impedance before it is connected to the grid

The harmonic injection module is inserted into the PCC between the inverter and the system which means the inverter has already been connected to the network. Then, if the oscillation mode is detected would be late and cause trouble. Therefore, the developer would like to know the stability of the interconnected system before the inverter is connected. It may be possible to predict the impedance of the inverter after being connected to the wider network.

9. Bibliography

[1] Davis, Steven J., et al. "Net-zero emissions energy systems." Science 360.6396 (2018): eaas9793.

[2] GreenMatch.(15 March 2024). UK's Wind Power: A Gust of Growth in the Renewable Energy Sector [Online]. https://www.greenmatch.co.uk/green-energy/wind

[3] Y. Cheng et al., "Real-world subsynchronous oscillation events in power grids with high penetrations of inverter-based resources," IEEE Transactions on Power Systems, vol. 38, no. 1, pp. 316-330, Jan. 2023, doi: 10.1109/TPWRS.2022.3161418.

[4] Y. Li, L. Fan and Z. Miao, "Replicating real-world wind farm SSR events," IEEE Transactions on Power Delivery, vol. 35, no. 1, pp. 339-348, Feb. 2020, doi: 10.1109/TPWRD.2019.2931838.

[5] IEA (2022), Renewables 2022, IEA, Paris https://www.iea.org/reports/renewables-2022, License: CC BY 4.0

[6] G. Rogers, "The nature of power system oscillations." Power System Oscillations. Boston, MA: Springer US, 2000. 7-30.

[7] "GC0077: Sub-Synchronous Oscillations (SSO)" by SQSS, NETS, and Grid Code GSR018, 2016.

[8] J. Adams, C. Carter and S. -H. Huang, "ERCOT experience with sub-synchronous control interaction and proposed remediation," IEEE PES T&D 2012, Orlando, FL, USA, 2012, pp. 1-5, doi: 10.1109/TDC.2012.6281678.

[9] J. Leslie, G-PST/ESIG Webinar Series: "Managing Grid Stability in a High IBR Network", January 2022. [Online]. Available: https://www.esig.energy/event/webinar-managing-grid-stability-in-a-high-ibr-network/

[10] Sub-synchronous oscillations in GB [Online]. Available: https://www.nationalgrideso.com/document/318951/download

[11] Ren21 Renewables. Global status report collection. Renewables in Energy Supply; 2023.

[12] Y-K Wu, J-H Lin, H-J Lin, "Standards and guidelines for grid-connected photovoltaic generation systems: a review and comparison", IEEE Trans Ind Appl vol. 53, pp:3205–16, 2017. https://doi.org/10.1109/TIA.2017.2680409.

[13] AQ Al-Shetwi, MZ Sujod, "Grid-connected photovoltaic power plants: a review of the recent integration requirements in modern grid codes", Int J Energy Res, vol. 42, pp:1849–65, 2018. https://doi.org/10.1002/er.3983.

[14] Sinha A, Chandra Jana K, Kumar Das M. "An inclusive review on different multilevel inverter topologies, their modulation and control strategies for a grid connected photo-voltaic system," Sol Energy, vol. 170, pp: 633–57, 2018. https://doi.org/10.1016/j.solener.2018.06.001.

[15] H. Bevrani, M. R. Feizi and S. Ataee, "Robust Frequency Control in an Islanded Microgrid: H∞ and μ-Synthesis Approaches," IEEE Transactions on Smart Grid, vol. 7, no. 2, pp. 706-717, March 2016, doi: 10.1109/TSG.2015.2446984.

[16] T. Hornik and Q. -C. Zhong, "A Current-Control Strategy for Voltage-Source Inverters in Microgrids Based on H∞ and Repetitive Control," IEEE Transactions on Power Electronics, vol. 26, no. 3, pp. 943-952, March 2011, doi: 10.1109/TPEL.2010.2089471.

[17] Yang S, Lei Q, Peng FZ, Qian Z. A robust control scheme for grid-connected voltage-source inverters. IEEE Trans Ind Electron 2011;58:202–12. https://doi.org/10.1109/TIE.2010.2045998.

[18] L. Zheng, F. Jiang, J. Song, Y. Gao and M. Tian, "A Discrete-Time Repetitive Sliding Mode Control for Voltage Source Inverters," in IEEE Journal of Emerging and Selected Topics in Power Electronics, vol. 6, no. 3, pp. 1553-1566, Sept. 2018, doi: 10.1109/JESTPE.2017.2781701

[19] B. Guo et al., "A Robust Second-Order Sliding Mode Control for Single-Phase Photovoltaic Grid-Connected Voltage Source Inverter," IEEE Access, vol. 7, pp. 53202-53212, 2019, doi: 10.1109/ACCESS.2019.2912033.

[20] N. Kumar, T. K. Saha and J. Dey, "Sliding-Mode Control of PWM Dual Inverter-Based Grid-Connected PV System: Modeling and Performance Analysis," IEEE Journal of Emerging and Selected Topics in Power Electronics, vol. 4, no. 2, pp. 435-444, June 2016, doi: 10.1109/JESTPE.2015.2497900.

[21] J. Fei and Y. Zhu, "Adaptive fuzzy sliding control of single-phase PV grid-connected inverter," 2017 IEEE International Conference on Mechatronics and Automation (ICMA), Takamatsu, Japan, 2017, pp. 1233-1238, doi: 10.1109/ICMA.2017.8015993.

[22] Y. Zhu and J. Fei, "Adaptive Global Fast Terminal Sliding Mode Control of Grid-connected Photovoltaic System Using Fuzzy Neural Network Approach," IEEE Access, vol. 5, pp. 9476-9484, 2017, doi: 10.1109/ACCESS.2017.2707668.

[23] L. Callegaro, C. A. Rojas, M. Ciobotaru and J. E. Fletcher, "A Controller Improving Photovoltaic Voltage Regulation in the Single-Stage Single-Phase Inverter," IEEE Transactions on Power Electronics, vol. 37, no. 1, pp. 354-363, Jan. 2022, doi: 10.1109/TPEL.2021.3100530.

[24] R. Davoodnezhad, D. G. Holmes and B. P. McGrath, "A fully digital hysteresis current controller for current regulation of grid connected PV inverters," 2014 IEEE 5th International Symposium on Power Electronics for Distributed Generation Systems (PEDG), Galway, Ireland, 2014, pp. 1-8, doi: 10.1109/PEDG.2014.6878684.

[25] J. Zhang, H. Yang, T. Wang, L. Li , DG. Dorrell, and DD-C. Lu, "Field-oriented control based on hysteresis band current controller for a permanent magnet synchronous motor driven by a direct matrix converter. " IET Power Electron, vol. 11, pp. 1277–85, 2018, https://doi.org/10.1049/iet-pel.2017.0651.

[26] Q. Wu, " Simple unipolar maximum switching frequency limited hysteresis current control for grid-connected inverter, " IET Power Electron, vol. 7(12), pp. 933–45, 2014.

[27] M. A. Khan, A. Haque, V. S. B. Kurukuru and S. Mekhilef, "Advanced Control Strategy With Voltage Sag Classification for Single-Phase Grid-Connected Photovoltaic System," IEEE Journal of Emerging and Selected Topics in Industrial Electronics, vol. 3, no. 2, pp. 258-269, April 2022, doi: 10.1109/JESTIE.2020.3041704.

[28] I. S. Mohamed, S. Rovetta, T. D. Do, T. Dragicević and A. A. Z. Diab, "A Neural-Network-Based Model Predictive Control of Three-Phase Inverter With an Output LC Filter," IEEE Access, vol. 7, pp. 124737-124749, 2019, doi: 10.1109/ACCESS.2019.2938220.

[29] Design model-reference neural controller in simulink, R2023b help center. 2023. https://it.mathworks.com/help/deeplearning/ug/design-model-reference-neural -controller-in-simulink.html.

[30] M. Sarvi, M. Keshmiri, "A fuzzy-PD controller to improve the performance of HVDC system," International Journal of Applied Power Engineering, vol.2 , 2013.

[31] M. A. Hannan, Z. A. Ghani, M. M. Hoque, P. J. Ker, A. Hussain and A. Mohamed, "Fuzzy Logic Inverter Controller in Photovoltaic Applications: Issues and Recommendations," IEEE Access, vol. 7, pp. 24934-24955, 2019, doi: 10.1109/ACCESS.2019.2899610.

[32] MA. Hannan, ZA. Ghani,MM. Hoque, MS. Hossain Lipu. "A fuzzy-rule-based PV inverter controller to enhance the quality of solar power supply: experimental test and validation, " Electronics, vol.8, 2019, https://doi.org/10.3390/electronics8111335.

[33] M. Seyedmahmoudian,B. Horan B,TK. Soon,R. Rahmani, AM. Than Oo , Mekhilef S, Stojcevski A. "State of the art artificial intelligence-based MPPT techniques for mitigating partial shading effects on PV systems – a review. " Renew Sustain Energy Rev, vol. 64, pp. 435–455, 2016. https://doi.org/10.1016/j.rser.2016.06.053.

[34] G. Dileep, SN. Singh. "An improved particle swarm optimization based maximum power point tracking algorithm for PV system operating under partial shading conditions. " Sol Energy, vol. 158,pp.1006–1015, 2017. https://doi.org/10.1016/j. solener.2017.10.027.

[35] L. Song, L. Huang,B. Long, F. Li. "A genetic-algorithm-based DC current minimization scheme for transformless grid-connected photovoltaic inverters. " Energies, vol.13, 2020. https://doi.org/10.3390/en13030746.

[36] F. Kabir,N. Yu,Y. Gao, W. Wang. "Deep reinforcement learning-based two-timescale Volt-VAR control with degradation-aware smart inverters in power distribution systems. " Appl Energy, vol.335, 2023, https://doi.org/10.1016/j.apenergy.2022.120629

[37] Y. Lin et al., "Pathways to the Next-Generation Power System With Inverter-Based Resources: Challenges and recommendations," IEEE Electrification Magazine, vol. 10, no. 1, pp. 10-21, March 2022, doi: 10.1109/MELE.2021.3139132.

[38] L. Harnefors, “Modeling of three-phase dynamic systems using complex transfer functions and transfer matrices,” IEEE Trans. Ind. Electron., vol. 54, no. 4, pp. 2239–2248, Aug. 2007.

[39] C. T. Rim, "Unified General Phasor Transformation for AC Converters," IEEE Trans. Power Electron., vol. 26, no. 9, pp. 2465-2475, Sept. 2011.

[40] A. Rygg, M. Molinas, C. Zhang, and X. Cai, “A modified sequence-domain definition and its equivalence to dq-domain impedance definition for the stability analysis of ac power electronic systems,” IEEE J. of Emerg. Sel. Topics Power Electron., vol. 4, no. 4, pp. 1383–1396, Dec. 2016.

[41] L. Harnefors, X. Wang, S. Chou, M. Bongiorno, M. Hinkkanen and M. Routimo, "Asymmetric Complex-Vector Models With Application to VSC– Grid Interaction," IEEE J. Emerg. Sel. Topics Power Electron., vol. 8, no. 2, pp. 1911-1921, Jun. 2020.

[42] Y. Gu, Y. Li, Y. Zhu and T. C. Green, "Impedance-Based Whole-System Modeling for a Composite Grid via Embedding of Frame Dynamics," IEEE Transactions on Power Systems, vol. 36, no. 1, pp. 336-345, Jan. 2021, doi: 10.1109/TPWRS.2020.3004377.

[43] M. Cespedes and J. Sun, "Impedance Modeling and Analysis of Grid-Connected Voltage-Source Converters," IEEE Transactions on Power Electronics, vol. 29, no. 3, pp. 1254-1261, March 2014, doi: 10.1109/TPEL.2013.2262473.

[44] B. Wen, D. Boroyevich, R. Burgos, P. Mattavelli and Z. Shen, "Analysis of D-Q Small-Signal Impedance of Grid-Tied Inverters," IEEE Transactions on Power Electronics, vol. 31, no. 1, pp. 675-687, Jan. 2016, doi: 10.1109/TPEL.2015.2398192.

[45] M. A. Azzouz and E. F. El-Saadany, "Multivariable Grid Admittance Identification for Impedance Stabilization of Active Distribution Networks," IEEE Transactions on Smart Grid, vol. 8, no. 3, pp. 1116-1128, May 2017, doi: 10.1109/TSG.2015.2476758.

[46] P. Zhong, J. Sun, Z. Tian, M. Huang, P. Yu and X. Zha, "An Improved Impedance Measurement Method for Grid-Connected Inverter Systems Considering the Background Harmonics and Frequency Deviation," IEEE Journal of Emerging and Selected Topics in Power Electronics, vol. 9, no. 4, pp. 4236-4247, Aug. 2021, doi: 10.1109/JESTPE.2020.2989436.

[47] X. Wang, L. Harnefors, and F. Blaabjerg, “Unified impedance model of grid- connected voltage-source converters,” IEEE Trans. Power Electron., vol. 33, no. 2, pp. 1775–1787, Feb. 2018.

[48] J. Sun and H. Liu, “Sequence impedance modeling of modular multilevel converters,” IEEE J. of Emerg. Sel. Topics Power Electron., vol. 5, no. 4, pp. 1427–1443, Dec. 2017.

[49] E. Mollerstedt and B. Bernhardsson, “Out of control because of harmonics – an analysis of the harmonic response of an inverter locomotive,” IEEE Control Syst. Mag., vol. 20, no. 4, pp. 70-81, Aug. 2000.

[50] V. Salis, A. Costabeber, S. M. Cox, F. Tardelli, and P. Zanchetta, “Experimental validation of harmonic impedance measurement and LTP Nyquist criterion for stability analysis in power converter networks,” IEEE Trans. Power Electron., vol. 34, no. 8, pp. 7972-7982, Aug. 2019.

[51] H. Wu and X. Wang, “Dynamic impact of zero-sequence circulating current on modular multilevel converters: complex-valued AC impedance modeling and analysis,” IEEE J. Emerg. Sel. Topics Power Electron., vol. 8, no. 2, pp. 1947- 1963, June 2020.

[52] S. Shah and L. Parsa, "Impedance Modeling of Three-Phase Voltage Source Converters in DQ, Sequence, and Phasor Domains," IEEE Trans. Energy Conv., vol. 32, no. 3, pp. 1139-1150, Sept. 2017.

[53] C. Zhang, M. Molinas, A. Rygg, J. Lyu, and X. Cai, “Harmonic transfer function-based impedance modelling of a three-phase VSC for asymmetric AC grids stability analysis,” IEEE Trans. Power Electron., vol. 34, no. 12, pp. 12552-12566, Dec. 2019.

[54] Y. Gu and T. C. Green, "Power System Stability With a High Penetration of Inverter-Based Resources," Proceedings of the IEEE, vol. 111, no. 7, pp. 832-853, July 2023, doi: 10.1109/JPROC.2022.3179826.

[55] J. Sun, "Impedance-Based Stability Criterion for Grid-Connected Inverters," IEEE Transactions on Power Electronics, vol. 26, no. 11, pp. 3075-3078, Nov. 2011, doi: 10.1109/TPEL.2011.2136439.

[56] W. Dong, H. Xin, D. Wu and L. Huang, "Small Signal Stability Analysis of Multi-Infeed Power Electronic Systems Based on Grid Strength Assessment," IEEE Transactions on Power Systems, vol. 34, no. 2, pp. 1393-1403, March 2019.

[57] L. Xiong, X. Liu, Y. Liu and F. Zhuo, "Modeling and Stability Issues of Voltage-source Converter-dominated Power Systems: A Review," CSEE Journal of Power and Energy Systems, vol. 8, no. 6, pp. 1530-1549, November 2022, doi: 10.17775/CSEEJPES.2020.03590.

[58] B. Wen, D. Boroyevich, R. Burgos, P. Mattavelli, and Z. Shen, “Inverse Nyquist stability criterion for grid-tied inverters,” IEEE Trans. Power Electron., vol. 32, no. 2, pp. 1548–1556, Feb. 2017.

[59] F. Liu, J. Liu, H. Zhang, D. Xue, S. U. Hasan, and L. Zhou, “Stability issues of Z+Z or Y+Y Type Cascade System,” Proc. IEEE Energy Conversion Congress and Exposition (ECCE), 2013, pp. 434-441.

[60] F. Liu, J. Liu, H. Zhang, and D. Xue, “Stability issues of Z + Z type cascade system in hybrid energy storage system (HESS),” IEEE Trans. Power Electron., vol. 29, no. 11, pp. 5846–5859, Nov. 2014.

[61] H. Liu, X. Xie, X. Gao, H. Liu, and Y. Li, “Stability analysis of SSR in multiple wind farms connected to series-compensated systems using impedance network model”, IEEE Trans. Power Syst., vol. 33, no. 3, pp. 3118–3128, May 2018.

[62] L. Harnefors, A. G. Yepes, A. Vidal, and J. Doval-Gandoy, “Passivity-based controller design of grid-connected VSCs for prevention of electrical resonance instability,” IEEE Trans. Ind. Electron., vol. 62, no. 2, pp. 702–710, Feb. 2015.

[63] F. Hans, W. Schumacher, S. Chou, and X. Wang, “Passivation of current- controlled grid-connected VSCs using passivity indices,” IEEE Trans. Ind. Electron., vol. 66, no. 11, pp. 8971–8980, Nov. 2019.

[64] X. Wang, F. Blaabjerg, and P. C. Loh, “Passivity-based stability analysis and damping injection for multiparalleled VSCs with LCL filters,” IEEE Trans. Power Electron., vol. 32, no. 11, pp. 8922–8935, Nov. 2017.

[65] D. Lu, X. Wang, and F. Blaabjerg, “Impedance-based analysis of DC-link voltage dynamics in voltage-source converters,” IEEE Trans. Power Electron., vol. 34, no. 4, pp. 3973–3985, Apr. 2019.

[66] A. J. Agbemuko, J. L. Domínguez-García, O. Gomis-Bellmunt and L. Harnefors, "Passivity-Based Analysis and Performance Enhancement of a Vector Controlled VSC Connected to a Weak AC Grid," in IEEE Transactions on Power Delivery, vol. 36, no. 1, pp. 156-167, Feb. 2021, doi: 10.1109/TPWRD.2020.2982498.

[67] Y. Liao, Z. Liu, H. Zhang and B. Wen, "Low-Frequency Stability Analysis of Single-Phase System With dq-Frame Impedance Approach—Part II: Stability and Frequency Analysis," IEEE Trans. Ind. Appl., vol. 54, no. 5, pp. 5012-5024, Sept.-Oct. 2018.

[68] Y. Hao, J. Liang, K.Wang , G. Wu, T. Joseph, R Sun., "Influence of Active Power Output and Control Parameters of Full-Converter Wind Farms on Sub-Synchronous Oscillation Characteristics in Weak Grids, ". Energies, vol. 13, no.19, pp. 5225, 2020. https://doi.org/10.3390/en13195225

[69] J. Liu et al., "Impact of Power Grid Strength and PLL Parameters on Stability of Grid-Connected DFIG Wind Farm," IEEE Transactions on Sustainable Energy, vol. 11, no. 1, pp. 545-557, Jan. 2020, doi: 10.1109/TSTE.2019.2897596.

[70] Z. Liu and X. Guo, "Control Strategy Optimization of Voltage Source Converter Connected to Various Types of AC Systems," in Journal of Modern Power Systems and Clean Energy, vol. 9, no. 1, pp. 77-84, January 2021, doi: 10.35833/MPCE.2020.000352.

[71] J. Fang, X. Li, H. Li and Y. Tang, "Stability Improvement for Three-Phase Grid-Connected Converters Through Impedance Reshaping in Quadrature-Axis," IEEE Transactions on Power Electronics, vol. 33, no. 10, pp. 8365-8375, Oct. 2018, doi: 10.1109/TPEL.2017.2777972.

[72] L. Zhou et al., "Virtual Positive-Damping Reshaped Impedance Stability Control Method for the Offshore MVDC System," IEEE Transactions on Power Electronics, vol. 34, no. 5, pp. 4951-4966, May 2019, doi: 10.1109/TPEL.2018.2865446.

[73] M. Li et al., "The Control Strategy for the Grid-Connected Inverter Through Impedance Reshaping in q-Axis and its Stability Analysis Under a Weak Grid," IEEE Journal of Emerging and Selected Topics in Power Electronics, vol. 9, no. 3, pp. 3229-3242, June 2021, doi: 10.1109/JESTPE.2020.3024863.

[74] C. Li, S. Wang and J. Liang, "Tuning Method of a Grid-Following Converter for the Extremely-Weak-Grid Connection," IEEE Transactions on Power Systems, vol. 37, no. 4, pp. 3169-3172, July 2022, doi: 10.1109/TPWRS.2022.3167899.

[75] L. Zhang, L. Harnefors, and H. Nee, “Power-synchronization control of grid- connected voltage-source converters,” IEEE Trans. Power Syst., vol. 25, no. 2, pp. 809–820, May 2010.

[76] L. Zhang, L. Harnefors, and H. Nee, “Interconnection of two very weak AC systems by VSC-HVDC links using power-synchronization control,” IEEE Trans. Power Syst., vol. 26, no. 1, pp. 344–355, Feb. 2011.

[77] P. Mitra, L. Zhang, and L. Harnefors, “Offshore wind integration to a weak grid by VSC-HVDC links using power-synchronization control: a case study,” IEEE Trans. Power Del., vol. 29, no. 1, pp. 453–461, Feb. 2014.

[78] J. Khazaei, Z. Miao, and L. Piyasinghe, “Impedance-model-based MIMO analysis of power synchronization control,” Electric Power Systems Research, vol. 154, pp. 341–351, Jan. 2018.

[79] L. Huang, H. Xin, and Z. Wang, “Damping low-frequency oscillations through VSC-HVDC stations operated as virtual synchronous machines,” IEEE Trans. Power Electron., vol. 34, no. 6, pp. 5803–5818, Jun. 2019.

[80] G. Denis, T. Prevost, P. Panciatici, X. Kestelyn, F. Colas, and X. Guillaud, “Improving robustness against grid stiffness, with internal control of an AC voltage-controlled VSC,” Proc. IEEE Power and Energy Society General Meeting (PESGM), Boston, MA, Nov. 2016.

[81] T. Qoria, F. Gruson, F. Colas, X. Kestelyn, X. Guillaud, “Analysis of the coupling between the outer and inner control loops of a Grid-forming Voltage Source Converter,” Proc. Europ. Conf. Power Electron. and Appl. (EPE), Sep. 2020.

[82] S. D’Arco, J. A. Suul, and O. Fosso, “Automatic tuning of cascaded controllers for power converters using eigenvalue parametric sensitivities,” IEEE Trans. Ind. Appl., vol. 51, no. 2, pp. 1743–1753, Mar. – Apr. 2015.

[83] S. Wang, Z. Liu, J. Liu, D. Boroyevich, and R. Burgos, “Small-signal modeling and stability prediction of parallel droop-controlled inverters based on terminal characteristics of individual inverters,” IEEE Trans. Power Electron., vol. 35, no. 1, pp. 1045-1063, Jan. 2020.

[84] W. Cao, Y. Ma, F. Wang, L. M. Tolbert, and Y. Xue, “Low-frequency stability analysis of inverter-based islanded multiple-bus AC microgrids based on terminal characteristics”, IEEE Trans. Smart Grid, vol. 11, no. 5, pp. 3662- 3676, Sept. 2020.

[85] F. Wang, J. L. Duarte, M. A. M. Hendrix and P. F. Ribeiro, "Modeling and Analysis of Grid Harmonic Distortion Impact of Aggregated DG Inverters," IEEE Transactions on Power Electronics, vol. 26, no. 3, pp. 786-797, March 2011, doi: 10.1109/TPEL.2010.2091286.

[86] A. A. A. Radwan and Y. A. -R. I. Mohamed, "Modeling, Analysis, and Stabilization of Converter-Fed AC Microgrids With High Penetration of Converter-Interfaced Loads," IEEE Transactions on Smart Grid, vol. 3, no. 3, pp. 1213-1225, Sept. 2012, doi: 10.1109/TSG.2012.2183683.

[87] D. Yang, X. Ruan and H. Wu, "Impedance Shaping of the Grid-Connected Inverter with LCL Filter to Improve Its Adaptability to the Weak Grid Condition," IEEE Transactions on Power Electronics, vol. 29, no. 11, pp. 5795-5805, Nov. 2014, doi: 10.1109/TPEL.2014.2300235.

[88] H. Nian, J. Yang, B. Hu, Y. Jiao, Y. Xu and M. Li, "Stability Analysis and Impedance Reshaping Method for DC Resonance in VSCs-based Power System," IEEE Transactions on Energy Conversion, vol. 36, no. 4, pp. 3344-3354, Dec. 2021, doi: 10.1109/TEC.2021.3066201.

[89] J. Fang et al., "Stability investigation and improvement for DC cascade systems with simplified impedance-based stability criterion," CSEE Journal of Power and Energy Systems, doi: 10.17775/CSEEJPES.2021.00940.

[90] L. Huang, C. Wu, D. Zhou and F. Blaabjerg, "A Double-PLLs-Based Impedance Reshaping Method for Extending Stability Range of Grid-Following Inverter Under Weak Grid," IEEE Transactions on Power Electronics, vol. 37, no. 4, pp. 4091-4104, April 2022, doi: 10.1109/TPEL.2021.3127644.

[91] Y. Wang, L. Wang and Q. Jiang, "Impact of Synchronous Condenser on Sub/Super-Synchronous Oscillations in Wind Farms," IEEE Transactions on Power Delivery, vol. 36, no. 4, pp. 2075-2084, Aug. 2021, doi: 10.1109/TPWRD.2020.3019481.

[92] S. Alarie, et al. "Two decades of blackbox optimization applications." EURO Journal on Computational Optimization, vol. 9, 2021.

[93] R. G. Regis, "Evolutionary Programming for High-Dimensional Constrained Expensive Black-Box Optimization Using Radial Basis Functions," IEEE Transactions on Evolutionary Computation, vol. 18, no. 3, pp. 326-347, June 2014, doi: 10.1109/TEVC.2013.2262111.

[94] C. Li, M. Molinas, O. B. Fosso, N. Qin and L. Zhu, "A Data-driven Approach to Grid Impedance Identification for Impedance-based Stability Analysis under Different Frequency Ranges," 2019 IEEE Milan PowerTech, Milan, Italy, 2019, pp. 1-6, doi: 10.1109/PTC.2019.8810402.

[95] Alenius, Henrik, and Tomi Roinila. "Impedance-Based Stability Analysis of Paralleled Grid-Connected Rectifiers: Experimental Case Study in a Data Center" Energies, vol.13, no. 8, 2020. https://doi.org/10.3390/en13082109

[96] Hosseinipour and J. Khazaei, "Sparse Identification for Data-Driven Dynamics and Impedance Modeling of Power Converters in DC Microgrids," IEEE Journal of Emerging and Selected Topics in Industrial Electronics, doi: 10.1109/JESTIE.2023.3345804

[97] J. Lyu, Y. Rao, Z. Wang, J. Dai and X. Cai, "Data-Driven Impedance Identification and Stability Online Assessment of Wind Farm Connected With MMC-HVDC," in IEEE Transactions on Industry Applications, vol. 60, no. 2, pp. 2567-2576, March-April 2024, doi: 10.1109/TIA.2023.3333760.

[98] Y. Rao, J. Lyu and X. Cai, "Wideband Impedance Online Identification of Wind Farms Based on Combined Data-Driven and Knowledge-Driven," 2022 IEEE International Power Electronics and Application Conference and Exposition (PEAC), Guangzhou,Guangdong, China, 2022, pp. 533-538, doi: 10.1109/PEAC56338.2022.9959118.

[99] Y. Qi, H. Deng, J. Fang and Y. Tang, "Synchronization Stability Analysis of Grid-Forming Inverter: A Black Box Methodology," IEEE Transactions on Industrial Electronics, vol. 69, no. 12, pp. 13069-13078, Dec. 2022, doi: 10.1109/TIE.2021.3137608.

[100] Yang, Dongsheng, et al. "Automation of impedance measurement for harmonic stability assessment of mmc-hvdc systems." 18th Wind Integration Workshop. 2019.

[101] Y. Liao et al., "Neural Network Design for Impedance Modeling of Power Electronic Systems Based on Latent Features," IEEE Transactions on Neural Networks and Learning Systems, doi: 10.1109/TNNLS.2023.3235806.

[102] Y. Li et al., "Neural Network Models and Transfer Learning for Impedance Modeling of Grid-Tied Inverters," 2022 IEEE 13th International Symposium on Power Electronics for Distributed Generation Systems (PEDG), Kiel, Germany, 2022, pp. 1-6, doi: 10.1109/PEDG54999.2022.9923064.

[103] N. Mohammed, W. Zhou, B. Bahrani and D. J. Hill, "Support Vector Machines for Predicting the Impedance Model of Inverter-Based Resources," in IEEE Transactions on Power Systems, doi: 10.1109/TPWRS.2024.3378200.

[104] P. Händel, "Understanding Normalized Mean Squared Error in Power Amplifier Linearization," IEEE Microwave and Wireless Components Letters, vol. 28, no. 11, pp. 1047-1049, Nov. 2018, doi: 10.1109/LMWC.2018.2869299.

[105] M. Niedźwiecki and M. Ciołek, "Akaike's final prediction error criterion revisited," 2017 40th International Conference on Telecommunications and Signal Processing (TSP), Barcelona, Spain, 2017, pp. 237-242, doi: 10.1109/TSP.2017.8075977.

[106] B. Davies et al., “Systems with multiple dc infeed,” CIGRE, Paris, France, 2008.

[107] H. Xiao and Y. Li, "Multi-Infeed Voltage Interaction Factor: A Unified Measure of Inter-Inverter Interactions in Hybrid Multi-Infeed HVDC Systems," IEEE Transactions on Power Delivery, vol. 35, no. 4, pp. 2040-2048, Aug. 2020, doi: 10.1109/TPWRD.2019.2960393.

[108] Cigre WG 14.07 (1992), ‘Guide for planning DC links terminating at AC system locations having low short- circuit capacities’, Part I: AC/DC interaction phenomena. IEEE Std 1204–1997, pp. 1–216, 1997.

[109] P. Kundur, Power System Stability and Control, New York, NY, USA: McGraw-Hill, 1994.

[110] Introducing AIM - Automated Impedance Measurement software [online] https://www.aistability.dk/

[111] Automated Identification of Sub-Synchronous Osci lations (SSO) Events [online] https://smarter.energynetworks.org/projects/nia2_ngeso018/?alttemplate=peaprojectpdf

[112] J. Bergstra, Y. Bengio, "Random search for hyper-parameter optimization. " Journal of machine learning research, vol. 13, no.2, 2012.

[113] Shallow Understanding on Bayesian Optimization. https://towardsdatascience.com/shallow-understanding-on-bayesian-optimization-324b6c1f7083

Appendix A

Simulation parameters of the modified 4-machine test system in Chapter 3.

A.1. Parameters of 4-machine Test System

Table A.1-1: Generator Parameters

Parameters	Value
Rated RMS Line-to-Neutral Voltage	11.54 kV
Rated RMS Line Current	25.98 kA
Inertia Constant	6.5 s
Armature Resistance	0.0025 pu
Potier Reactance	0.2 pu
Unsaturated Reactance (Xd)	1.8 pu
Unsaturated Transient Reactance (Xd’)	0.3 pu
Unsaturated Transient Time	8 s
Unsaturated Sub-transient Reactance (Xd’’)	0.25 pu
Unsaturated Sub-transient Time	0.03 s
Unsaturated Reactance (Xq)	1.7 pu
Unsaturated Transient Reactance (Xq’)	0.55 pu
Unsaturated Transient Time	0.4 s
Unsaturated Sub-transient Reactance (Xq’’)	0.25 pu
Unsaturated Sub-transient Time	0.05 s
Air Gap Factor	1.0

Table A.1-2: Branch Parameters

From Bus	To Bus	***R*** (pu)	***X*** (pu)	***B*** (pu)	Lengths (km)
5	6	0.0025	0.025	0.04375	25
6	7	0.0010	0.010	0.01750	10
7	8	0.0110	0.110	0.19250	110
7	8	0.0110	0.110	0.19250	110
8	9	0.0110	0.110	0.19250	110
8	9	0.0110	0.110	0.19250	110
9	10	0.0010	0.010	0.01750	10
10	11	0.0025	0.025	0.04375	25

Table A-1-3: Transformer Parameters

From Bus	To Bus	***R*** (pu)	***X*** (pu)
1	5	0	0.15
2	6	0	0.15
3	11	0	0.15
4	10	0	0.15

A.2. Parameters of Wind Turbine

Table A.2: Offshore Wind Farm Parameters

Item Name	Value
Nominal voltage of offshore AC grid	230 kV
Rated power of each type 4 wind turbine generators	2 MW
Number of wind turbine generators	350

A.3. Parameters of VSC HVDC

Table A.3: VSC-HVDC parameters

Item Name	Value
Nominal voltage of AC grid	400 kV
Rated MVA of MMC	1000 MVA
Nominal voltage of DC bus	640 kV
Arm reactor	50 mH
Converter reactor	25 mH
Transformer leakage reactance	0.15 pu
Nominal voltage of offshore AC grid	230 kV

Nominal voltage of AC grid	400 kV

Appendix B

Simulation parameters of the inverter in Chapter 2 and Chapter 4.

B.1. Parameters of the system

Table B.1 Parameters for interconnected system

Symbol	Definition	Value
V_g	Grid phase voltage amplitude	50V
f_g	Grid frequency	50Hz
P_n	Rated active power	800W
S_n	Rated apparent power	800VA
I_{max}	Rated current	10.7A
V_{dc}	DC input voltage	600V
f_{sw}	switching frequency	10kHz
L_f	Filter inductor	5mH
R_f	Filter resistor	16mΩ
C_f	Filter capacitor	10μF
SCR	Short circuit ratio	1
L_g	Grid side inductor	15mH
R_g	Grid side resistance	48mΩ
R_g/X_g	Grid side impedance ratio	0.01

B.2. Control parameters of the inverter

Table B.2 Inverter control loop parameters

Symbol	Definition	Value
V_o^*	Output voltage reference	50V
ω_i	Current loop bandwidth	1000 rad/s
ω_v	Voltage loop bandwidth	50 rad/s
ω_p	Power loop bandwidth	10 rad/s
ω_{LPF}	LPF cutoff frequency	200 rad/s
ζ	PLL damping ratio	1
ω_n	PLL natural frequency	200 rad/s

K_{p_PLL}	PLL scaling parameters	400
K_{i_PLL}	PLL integration parameters	40000
K_{p_P}	Power loop proportional parameters	1/1500
K_{i_P}	Power loop integral parameters	1/7.5
K_{p_V}	Voltage loop proportional parameters	10.7/200
K_{i_V}	Voltage loop integration parameters	10.7
K_{p_I}	Current loop proportional parameters	5
K_{i_I}	Current loop integration parameters	16